

Process Improvement of Thin Film Photovoltaic Devices with Studies on the Effect of Electron Transporting Layer

August 2017

ARIYARIT, Atthaporn

A Thesis for the Degree of Ph.D. in Integrated Design Engineering

Process Improvement of Thin Film Photovoltaic Devices
with Studies on the Effect of Electron Transporting Layer

August 2017

Graduate School of Science and Technology
Keio University

ARIYARIT, Atthaporn

Abstract

Given depleted petroleum reserve levels and increasing global warming, studies of photovoltaic devices have increased in volume. However, the production cost of photovoltaic energy is still higher than other types of energy devices. Therefore, increasing the power efficiency of photovoltaic is one choice to solve this problem. Generally, there are many ways to increase power efficiency such as developing new structures of photovoltaic, designing the photovoltaic module in an improved manner, and developing new material for photovoltaic devices. This study focuses on the development of photovoltaic devices and the effect of titanium dioxide in types of organic thin film solar cells (OSCs) and perovskite solar cells (PVSCs). The purpose of studying OSCs are its characteristics: 1) non-toxic material 2) fabrication with wet process like spin-coating, dipping or screen printing and 3) this type of device can be developed for semi-transparent flexible devices. The purpose of studying PVSCs are as follows: 1) fabrication at low temperature 2) the material for fabricating these devices is cheaper than other type of photovoltaic and 3) these devices have high efficiency. Both of these devices require electron transporting layer. Therefore, this thesis also includes the fabrication, optimized process and characterize of electron transporting layer thin film and studies the effect of electron transporting layer in photovoltaic devices.

Content

Chapter 1: Introduction

1.1 History of Photovoltaic -----	1
1.2 Background-----	3
1.2.1 Organic thin film solar cell-----	3
1.2.2 Perovskite solar cell-----	4
1.3 Objective of study-----	6
Reference-----	14

Chapter 2: Titanium Dioxide Layer in Organic Thin Film Solar Cell

2.1 Introduction-----	29
2.2 Experiment-----	30
3.2.1 TiO ₂ electron transport layer-----	30
3.2.2 Characterization-----	30
2.3 Results and Discussion-----	31
3.3.1 Temperature dependent of TiO ₂ by spray LBL-----	31
3.3.2 Optical properties of TiO ₂ fabricated by spray LBL-----	33
2.4 Conclusions-----	35
References-----	44

Chapter 3: Process Improvement for Organic Thin Film Solar Cell

3.1 Introduction for organic thin film solar cell-----	47
3.1.1 Solar radiation-----	47
3.1.2 Basic parameters of photovoltaic-----	48
3.2 Experiment-----	50
3.2.1 Organic semitransparent solar cell-----	50
3.2.2 Flexible organic thin film solar cell-----	51
3.2.3 Characterization-----	52
3.3 Result and Discussion-----	52

3.3.1 Band diagram-----	52
3.3.2 Effect of annealing temperature of TiO ₂ layer-----	53
3.3.3 Effect of thickness TiO ₂ -----	54
3.3.4 Transparent properties of semi-transparent OSC-----	55
3.3.5 Flexible organic thin film solar cell-----	56
3.3.6 Improved the PCE of solar cell module-----	56
2.5 Conclusion-----	57
Reference-----	68

Chapter 4: Optimization Technique with Low Temperature Process for Perovskite Solar Cell

4.1 Introduction-----	72
4.2 Method-----	74
4.2.1 Kriging model method-----	74
4.2.2 NSGA-II-----	75
4.3 Experiment-----	76
4.3.1 Synthesis of Methyl Ammonium Iodide-----	76
4.3.2 Devices Fabrication-----	76
4.3.3 Characterization-----	77
4.3 Results and Discussion-----	78
4.4.1 Design of experiment-----	78
4.4.2 Control film thickness of perovskite layer-----	78
4.4.3 Photovoltaic characteristics-----	79
4.4.4 Surface morphology and crystalline property-----	80
4.4.5 Predicting the mapping surface via Kriging model-----	81
4.4.6 Validation of the optimization via genetic algorithm-----	82
4.5 Conclusions-----	84
References-----	100

**Chapter 5: Process Improvement for cm² Perovskite Solar Cell with
Studies Effect of TiO₂**

5.1 Introduction----- 104

 5.1.1 Fabrication method for perovskite layer----- 106

 5.1.1.1 One-step method----- 106

 5.1.1.2 Two-step method----- 107

5.2 Experiment----- 108

 5.2.1 Substrate preparation----- 108

 5.2.2 Devices fabrication----- 108

 5.2.3 Characterization----- 109

5.3 Results and Discussion----- 110

 5.3.1 Surface modification by dynamic spin coating----- 110

 5.3.2 Investigated the changing of surface morphology----- 111

 5.3.3 Optimization by design of experiment----- 114

 5.3.4 The selection of parameters range ----- 114

 5.3.5 Predicting the mapping surface via Kriging model----- 116

5.4 Conclusions----- 117

References----- 134

Chapter 6: Conclusion

6.1 General summary----- 139

6.2 Future approach----- 140

Acknowledgement----- 142

List of Figures

Fig.1-1 Summary of type and generation photovoltaic.

Fig.1-2 The highest PCE of each type of solar cell with time published by Progress in Photovoltaics.

Fig.1-3 Schematic diagrams of perovskite solar cells in the (a) n-i-p mesoscopic, (b) n-i-p planar,(c) p-i-n planar, and (d) p-i-n mesoscopic structures.

Fig.1-4 The overview of this thesis.

Fig. 2-1 Mass difference of 20 TALH/PDDA bilayers using quartz crystal microbalance (QCM) measurements.

Fig. 2-2 Mass difference of one TALH/PDDA bilayer using QCM measurements.

Fig. 2-3 XRD results for titanium dioxide layers fabricated using the spray-LBL method after annealing at different temperatures.

Fig. 2-4 The crystalline formation arrangement mechanism of TALH precursor to mix rutile and anatase thin film. Reprinted with permission form [2-16] Copyright 2015, American Chemical Society.

Fig. 2-5 2Theta and FWHM of (a) TiO₂ anatase phase (004) and (b) TiO₂ rutile phase (210) when fabricated with Spray LBL on glass and annealing at difference temperature

Fig. 2-6 XPS spectra of oxygen in a titanium dioxide thin film fabricated by spray-LBL method before (top) and after annealing at 450°C (bottom).

Fig. 2-7 SEM images of TiO₂ layers deposited by spray-LBL on glass before annealing (a) and after annealing at various temperatures: (b) 300°C, (c) 350°C, (d) 400°C, (e) 450°C, and (f) 500°C.

Fig. 2-8 SEM image of TiO₂ layer fabricated by spray-LBL on FTO substrate after annealing at 450°C.

Fig. 2-9 AFM image of (a) FTO layer, Rms of surface=32 nm (b) TiO₂ layer on FTO when fabricated with Spray LBL and annealing at 450 °C, Rms of surface=50 nm

Fig. 2-10 Transmittance of TiO₂ layers fabricated by spray-LBL on glass substrates before and after annealing at various temperatures.

Fig. 3-11 Tauc plot of TiO₂ layers fabricated by spray-LBL method on glass substrates before and after annealing at various temperatures.

Fig. 3-1 The solar radiation spectrum and wavelength with condition AM0 and AM1.5

Fig.3-2 A carrier concentration of p–n junction in thermal equilibrium with zero-bias voltage applied.

Fig.3-3 Current density –Voltage characteristics of solar cell under illumination. Determination of maximum power output is indicated.

Fig. 3-4 Equivalent circuit of one diode model.

Fig. 3-5 Flow chart for fitting parameter: R_s , R_{sh} , n , J_0 and J_{ph} by using one diode model with Trust-region algorithm.

Fig. 3-6 Structure of bulk heterojunction solar cell, and (b) band diagram of bulk heterojunction solar cell in this experiment.

Fig 3-7 Performance of solar cell when fabricated TiO_2 layer with LPD and Spray LBL method

Fig. 3-8 Performance of solar cell when changing the thickness of TiO_2 layer when annealing at $450\text{ }^\circ\text{C}$

Fig. 3-9 Transmittance of the semitransparent solar cells with the electron transport layer fabricated by Spray-LBL after annealing at $450\text{ }^\circ\text{C}$.

Fig. 3-10 Current density-voltage characteristic of semitransparent solar cell with the electron transport layer fabricated by Spray-LBL after annealing at $450\text{ }^\circ\text{C}$

Fig. 3-11 Current density –Voltage characteristic of bulk heterojunction solar cells when fabricate the electron transport layer by spray-LBL without annealing and change the thickness of TiO_2 layer by changing number of bilayers.

Fig. 3-12 Current density–Voltage characteristics of bulk heterojunction solar cells with the electron transport layer fabricated by Spray-LBL after annealing at $450\text{ }^\circ\text{C}$ using silver nano- network and silver thin films on PET substrate.

Fig. 4-1 Flowcharts showing the modelling and optimization process using in this report.

Fig. 4-2 Algorithms of simple GA.

Fig .4-3 Ranking by NSGA-II)Minimization of f_1 and f_2)

Fig. 4-4 a) Energy band diagram and b) Devices structure of our cell.

Fig .4-5 Relation between spin-coating speed and thickness of perovskite layer

Fig .4-6 Relationship between J_{sc} and V_{oc} from the original experimental data.

Fig .4-7 Relationship between experiment parameters and efficiency of devices from original experimental data.

Fig .4-8 SEM images of perovskite layer under conditions in **Table 4-1**.

Fig .4-9 Relationship between input parameters and a) the average grain size, b) standard deviation and c) crystalline conversion ratio into MAPbI₃.

Fig .4-10 Grain size distribution of perovskite thin film surface.

Fig .4-11 The XRD spectra of perovskite layer on FTO/SnO₂ fabricated under conditions in **Table 4-1**.

Fig .4-12 Surface plot of the relationship between experimental parameters (spin speed, time) and outputs a) short circuit current density (J_{sc}), b) open circuit voltage (V_{oc}) and c) power conversion efficiency.

Fig .4-13 Non-dominated solution of output parameters; V_{oc} , J_{sc}

Fig .4-14 Surface plot of the relationship between experimental parameters (spin speed, time) and a) S.D of grain and b) conversion of MAPbI₃.

Fig .4-15 Relationship of efficiency and input parameters (spin speed and dipping time) derived from NSGA-II.

Fig .4-16 Current-voltage characteristics of the highest performance devices fabricated with optimal condition.

Fig. 5-1 Schematic of one step method deposition. Reprint with permission form [5-3] Copyright 2015, The American Association for the Advancement of Science.

Fig. 5-2 (a) Schematic illustration of in situ formation of FAPbI₃ by in situ dipping reaction of PbI₂ and FAI on the TiO₂ surface. Reprinted with permission form [5-26] Copyright 2015, American Chemical Society.

Fig. 5-3 Schematic of fabrication of perovskite solar cell based on the modified two - step spin method.

Fig. 5-4 The image of 1 cm² scale area PVSCs when fabricate with modified two - step method.

Fig. 5-5 Surface morphology analysis of perovskite layer when washing surface with different spin speed.

Fig. 5-6 XRD pattern of perovskite film when washing perovskite with difference spin speed.

Fig. 5-7 The sample picture before and after using dynamic-spin washing method with SEM surface of dry area and wet area.

Fig. 5-8 XRD pattern of perovskite films area with the residual solution and the dry area.

Fig. 5-9 Schematic of explanation of difference surface structure when washing surface of perovskite with difference spin speed.

Fig. 5-10 Cross-section and schematic of remain solution area and dry area of boundary of difference perovskite surface morphology.

Fig. 5-11 Relationship between film thickness of mesoporous-TiO₂ layer and spin-speed to fabricated mesoporous-TiO₂.

Fig. 5-12 Surface plot of the relationship between experimental parameters (spin speed of dense-TiO₂ and mesoporous-TiO₂) and outputs a) short-circuit current density (J_{sc}), b) open circuit voltage (V_{oc}), fill factor (FF) and d) power conversion efficiency (PCE).

Fig. 5-13 Current-voltage characteristics of the highest performance of (a) small area devices and (b) large area devices when fabricated with the optimal condition. 0.09cm² for the small surface area and 1 cm² for large surface area devices.

List of Table

Table 2-1 The crystalline size of anatase (004) and rutile (210) after annealing at different temperatures.

Table 2-2 Haze value and transmittance of FTO, TiO₂/FTO and TiO₂/FTO after annealing at 450 °C

Table 2-3 The refractive index, haze and energy band gap of TiO₂ fabricated by Spray-LBL and annealing with difference temperature .

Table 3-1 The value of LUMO and HOMO level of each layer of organic thin film solar cell.

Table 3-2 Electrical properties of solar cells with the electron transport layer fabricated Spray-LBL method before and after annealing at different temperatures.

Table 3-3 The optical properties of electron transport layers fabricated by Spray-LBL method after annealing at 450°C with changing the thickness of TiO₂ layer

Table 3-4 Electrical properties of solar cells with electron transport layers fabricated by spray-LBL method after annealing at 450°C for various TiO₂ layer thicknesses.

Table 3-5 Haze value and transmittance of FTO, TiO₂/FTO and TiO₂/FTO after annealing at 450 °C

Table 3-6 The properties of solar cell when fabricated the electron transport layer with spray-LBL method without annealing and change the number of bilayer

Table 4-1 Input parameters for fabricating perovskite layer assigned by LHS method.

Table 4-2 Output parameters of perovskite solar cells fabricated by using the conditions in **Table 4-1**.

Table 4-3 The conversion ratio of PbI₂ to MAPbI₃, grain size average and S.D value of perovskite grain when fabricated with difference condition.

Table 4-4 Current density-voltage parameters of perovskite solar cell when fabricated with optimal condition.

Table 5-1 Conversion ratio of PbI₂ to MAPbI₃ when washing them with IPA at difference spin speeds

Table 5-2 The conversion ratio of PbI₂ to MAPbI₃ between dry area and wet area

Table 5-3 Current density-voltage parameters of small area of PVSCs fabricated with difference washing IPA spin speed.

Table 5-4 Current density-voltage parameters of cm^2 area of PVSCs fabricated with difference washing IPA spin speed.

Table 5-5 Current density-voltage parameters of perovskite solar cell (FTO/Dense- TiO_2 /perovskite/Au) when fabricated with changing fabrication spin speed of compact TiO_2 layer.

Table 5-6 Input parameters for fabricating dense- TiO_2 and mesoporous TiO_2 layer assigned by Latin-hyper cube method.

Table 5-7 Current density-voltage parameters of perovskite solar cell (half-cell) when fabricated by using the conditions in **Table 5-6**.

Table 5-8 Current density-voltage parameters of perovskite solar cell(half cell) when fabricated with optimal condition

Table 5-9 Current density-voltage parameters of perovskite solar cell when fabricated with 0.09cm^2 and 1 cm^2 scale area.

Table 5-10 Current density-voltage parameters of perovskite solar cell when fabricated with optimal condition

Chapter 1

Introduction

Solar photovoltaic devices are commonly known for their ability to generate electrical power from light energy. These products are sustainable, can be used in every area around the world and offer cleaner energy. However, the production cost per watts and production power consumption are still high. Therefore, the development of reduced production cost, lower process temperature and less toxic environment for fabricating this product are very interesting to studies, and to future potential use.

1.1 History of photovoltaic

The first photovoltaic was developed by Charles Fritts in 1883 on the substrate selenium wafers. In 1954, the first generation of photovoltaic commenced, with the success of crystalline silicon solar cell [1-2]. The research of first generation photovoltaic focused on theory with homo-junction structure and studied it on crystalline wafer based substrate such as monocrystalline-Silicon solar cell(c-Si) [3-4], polycrystalline-silicon solar cell(poly-Si) [5-6], Gallium-Arsenide [7] and multi-junction solar cell [8-11].

However, the costs of the substrate to fabricate the photovoltaic in the first generation were high. Therefore, the researchers in the second generation of photovoltaic focused on decreasing the cost of fabricated photovoltaic. A key idea from this era was developing the thin film structure for photovoltaic. The examples of the second generation photovoltaic are amorphous silicon solar cell(a-Si) [12-14], tandem solar cell (a-si/ μ -Si Solar cell) [15-19], heterojunction intrinsic thin layer solar cell(HIT) [20,21], CdS/CdTe solar cell [22-24] and Cu(In,Ga)Se solar cell (CIGS) [25-30].

The next generation of photovoltaic, the third generation, also focused on decreasing fabrication cost by material engineering of photovoltaic. The main objective of development in this era was higher power conversion efficiency (PCE) with lower cost and a greener process [31-35]. The main type of solar cell in this era are organic thin film solar cell (OSC) [36-40], Dye-sensitized solar cell (DSSC) [41-43], Cu(Zn,Sn)Se solar cell (CZTS) [44-47] and Perovskite solar cell (PVSC) [48-52].

The summary generation of photovoltaic are shown in Fig. 1-1. Fig. 1-2 shows the development of highest PCE of each type of photovoltaic by time. From this graph, the type of photovoltaic cell which demonstrates the highest efficiency among photovoltaic cells is the multi-junction cell developed by Fraunhofer-Institute for Solar Energy Systems(ISE) [53].

1.2 Background

1.2.1 Organic thin film solar cell

The recent development of photovoltaic field required improvements in material like OSCs and PVSCs. The OSCs were developed based on the conductivity in halogen doped organic compound in 1954, but these compounds were not stable [54]. Over several years, much research has focused on the charge transport properties of small molecules [55].

The first OSCs were based on active layer by single material with different work function material of two-sided electrodes [56]. However, these devices still have low efficiency, with PCE lower than 1%, due to not enough process temperature and the thickness of sample being too high (much higher than exciton diffusion length). After that, the first organic bilayer solar cells were developed by Tang et al. in the late 1970s [57]. This organic bilayer solar cell devices were made of two conjugated small molecules and achieved a PCE of around 1%. The typical type of OSCs is shown in Fig. 2(a). The limiting factor of this concept is the layer thickness of the absorbing material, which is much higher than the diffusion exciton length.

In the early 1990s, this problem was addressed solved by combining donor and acceptor in the same layer, which named as “bulk heterojunction solar cell” [58]. The structure of the bulk heterojunction solar cell is show in Fig 2(b). This structure has the advantage of being able to dissociate excitons very efficiently over the whole extent of the solar cell, and thus generating electron-hole pairs throughout the films. The requirement for efficient bulk heterojunction solar cells is good control of surface morphology. However, this type of OSCs remain in need of improved efficiency and optimization.

After the first devices of bulk heterojunction solar cell, many research groups improved the efficiency of OSCs by making use of new processes: Li et al. developed high-efficiency solution processable polymer photovoltaic cells by self-organization of polymer blends in 2005 [59], Aernouts et al. developed polymer-based organic solar cells using ink-jet printed active layers in 2008 [60], and Srinivasan et al. developed PTB7:PC71BM by using the Spray-Coating Method in 2015[61]. Some research groups developed new material for OSC: Peumans et al. developed small molecular weight organic thin-film photodetectors and solar cells in 2003 [62], Collins et al. developed PTB7: PC71BM solar cells in 2012 [63].

1.2.2 Perovskite Solar Cell

The first perovskite solar cell device was developed by Miyasaka *et al* in 2009 with efficiency of 3.8% [64]. However, the first devices contained a liquid electrolyte and received little attention as they were inefficient and unstable. In 2012, the first solid-state cells were developed with an efficiency around 10%. Since then, the device performance of perovskite solar cell have rapidly progressed and the best PCE record over 22% in mid-2016 [65, 66]. This rapid improvement in performance was because of inexpensive fabrication, easy processing and excellent material properties [67-70]. Moreover, high quality perovskite thin films can be fabricated with solution and vapor based deposition methods. Many of these methods are possible to fabricate with large-scale, flexible and semitransparent, which increased the features of commercialization of perovskite solar cells [71-76]. In addition to the choice of fabrication process, perovskite materials also have outstanding optoelectronics properties that can benefit photovoltaic application [77-80].

The outstanding properties of this material are 1) the band gap of MAPbI₃ is 1.55 eV which is nearly ideal of single-junction solar cells exposed to the solar spectrum, and it can be adjust the band gap from 1.5 to 2.3 eV[81, 82], 2) this material also has a higher absorption coefficient than other photovoltaic material like Si, CdTe/CdS, CIGS and a-Si, so the thickness of this material can decrease to 300 nm[83, 84], 3) high electron and hole mobility of this material are in order of 10 to 60 cm²/Vs and long carrier lifetime (around 100 ns) resulting in long diffusion lengths(around 1 μm) so the charge carriers can easy to transport across the 300 nm thickness of perovskite absorber layer before recombination [85, 86], and 4) Due to electronic defect are shallow and relatively harmless so the non-radiative recombination rates are low, benefitting an increase the open-circuit voltage (Voc) over 1 V [87, 88].

The first PVSCs were used as a direct replacement for dye sensitizer in the DSSCs. The conventional DSSC structure use a thick porous TiO₂ layer that is coated and absorb dye material [89-90]. In these devices, TiO₂ is used to transport the electron and block the hole, while the electrolyte is used as a hole conductor. The original perovskite solar cell was also developed with this structure. After that the mesoporous electron transporting layer (ETLs) were developed and replaced the liquid electrolyte with solid-state hole conductors, which have the advantage of being developed for thin-film structure like OSCs [91-95]. The name of this structure is n-i-p mesoporous perovskite solar cell (Fig. 1-3a). To develop the structure of PVSCs, some research groups succeeded in developing a planar device structure for PVSCs. The planar devices use perovskite material for absorber with sandwiched layer between dense ETLs, without mesoporous layer, and hole transporting layers (HTLs) [96-99]. The planar PVSCs can be classified into two types, based on which layer one first encounters. The two types of perovskite solar cell are n-i-

p (Fig. 1-3c) and invert-type p-i-n structure (Fig. 1-3d). Recently, a mesoporous p-i-n structure has also been developed (Fig. 1-3b). Due to having many choices for fabrication, the band gap architecture used for determining the material selection of transporting layer, both ETLs and HTLs, and collector material, cathode and anode, for optimizing the best structure of solar cell [100-105]. Many kinds of materials can fabricate ETL and HTL, and these include metal oxide material such as ZnO, SnO₂, Al₂O₃ and NiO_x [106-112] and organic material such as P3HT, PCBM, PEDOT:PSS and PTB7 [113-120].

Due to early era of PVSCs, the problems in the fabrication process still have many point which improvement is necessary. One of the major problems in this type of devices is that they aren't stable in humid conditions [121-122]. This severely affects cells' lifetime. Therefore, some researches try to increase the lifetime of cells using encapsulate technique, changing the perovskite solvent in fabrication or trying to fabricate a two-dimensional perovskite solar cell [123-125]. This problem also has effects on the surface morphology of perovskite when fabricated [126-127]. The other problem with these devices is they are not stable and react with some materials such as silver or CuI, so this type of material can't be fabricated directly on the perovskite layer [128-129].

1.3 Objective of Study

Global warming is currently an international key issue [130-131]. Moreover, the energy produced by petroleum has nearly been exhausted. Therefore, people want to produce energy without fuel. Photovoltaic is one choice for renewable energy. It can produce electricity but does not use oil and therefore does not contribute to global warming. It can convert solar energy to electrical energy. However, solar cell face's problems to do

with efficiency, toxicity and production cost. The thesis dissertation is arranged as shown in Fig. 1-4.

In Chapter 2, Titanium oxide material(TiO_x) is considered. This is commonly material using for material application such as anti-refraction layer, super hydrophobic surface, photocatalyst and electron transporting layer in solar cell (ETL) [132-135]. In this chapter, the TiO_x layers were fabricated by Spray layer-by-layer (spray-LBL) used for ETL in semitransparent organic thin film solar cell [136-138]. The properties of TiO_x when fabricated with spray LBL are explained, and we study the effect of post annealed temperature. Moreover, TiO_x fabricated by spray LBL are also chosen for ETLs layer in OSCs, and we study the post annealed temperature and the changing PCE of OSC devices.

In Chapter 3, OSCs were developed for decreasing the toxicity effect by using organic solvent that is very environmentally-friendly. However, this type of solar cell still has problems, owing to the high cost of materials like PCBM, PTB7 or P3HT [139-141]. The high temperature to fabricated metal oxide layer in OSCs also problem for fabrication. Therefore, one target for this study is tried to decrease the fabrication temperature with safety materials for OSCs. We use the benefit of low absorption wavelength of organics solar cell to fabricated semitransparent organic thin film solar cell [142,143]. The organic thin film solar cell are fabricated on $\text{F:Sn}_2\text{O}_3$ (FTO) glass. Then laminated the back electrode contact with silver nano-network (Ag-NWs). The device structures of this study are $\text{FTO/TiO}_2/\text{P3HT:PCBM/PEDOT:PSS/Ag-NWs}$. Due to benefits of our experiment process, the flexible solar cell can also be fabricated on flexible substrate [144]. This chapter also introduces the fabrication of flexible of OSCs on ITO PEN substrate with structure $\text{ITO PEN/TiO}_2/\text{P3HT:PCBM/ PEDOT:PSS/Ag}$.

To decrease the production cost of photovoltaic, the developed material of photovoltaic materials are required. One option to fabricate low cost solar cell is PVSCs. This type of device can be fabricated with low cost material, a simple fabrication process and low temperature. In chapter 4, PVSCs were fabricated using a two-step method because this technique can improve surface coverage with high reproducibility [145-147]. To finding the “optimum condition” through such a variety of systems in fabricating PVSCs might make the process complicated. This chapter also explains the development of an optimization tool for perovskite layer. The development with the low-temperature fabrication process of PVSCs, based on structure FTO/SnO₂/perovskite/Spiro-ometed/Au, by using Latin hypercube sampling (LHS)[148-150] for Design of experiment(DoE), where we randomly chose only 12 conditions for two factors with 12 levels each. DoE by LHS drastically decreases the number of experiments while keeping the uniformity through the experimental space. After conducting the experiment, we investigated the reasonability of result efficiency via material characterizations such as morphology and crystalline property. Then we utilized kriging model and a fast and elitist multiobjective genetic algorithm (NSGA-II) to model the output efficiency and optimum condition random efficient with a low sampling point [151-153].

The high PCE of PVSCs are demonstrated across multiple independent research studies [65-66]. Most of the reports which improve fabrication method of PVSCs are focused on the small active area, and only few report on large surface (in cm² scale area) fabrication processes [154-155]. However, there are only a few reports of fabricating a large area PVSCs at atmospheric pressure. Such areas face several hindrances: 1) a large amount of incomplete reaction, remain high amount of PbI₂, 2) large amounts of pin-hole in perovskite surface and 3) low reproducibility rate.

In chapter 5, the designed fabrication process of perovskite layer is demonstrated, which is named “dynamic spin-washing method” with a conventional mesoporous-TiO₂ based structure device for a cm² scale area at atmospheric pressure, and humidity of less than 40%. The key for developing a two-step method is “dynamic spin-washing” process after dipping in an MAI solution. This experiment demonstrates that our washing process has benefits to improving the uniformity and quality of perovskite crystalline thin film.

Chapter 6 gives conclusion and implication for future works as a last chapter. Here, the overall conclusion indicates the significance of this thesis.

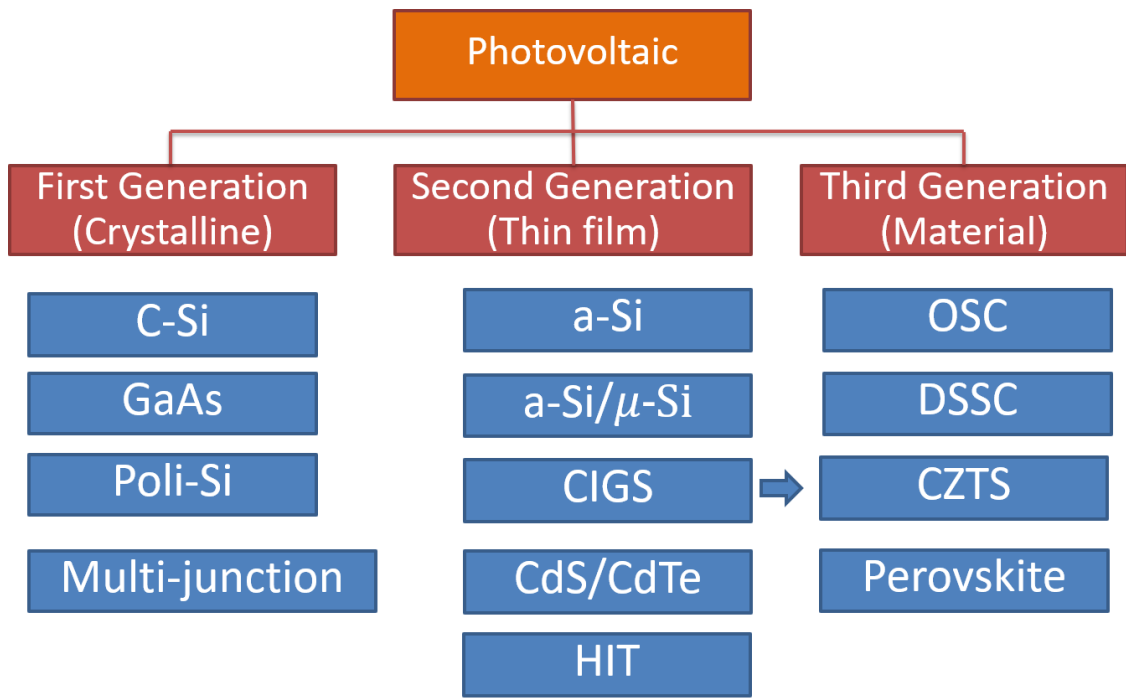


Fig.1-1 Summary of type and generation photovoltaic

Best Research-Cell Efficiencies

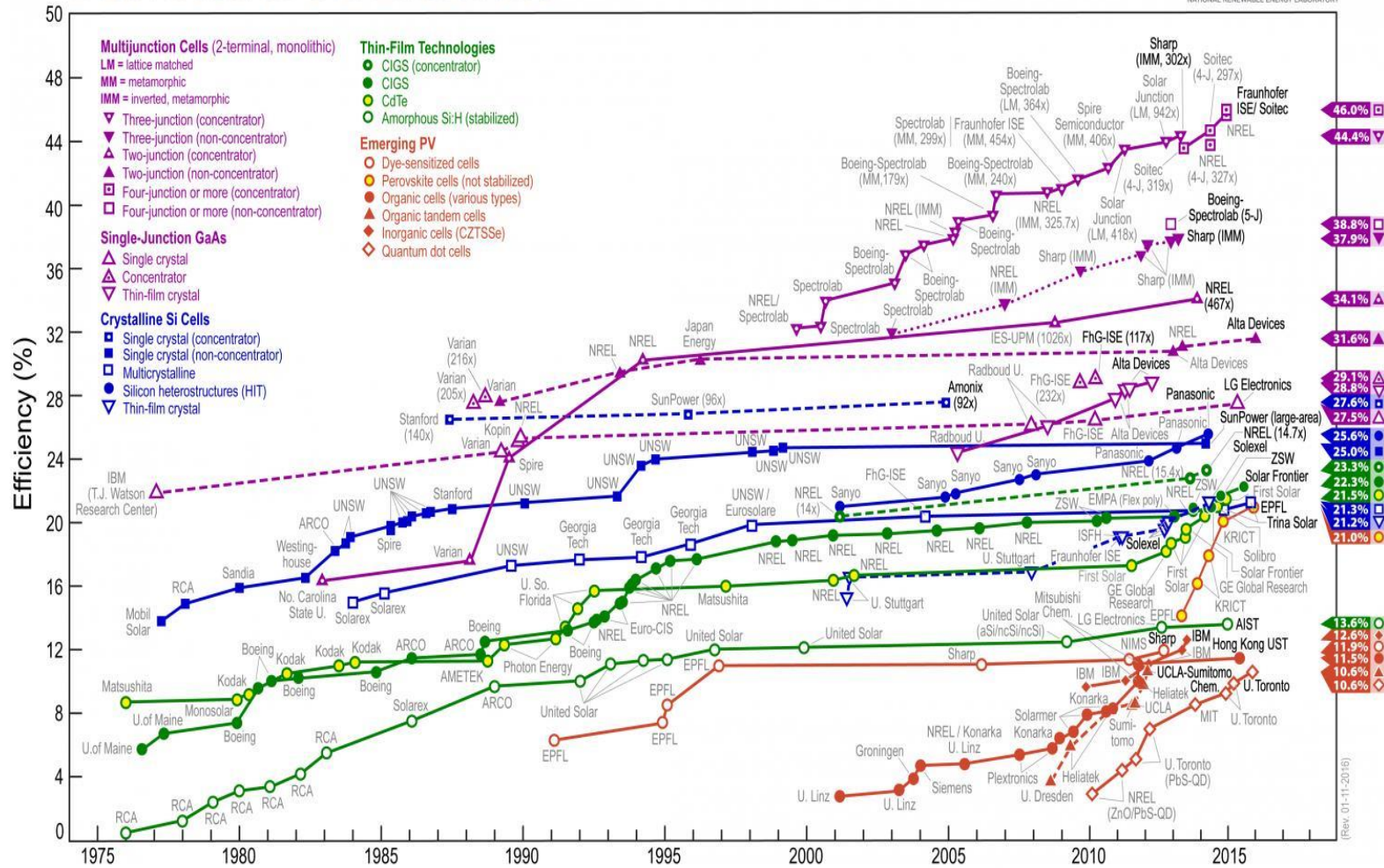


Fig. 1-2 The highest PCE of each type of solar cell with time published by Progress in Photovoltaics [66]

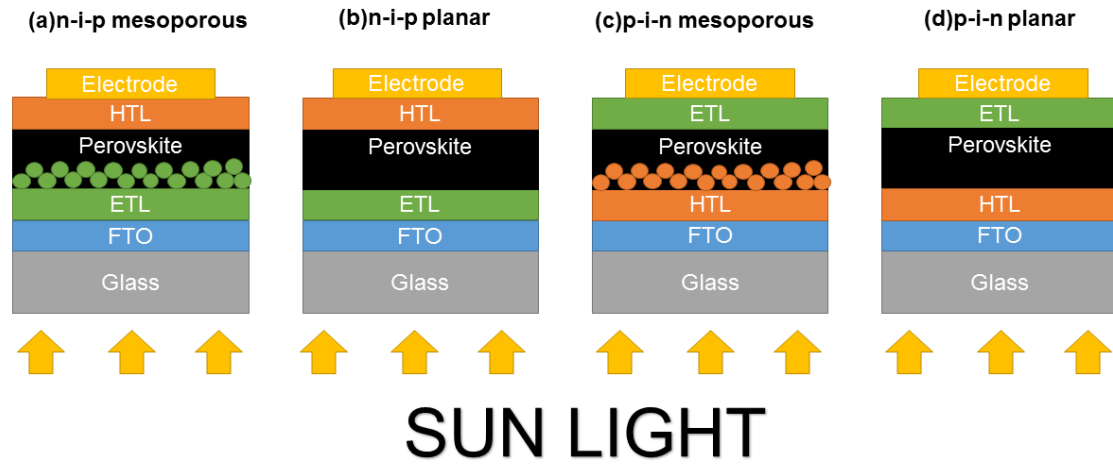


Fig. 1-3 Schematic diagrams of perovskite solar cells in the (a) n-i-p mesoscopic, (b) n-i-p planar, (c) p-i-n planar, and (d) p-i-n mesoscopic structures.

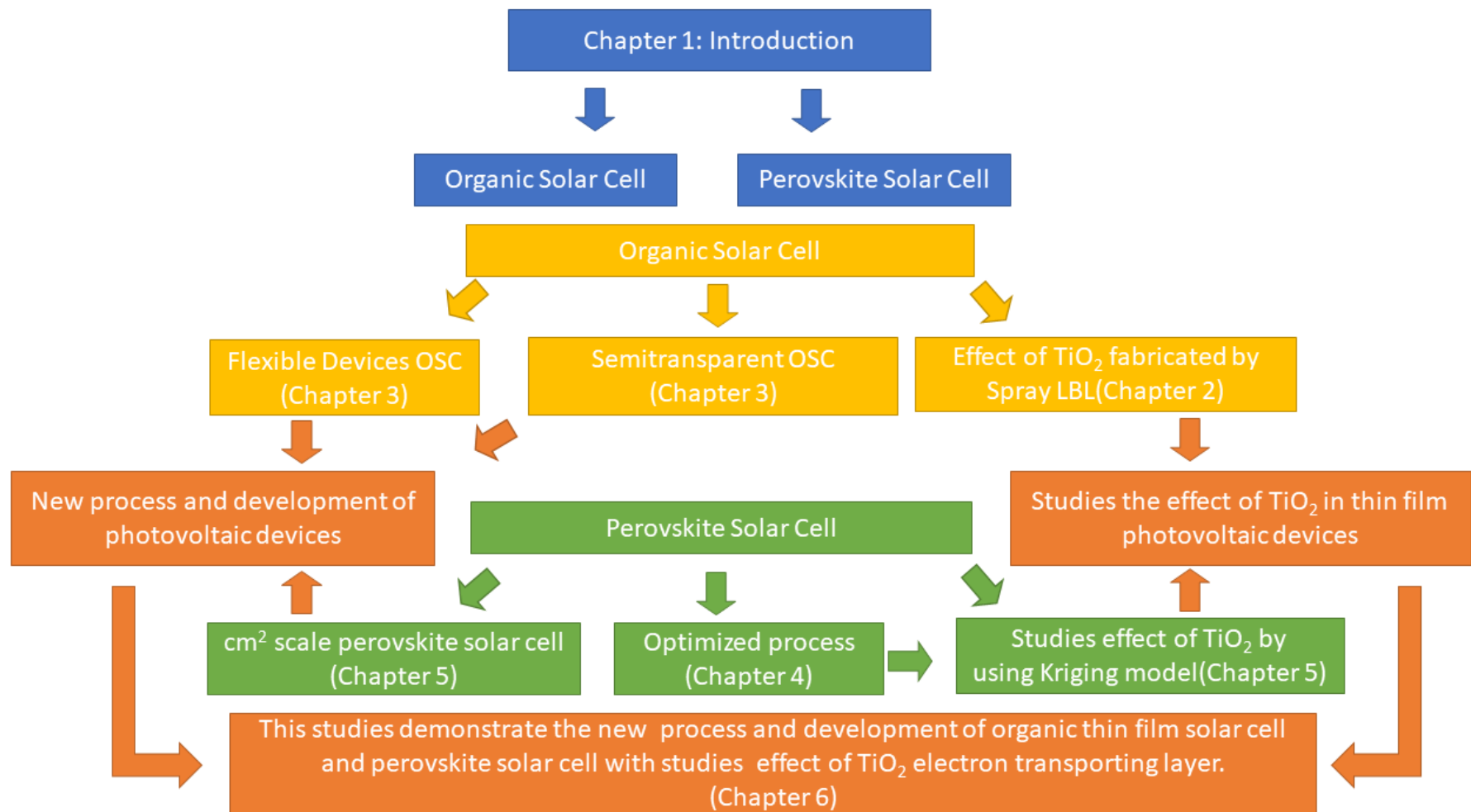


Fig. 1-4 The overview of this thesis

References

- [1-1] APS News. American Physical Society, 2009, 18 (4). April
- [1-2] Chapin, D.M. , Fuller, C.S., Pearson, G.L., *Journal of Applied Physics*, 1954, 25 (5): 676–677.
- [1-3] Zhao, J., Wang, A., Green, M.A. & Ferrazza, F., *Applied Physics Letters*, 1998, 73(14), 1991-1993.
- [1-4] Bergmann, R. B., Berge, C., Rinke, T. J., Schmidt, J., & Werner, J. H., *Solar energy materials and solar cells*, 2002, 74(1), 213-218.
- [1-5] Zolper, J. C., Narayanan, S., Wenham, S. R., & Green, M. A., *Applied Physics Letters*, 1989, 55(22), 2363-2365.
- [1-6] Fuyuki, T., Kondo, H., Yamazaki, T., Takahashi, Y., & Uraoka, Y, *Applied Physics Letters*, 2005, 86(26), 262108.
- [1-7] Algora, C., & Diaz, V., *IEEE Transactions on Electron Devices*, 1998, 45(9), 2047-2054.
- [1-8] Dimroth, F. & Kurtz, S. , *MRS bulletin*, 2007, 32(03), 230-235.
- [1-9] Faine, P., Kurtz, S. R., Riordan, C., & Olson, J. M., *Solar cells*, 1991, 31(3), 259-278.
- [1-10] Takamoto, T., Kaneiwa, M., Imaizumi, M., & Yamaguchi, M., *Progress in Photovoltaics: Research and Applications*, 2005, 13(6), 495-511.
- [1-11] Bertness, K. A., Kurtz, S. R., Friedman, D. J., Kibbler, A. E., Kramer, C., & Olson, J. M., *Applied physics letters*, 1994, 65(8), 989-991.

- [1-12] Carlson, D. E., *IEEE Transactions on Electron Devices*, 1977, 24, 449-453
- [1-13] Carlson, D. E., & Wronski, C. R., *Applied Physics Letters*, 1976, 28(11), 671-673.
- [1-14] Galloni, R., *Renewable energy*, 1996, 8(1), 400-404.
- [1-15] Keppner, H., Meier, J., Torres, P., Fischer, D., & Shah, A., *Applied physics A*, 1999, 69(2), 169-177.
- [1-16] Shah, A., Meier, J., Vallat-Sauvain, E., Droz, C., Kroll, U., Wyrsh, N., Guillet, J. & Graf, U., *Thin Solid Films*, 2002, 403, 179-187.
- [1-17] Ganguly, G., Ikeda, T., Nishimiya, T., Saitoh, K., Kondo, M., & Matsuda, A., *Applied physics letters*, 1996, 69(27), 4224-4226.
- [1-18] Meier, J., Spitznagel, J., Kroll, U., Bucher, C., Fay, S., Moriarty, T., & Shah, A., *Thin Solid Films*, 2004, 451, 518-524.
- [1-19] Meier, J., Dubail, S., Platz, R., Torres, P., Kroll, U., Selvan, J. A., Pellaton Vaucher, N., Hof, Ch., Fischer, D., Keppner, H., Flückiger, R., Shah, A., V. Shklover & Flückiger, R., *Solar Energy materials and Solar cells*, 1997, 49(1), 35-44.
- [1-20] Mishima, T., Taguchi, M., Sakata, H., & Maruyama, E., *Solar Energy Materials and Solar Cells*, 2011, 95(1), 18-21.
- [1-21] Zhao, L., Li, H. L., Zhou, C. L., Diao, H. W., & Wang, W. J., *Solar Energy*, 2009, 83(6), 812-816.
- [1-22] Britt, J., & Ferekides, C., *Applied Physics Letters*, 1993, 62(22), 2851-2852.

- [1-23] Chu, T. L., Chu, S. S., Ferekides, C., Wu, C. Q., Britt, J., & Wang, C., *Journal of applied physics*, 1991, 70(12), 7608-7612.
- [1-24] Gupta, A., & Compaan, A. D., *Applied Physics Letters*, 2004, 85(4), 684-686.
- [1-25] Schmid, D., Ruckh, M., & Schock, H. W. (1994, December), IEEE Photovoltaic Specialists Conference-1994, 1994 IEEE First World Conference on (Vol. 1, pp. 198-201). IEEE.
- [1-26] Kaiser, I., Ernst, K., Fischer, C. H., Könenkamp, R., Rost, C., Sieber, I., & Lux-Steiner, M. C., *Solar Energy Materials and Solar Cells*, 2001, 67(1), 89-96.
- [1-27] Li, L., Coates, N., & Moses, D., *Journal of the American Chemical Society*, 2009, 132(1), 22-23.
- [1-28] Jackson, P., Hariskos, D., Lotter, E., Paetel, S., Wuerz, R., Menner, R., Wischmann, W. & Powalla, M., *Progress in Photovoltaics: Research and Applications*, 2011, 19(7), 894-897.
- [1-29] Naghavi, N., Spiering, S., Powalla, M., Cavana, B., & Lincot, D. , 2003, *Progress in Photovoltaics: Research and Applications* ,11(7), 437-443.
- [1-30] Kessler, F., & Rudmann, D., 2004, *Solar Energy*, 77(6), 685-695.
- [1-31] O'regan, B., & Grfitzeli, M., *nature*, 1991 353(6346), 737-740.
- [1-32] Kay, A., & Grätzel, M., *Solar Energy Materials and Solar Cells*, 1996, 44(1), 99-117.
- [1-33] Guo, M., Xie, K., Lin, J., Yong, Z., Yip, C. T., Zhou, L., Wang, Y. & Huang, H., *Energy & Environmental Science*, 2012, 5(12), 9881-9888.

- [1-34] Daeneke, T., Uemura, Y., Duffy, N. W., Mozer, A. J., Koumura, N., Bach, U., & Spiccia, L., *Advanced Materials*, 2012, 24(9), 1222-1225.
- [1-35] Park, N. G. , *Materials Today*, 2015, 18(2), 65-72.
- [1-36] Peumans, P., Uchida, S., & Forrest, S. R., *Nature*, 2003, 425(6954), 158-162.
- [1-37] Rand, B. P., Peumans, P., & Forrest, S. R. (2004). *Journal of Applied Physics*, 96(12), 7519-7526.
- [1-38] Erb, T., Zhokhavets, U., Gobsch, G., Raleva, S., Stühn, B., Schilinsky, P., Waldauf, C. & Brabec, C. J. (2005)., *Advanced Functional Materials*, 15(7), 1193-1196.
- [1-39] Goris, L., Haenen, K., Nesladek, M., Wagner, P., Vanderzande, D., De Schepper, L., D'haenL, J., Lutsen L. & Manca, J. V. (2005), *Journal of materials science*, 40(6), 1413-1418.
- [1-40] Aernouts, T., Vanlaeke, P., Geens, W., Poortmans, J., Heremans, P., Borghs, S., Mertensa, R., Andriessen, R. & Leenders, L. (2004), *Thin solid films*, 451, 22-25.
- [1-41] Wang, P., Zakeeruddin, S. M., Moser, J. E., Nazeeruddin, M. K., Sekiguchi, T., & Grätzel, M. (2003), *Nature materials*, 2(6), 402-407
- [1-42] Ko, S. H., Lee, D., Kang, H. W., Nam, K. H., Yeo, J. Y., Hong, S. J., Grigoropoulos, C.P. & Sung, H. J. (2011), *Nano letters*, 11(2), 666-671.
- [1-43] Hara, K., Sayama, K., Ohga, Y., Shinpo, A., Suga, S., & Arakawa, H. (2001), *Chemical Communications*, (6), 569-570.
- [1-44] Ennaoui, A., Lux-Steiner, M., Weber, A., Abou-Ras, D., Kötschau, I., Schock, H. W., Schurr, R., Hölzing, A., Jost, S., Hock, R., Voß, T., Schulze, J. & Voß, T. (2009), *Thin Solid Films*, 517(7), 2511-2514.

- [1-45] Katagiri, H., Jimbo, K., Maw, W. S., Oishi, K., Yamazaki, M., Araki, H., & Takeuchi, A. (2009), *Thin Solid Films*, 517(7), 2455-2460.
- [1-46] Ahmed, S., Reuter, K. B., Gunawan, O., Guo, L., Romankiw, L. T., & Deligianni, H. (2012), *Advanced Energy Materials*, 2(2), 253-259.
- [1-47] Jimbo, K., Kimura, R., Kamimura, T., Yamada, S., Maw, W. S., Araki, H., Oishi, K. & Katagiri, H. (2007), *Thin Solid Films*, 515(15), 5997-5999.
- [1-48] Leyden, M. R., Ono, L. K., Raga, S. R., Kato, Y., Wang, S., & Qi, Y. (2014), *Journal of Materials Chemistry A*, 2(44), 18742-18745.
- [1-49] Laban, W. A., & Etgar, L. (2013), *Energy & Environmental Science*, 6(11), 3249-3253.
- [1-50] Zhu, Z., Ma, J., Wang, Z., Mu, C., Fan, Z., Du, L., Bai, Y., Fan, L., Yan, H., Phillips, D.L. & Yang, S. (2014), *Journal of the American Chemical Society*, 136(10), 3760-3763.
- [1-51] Ke, W., Fang, G., Wang, J., Qin, P., Tao, H., Lei, H., Liu, Q., Dai, X. & Zhao, X. (2014), *ACS applied materials & interfaces* 6(18), 15959-15965.
- [1-52] Yan, K., Long, M., Zhang, T., Wei, Z., Chen, H., Yang, S., & Xu, J. (2015), *Journal of the American Chemical Society*, 137(13), 4460-4468.
- [1-53] Green, M. A., Emery, K., Hishikawa, Y., Warta, W., & Dunlop, E. D. (2016), *Progress in Photovoltaics: Research and Applications*, 24(NREL/JA-5J00-65643).
- [1-54] Akamatu, H., Inokuchi, H., & Matsunaga, Y. (1954). *Nature*, 173, 168-169.
- [1-55] Pope, M., & Swenberg, C. E. (1999). *Electronic processes in organic crystals and polymers*. Oxford University Press on Demand.

- [1-56] Chamberlain, G. A. (1983). Organic solar cells: a review. *Solar cells*, 8(1), 47-83.
- [1-57] Tang, C. W. (1986). *Applied Physics Letters*, 48(2), 183-185.
- [1-58] Yu, G., Gao, J., Hummelen, J. C., Wudl, F., & Heeger, A. J. (1995). *Science*, 270(5243), 1789.
- [1-59] Li, G., Shrotriya, V., Huang, J., Yao, Y., Moriarty, T., Emery, K., & Yang, Y. (2005) *Nature materials*, 4(11), 864-868.
- [1-60] Aernouts, T., Aleksandrov, T., Giroto, C., Genoe, J., & Poortmans, J. (2008). *Applied Physics Letters*, 92(3), 033306.
- [1-61] Srinivasan, M. V., Ito, M., Kumar, P., Abhirami, K., Tsuda, N., Yamada, J., Shin, P.K. & Ochiai, S. (2015). *Industrial & Engineering Chemistry Research*, 54(1), 181-187.
- [1-62] Peumans, P., Yakimov, A., & Forrest, S. R. (2003). *Journal of Applied Physics*, 93(7), 3693-3723.
- [1-63] Collins, B. A., Li, Z., Tumbleston, J. R., Gann, E., McNeill, C. R., & Ade, H. (2013). *Advanced Energy Materials*, 3(1), 65-74.
- [1-64] Kojima, A., Teshima, K., Shirai, Y., & Miyasaka, T. (2009). *Journal of the American Chemical Society*, 131(17), 6050-6051.
- [1-65] Lee, M. M., Teuscher, J., Miyasaka, T., Murakami, T. N., & Snaith, H. J. (2012). *Science*, 338(6107), 643-647.
- [1-66] NREL, Best Research-Cell Efficiencies, http://www.nrel.gov/ncpv/images/efficiency_chart.jpg (2015).

- [1-67] Singh, S. P., & Nagarjuna, P. (2014). Dalton Transactions, 43(14), 5247-5251.
- [1-68] Qin, P., Tanaka, S., Ito, S., Tetreault, N., Manabe, K., Nishino, H., Nazeeruddin, K.M. & Grätzel, M. (2014). Nature communications, 5, 1-7
- [1-69] Docampo, P., Ball, J. M., Darwich, M., Eperon, G. E., & Snaith, H. J. (2013). Nature communications, 4.
- [1-70] Lindblad, R., Bi, D., Park, B. W., Oscarsson, J., Gorgoi, M., Siegbahn, H., Odellius, M., Johansson, E.M.J. & Rensmo, H. (2014). The journal of physical chemistry letters, 5(4), 648-653.
- [1-71] Chen, W., Wu, Y., Yue, Y., Liu, J., Zhang, W., Yang, X., Chen, H., Bi, E., Ashraful, I., Grätzel, M. & Han, L. (2015). Science, 350(6263), 944-948.
- [1-72] Razza, S., Di Giacomo, F., Matteocci, F., Cina, L., Palma, A. L., Casaluci, S., Cameron, P., D'Epifanioc, A., Licoccia, S. & Brown, T. M. (2015). Journal of Power Sources, 277, 286-291.
- [1-73] Guo, F., Azimi, H., Hou, Y., Przybilla, T., Hu, M., Bronnbauer, C., Langner, S., Spiecker, E., Forberich, K. & Brabec, C. J. (2015). Nanoscale, 7(5), 1642-1649.
- [1-74] Della Gaspera, E., Peng, Y., Hou, Q., Spiccia, L., Bach, U., Jasieniak, J. J., & Cheng, Y. B. (2015). Nano Energy, 13, 249-257.
- [1-75] Roldán-Carmona, C., Malinkiewicz, O., Soriano, A., Espallargas, G. M., Garcia, A., Reinecke, P., Kroyer, T., Dar, M. I., Nazeeruddin, K.N. & Bolink, H. J. (2014). Energy & Environmental Science, 7(3), 994-997.
- [1-76] Jung, J. W., Williams, S. T., & Jen, A. K. Y. (2014). RSC Advances, 4(108), 62971-62977.

- [1-77] Liu, M., Johnston, M. B., & Snaith, H. J. (2013). *Nature*, 501(7467), 395-398.
- [1-78] Wang, Q., Shao, Y., Dong, Q., Xiao, Z., Yuan, Y., & Huang, J. (2014). *Energy & Environmental Science*, 7(7), 2359-2365.
- [1-79] Barrows, A. T., Pearson, A. J., Kwak, C. K., Dunbar, A. D., Buckley, A. R., & Lidzey, D. G. (2014). *Energy & Environmental Science*, 7(9), 2944-2950.
- [1-80] Das, S., Yang, B., Gu, G., Joshi, P. C., Ivanov, I. N., Rouleau, C. M., Aytug, T., Geohegan, D.B. & Xiao, K. (2015). *ACS Photonics*, 2(6), 680-686.
- [1-81] Noh, J. H., Im, S. H., Heo, J. H., Mandal, T. N., & Seok, S. I. (2013). *Nano letters*, 13(4), 1764-1769.
- [1-82] Eperon, G. E., Stranks, S. D., Menelaou, C., Johnston, M. B., Herz, L. M., & Snaith, H. J. (2014). *Energy & Environmental Science*, 7(3), 982-988.
- [1-83] Yin, W. J., Shi, T., & Yan, Y. (2014). *Advanced Materials*, 26(27), 4653-4658.
- [1-84] De Wolf, S., Holovsky, J., Moon, S. J., Löper, P., Niesen, B., Ledinsky, M., Haug, F.J., Yum, J.H. & Ballif, C. (2014). *The journal of physical chemistry letters*, 5(6), 1035-1039.
- [1-85] Stranks, S. D., Eperon, G. E., Grancini, G., Menelaou, C., Alcocer, M. J., Leijtens, T., Herz, L.M., Petrozza, A. & Snaith, H. J. (2013). *Science*, 342(6156), 341-344.
- [1-86] Wehrenfennig, C., Eperon, G. E., Johnston, M. B., Snaith, H. J., & Herz, L. M. (2014). *Advanced materials*, 26(10), 1584-1589.
- [1-87] Yin, W. J., Shi, T., & Yan, Y. (2014). *Applied Physics Letters*, 104(6), 063903.

- [1-88] Sutton, R. J., Eperon, G. E., Miranda, L., Parrott, E. S., Kamino, B. A., Patel, J. B., Hörantner, M.T., Johnston, M.B., Haghighirad, A.B., Moore, D.T. & Snaith, H. J. (2016) *Advanced Energy Materials*, 6, 1502458
- [1-89] Chen, D., Huang, F., Cheng, Y. B., & Caruso, R. A. (2009). *Advanced Materials*, 21(21), 2206-2210.
- [1-90] Koo, H. J., Kim, Y. J., Lee, Y. H., Lee, W. I., Kim, K., & Park, N. G. (2008). *Advanced Materials*, 20(1), 195-199.
- [1-91] Yamada, Y., Nakamura, T., Endo, M., Wakamiya, A., & Kanemitsu, Y. (2014). *Applied Physics Express*, 7(3), 032302.
- [1-92] Edri, E., Kirmayer, S., Henning, A., Mukhopadhyay, S., Gartsman, K., Rosenwaks, Y., Hodes, G. & Cahen, D. (2014). *Nano letters*, 14(2), 1000-1004.
- [1-93] Leijtens, T., Lauber, B., Eperon, G. E., Stranks, S. D., & Snaith, H. J. (2014). *The journal of physical chemistry letters*, 5(7), 1096-1102.
- [1-94] Jeon, N. J., Lee, H. G., Kim, Y. C., Seo, J., Noh, J. H., Lee, J., & Seok, S. I. (2014). *Journal of the American Chemical Society*, 136(22), 7837-7840.
- [1-95] Lindblad, R., Bi, D., Park, B. W., Oscarsson, J., Gorgoi, M., Siegbahn, H., Odellius, M., Johansson, E.M.J. & Rensmo, H. (2014). *The journal of physical chemistry letters*, 5(4), 648-653.
- [1-96] Jena, A. K., Chen, H. W., Kogo, A., Sanehira, Y., Ikegami, M., & Miyasaka, T. (2015). *ACS applied materials & interfaces*, 7(18), 9817-9823.
- [1-97] Liang, P. W., Liao, C. Y., Chueh, C. C., Zuo, F., Williams, S. T., Xin, X. K., Lin, J.J. & Jen, A. K. Y. (2014). *Advanced Materials*, 26(22), 3748-3754.

- [1-98] Leijtens, T., Stranks, S. D., Eperon, G. E., Lindblad, R., Johansson, E. M., McPherson, I. J., Rensmo, H.K., Ball, J.M., Lee, M.M. & Snaith, H. J. (2014). *ACS nano*, 8(7), 7147-7155.
- [1-99] Heo, J. H., Han, H. J., Kim, D., Ahn, T. K., & Im, S. H. (2015). *Energy & Environmental Science*, 8(5), 1602-1608.
- [1-100] Hao, F., Stoumpos, C. C., Chang, R. P., & Kanatzidis, M. G. (2014). *Journal of the American Chemical Society*, 136(22), 8094-8099.
- [1-101] Conings, B., Baeten, L., De Dobbelaere, C., D'Haen, J., Manca, J., & Boyen, H. G. (2014). *Advanced Materials*, 26(13), 2041-2046.
- [1-102] Ito, S., Tanaka, S., Manabe, K., & Nishino, H. (2014). *The Journal of Physical Chemistry C*, 118(30), 16995-17000.
- [1-103] Liu, L., Mei, A., Liu, T., Jiang, P., Sheng, Y., Zhang, L., & Han, H. (2015). *Journal of the American Chemical Society*, 137(5), 1790-1793.
- [1-104] Chen, W., Wu, Y., Liu, J., Qin, C., Yang, X., Islam, A., Cheng, Y.B. & Han, L. (2015). *Energy & Environmental Science*, 8(2), 629-640.
- [1-105] Liu, M., Johnston, M. B., & Snaith, H. J. (2013). *Nature*, 501(7467), 395-398.
- [1-106] Liu, D., & Kelly, T. L. (2014). *Nature photonics*, 8(2), 133-138.
- [1-107] Kumar, M. H., Yantara, N., Dharani, S., Graetzel, M., Mhaisalkar, S., Boix, P. P., & Mathews, N. (2013). *Chemical Communications*, 49(94), 11089-11091.
- [1-108] Li, Y., Zhu, J., Huang, Y., Liu, F., Lv, M., Chen, S., Hu, L., Tang, J., Yao, J. & Dai, S. (2015). *RSC Advances*, 5(36), 28424-28429.

- [1-109] Rao, H. S., Chen, B. X., Li, W. G., Xu, Y. F., Chen, H. Y., Kuang, D. B., & Su, C. Y. (2015). *Advanced Functional Materials*, 25(46), 7200-7207.
- [1-109] Li, W., Li, J., Wang, L., Niu, G., Gao, R., & Qiu, Y. (2013). *Journal of Materials Chemistry A*, 1(38), 11735-11740.
- [1-110] Pachoumi, O., Li, C., Vaynzof, Y., Banger, K. K., & Sirringhaus, H. (2013). *Advanced Energy Materials*, 3(11), 1428-1436.
- [1-111] Wang, K. C., Shen, P. S., Li, M. H., Chen, S., Lin, M. W., Chen, P., & Guo, T. F. (2014). *ACS applied materials & interfaces*, 6(15), 11851-11858.
- [1-112] Jeng, J. Y., Chen, K. C., Chiang, T. Y., Lin, P. Y., Tsai, T. D., Chang, Y. C., Guo, F.G., Chen, P., Wen, T.C. & Hsu, Y. J. (2014). *Advanced materials*, 26(24), 4107-4113.
- [1-113] Di Giacomo, F., Razza, S., Matteocci, F., D'Epifanio, A., Licoccia, S., Brown, T. M., & Di Carlo, A. (2014). *Journal of Power Sources*, 251, 152-156.
- [1-114] Zhu, Z., Ma, J., Wang, Z., Mu, C., Fan, Z., Du, L., Bai, Y., Fan, L., Yan, H., Phillips, D.L. & Yang, S. (2014). *Journal of the American Chemical Society*, 136(10), 3760-3763.
- [1-115] Seo, J., Park, S., Kim, Y. C., Jeon, N. J., Noh, J. H., Yoon, S. C., & Seok, S. I. (2014). *Energy & Environmental Science*, 7(8), 2642-2646.
- [1-116] Roldán-Carmona, C., Malinkiewicz, O., Soriano, A., Espallargas, G. M., Garcia, A., Reinecke, P., Kroyer, T., Dar, M.I., Nazeeruddin, M.K. & Bolink, H. J. (2014). *Energy & Environmental Science*, 7(3), 994-997.

- [1-117] Liang, P. W., Liao, C. Y., Chueh, C. C., Zuo, F., Williams, S. T., Xin, X. K., Lin, J. & Jen, A. K. Y. (2014). *Advanced Materials*, 26(22), 3748-3754.
- [1-118] Yun, J. M., Yeo, J. S., Kim, J., Jeong, H. G., Kim, D. Y., Noh, Y. J., Kim, S.S., Ku, B.C. & Na, S. I. (2011). *Advanced Materials*, 23(42), 4923-4928.
- [1-119] J. Kim, G. Kim, T. K. Kim, S. Kwon, H. Back, J. Lee, S. H. Lee, H. Kang and K. Lee, *J. Mater. Chem. A*, 2014, 2, 17291–17296
- [1-120] Baumann, A., Tvingstedt, K., Heiber, M. C., V  th, S., Momblona, C., Bolink, H. J., & Dyakonov, V. (2014). *Apl Materials*, 2(8), 081501.
- [1-121] Han, Y., Meyer, S., Dkhissi, Y., Weber, K., Pringle, J. M., Bach, U., Spiccia, L. & Cheng, Y. B. (2015). *Journal of Materials Chemistry A*, 3(15), 8139-8147.
- [1-122] Dong, X., Fang, X., Lv, M., Lin, B., Zhang, S., Ding, J., & Yuan, N. (2015). *Journal of Materials Chemistry A*, 3(10), 5360-5367.
- [1-123] Weerasinghe, H. C., Dkhissi, Y., Scully, A. D., Caruso, R. A., & Cheng, Y. B. (2015). *Nano Energy*, 18, 118-125.
- [1-124] Dong, Q., Liu, F., Wong, M. K., Tam, H. W., Djurišić, A. B., Ng, A., Surya, C., Chan, W. & Ng, A. M. C. (2016). *ChemSusChem*, 9(18), 2597-2603.
- [1-125] Liu, J., Xue, Y., Wang, Z., Xu, Z. Q., Zheng, C., Weber, B., Song, J., Wang, Y., Lu, Y., Zhang, Y. & Bao, Q. (2016). *ACS nano*, 10(3), 3536-3542.
- [1-126] You, J., Yang, Y. M., Hong, Z., Song, T. B., Meng, L., Liu, Y., Jiang, C., Zhou, H., Chang, W.H., Li, G. & Yang, Y. (2014). *Applied Physics Letters*, 105(18), 183902.

- [1-127] Ko, H. S., Lee, J. W., & Park, N. G. (2015). *Journal of Materials Chemistry A*, 3(16), 8808-8815.
- [1-128] Kato, Y., Ono, L. K., Lee, M. V., Wang, S., Raga, S. R., & Qi, Y. (2015). *Advanced Materials Interfaces*, 2(13).
- [1-129] Christians, J. A., Fung, R. C., & Kamat, P. V. (2013). *Journal of the American Chemical Society*, 136(2), 758-764.
- [1-130] Jacobson, M. Z. (2009). *Energy & Environmental Science*, 2(2), 148-173.
- [1-131] Dincer, F. (2011). *Renewable and Sustainable Energy Reviews*, 15(1), 713-720.
- [1-132] Kim, J. H., Fujita, S., & Shiratori, S. (2006). *Thin Solid Films*, 499(1), 83-89.
- [1-133] Kim, J. H., Kim, S. H., & Shiratori, S. (2004). *Sensors and Actuators B: Chemical*, 102(2), 241-247.
- [1-134] Chigane, M., & Shinagawa, T. (2012). *Thin Solid Films*, 520(9), 3510-3514.
- [1-135] Ray, S., & Lalman, J. A. (2016). *Materials Today: Proceedings*, 3(6), 1582-1591.
- [1-136] Nogueira, G. M., Banerjee, D., Cohen, R. E., & Rubner, M. F. (2011). *Langmuir*, 27(12), 7860-7867.
- [1-137] Saetia, K., Schnorr, J. M., Mannarino, M. M., Kim, S. Y., Rutledge, G. C., Swager, T. M., & Hammond, P. T. (2014). *Advanced Functional Materials*, 24(4), 492-502.
- [1-138] Kim, S. Y., Hong, J., Kaviani, R., Lee, S. W., Hyder, M. N., Shao-Horn, Y., & Hammond, P. T. (2013). *Energy & Environmental Science*, 6(3), 888-897.

- [1-139] Kuwabara, T., Iwata, C., Yamaguchi, T., & Takahashi, K. (2010). ACS applied materials & interfaces, 2(8), 2254-2260.
- [1-140] Wienk, M. M., Kroon, J. M., Verhees, W. J., Knol, J., Hummelen, J. C., van Hal, P. A., & Janssen, R. A. (2003). Angewandte Chemie, 115(29), 3493-3497.
- [1-141] Kuwabara, T., Sugiyama, H., Yamaguchi, T., & Takahashi, K. (2009). Thin Solid Films, 517(13), 3766-3769.
- [1-142] Lee, J. Y., Connor, S. T., Cui, Y., & Peumans, P. (2010). Nano letters, 10(4), 1276-1279.
- [1-143] Seemann, A., Egelhaaf, H. J., Brabec, C. J., & Hauch, J. A. (2009). Organic Electronics, 10(8), 1424-1428.
- [1-144] Shimada, C., & Shiratori, S. (2013), 5(21), 11087-11092.
- [1-145] Chen, C. W., Kang, H. W., Hsiao, S. Y., Yang, P. F., Chiang, K. M., & Lin, H. W. (2014). Advanced Materials, 26(38), 6647-6652.
- [1-146] Jeon, Y. J., Lee, S., Kang, R., Kim, J. E., Yeo, J. S., Lee, S. H., Kim, S.S., Yun, J.M. & Kim, D. Y. (2014). Scientific reports, 6953, 4.
- [1-147] Chen, W., Wu, Y., Liu, J., Qin, C., Yang, X., Islam, A., Cheng, Y.B. & Han, L. (2015). Energy & Environmental Science, 8(2), 629-640.
- [1-148] Stein, M. (1987). Technometrics, 29(2), 143-151.
- [1-149] Huntington, D. E., & Lyrantzis, C. S. (1998). Probabilistic engineering mechanics, 13(4), 245-253.
- [1-150] Davey, K. R. (2008). IEEE Transactions on Magnetism, 44(6), 974-977.

[1-151] Cattle, J. A., McBratney, A., & Minasny, B. (2002). *Journal of Environmental Quality*, 31(5), 1576-1588.

[1-152] Gu, Y., Wang, Q. X., & Lam, K. Y. (2007). *Computer Methods in Applied Mechanics and Engineering*, 196(9), 1673-1684.

[1-153] Deb, K., Pratap, A., Agarwal, S., & Meyarivan, T. A. M. T. (2002). *IEEE transactions on evolutionary computation*, 6(2), 182-197.

[1-154] Li, X., Bi, D., Yi, C., Décoppet, J. D., Luo, J., Zakeeruddin, S. M., Hagfeldt, A. & Grätzel, M, (2016). *Science*, 353(6294), 58-62.

[1-155] Gouda, L., Gottesman, R., Tirosh, S., Haltzi, E., Hu, J., Ginsburg, A., Keller, D.A., Bouhadana, Y. & Zaban, A, (2016). *Nanoscale*, 8(12), 6386-6392.

Chapter 2

Titanium Dioxide Layer in Organic Thin Film Solar cell

2.1 Introduction

Titanium dioxide (TiO_2) is one of the most popular materials to use for many applications like anti-refraction layer, photocatalytic, super-hydrophobic and electron transport layer in solar cells, [1-4] its because of high band gap, high chemical and optical stabilities, non-toxicity, low cost and corrosion resistance. [5-7] There are four common crystal structures found in nature; i.e. Anatase(tetragonal), Rutile(tetragonal), brookite (orthorhombic), and $\text{TiO}_2(\text{B})$ (monoclinic). [8-10] However only Anatase and Rutile phases are acceptable to use for electron transport layer in photovoltaic.[11-12] TiO_2 Rutile phase is the most thermodynamically stable of TiO_2 at all temperature, the total free energy of it is lower than metastable phase of anatase and brookite. Anatase phase is the best TiO_2 structure for photovoltaic application due to high conduction band edge energy and lower recombination of electron-hole pairs. [13]

In the previous studies, the TiO_2 layer has been prepared from toxic materials such as TiCl_4 and TiF_4 , [14-15] which should constrict industrialization from the perspective of safety, short fabrication time and applications for large area devices. Poly (diallyldimethylammonium chloride) (PDDA), titanium (IV) bis (ammonium lactato) dihydroxide (TALH) was selected for this experiment to deposit TiO_2 layer on FTO substrate.

In this chapter, TiO₂ fabricated by spray LBL with water base and non-toxic pollution are used for ETLs in organic solar. This chapter also studies the effect of film thickness and annealed temperature related with the photovoltaic performance.

2.2 Experiment

2.2.1 TiO₂ electron transport layers

In this experiment, we fabricated TiO₂ for organic solar cell by Spray-LBL. An automatic spray-LBL machine was developed in our previous research. To prepare a single bilayer, the FTO glass and the glass substrate were alternately sprayed with a PDDA cationic solution (10 mM, pH 5.5) and a TALH anionic suspension (0.1 wt.%, pH 3.5), and were rinsed three times with pure water after deposition of each layer. The film thickness was controlled by controlling the number of bilayers that were applied. The spray conditions including a spray nozzle diameter of 1.2 mm, droplet sizes in the 10–100 μm range, solution and water flow rates adjusted to 4.0 mL/min. The distance between substrate and nozzle was fixed at 15 cm, and the spray pressure was controlled at 0.05 MPa. After precursor film preparation by spray-LBL, the samples were annealed at various temperatures (300, 350, 400, 450 and 500°C) for 60 min to prepare titanium dioxide layers.

2.2.2 Characterization

Field emission scanning electron microscope (FE-SEM) images were taken using a FE-SEM (S-4700, Hitachi, Japan) with an accelerating voltage of 5 kV to characterize the surface topography of the films. Film thickness and the refractive index of the thin films coated on the substrates were determined by ellipsometry (MARY-102, Five Lab, Japan) and film thickness measurements (Dektak; 3030, ULVAC, Japan). Transmittance in the

spectral range of 200 to 1000 nm were measured by a spectrophotometer (UVmini-1240, Shimadzu, Japan). Haze values of the films were measured by a haze meter (NDH-5000, Nippon Denshoku Industries, Tokyo, Japan) with a white light-emitting diode (5 V, 3 W) as an optical source. Crystallization of TiO₂ layer was analyzed by a XRD (D8, DISCOVER, Bruker, Japan) with Cu K α radiation (40 kV, 40 mA), at a scan rate and a step size of 2°/min and 0.01°, respectively. The surface elemental composition of samples was identified by X-ray photoelectron spectroscopy (XPS: JEOL JPS-9000MX).

2.3 Result and Discussion

2.3.1 Temperature dependent of TiO₂ by spray LBL

The Spray-LBL process consisted of four steps for one bilayer: 1) spraying of cations; 2) first rinse; 3) spraying of anions; and 4) second rinse, which promoted uniform film growth with 5 nm film thickness per bilayer (**Fig.2-1**). Based on the difference in mass for a single bilayer (**Fig. 2-2**), the growth rate of spray TALH layer was higher than spray PDDA layer solution.

The crystalline structures of the TiO₂ films that were deposited on glass after the spray-LBL and annealing processes at different temperatures were analyzed using XRD measurements (**Fig. 2-3**). The film changed into an amorphous form at annealing temperatures of more than 450°C. The main peaks of the two-theta angles at approximately 37.36° and 43.59° corresponded to anatase (004) and rutile (210) phases, respectively. The anatase and rutile phase are forming by mainly component of TiO₂ tetragonal structure in TALH precursors. After precursors dilute with water and coating on the substrate, the TiO₂ tetragonal are arrangements of rutile and anatase.[16] The crystalline formation arrangement mechanism is show in **Fig. 2-4**. The crystalline sizes

of anatase (004) and rutile (210) phases at the different annealing temperatures were determined using Debye-Scherrer's formula (**Fig. 2-3**, **Fig. 2-5** and **Table 2-1**):

$$D = k\lambda/(\beta\cos\theta) \quad [2-1]$$

where D is the crystalline size, λ is the wavelength of the Cu K α X-ray source, which was equal to 0.154 nm, k is shape factor equal 0.9, β is the full width at half maximum of the peak and θ is the maximum peak angle. The crystalline size of the anatase phase was higher because the PDDA compound evaporated at annealing temperatures lower than 300°C.[17] In the case of annealing temperatures of between 300°C and 400°C, the crystalline content of the anatase phase and the rutile phase were both reduced because of thermal decomposition. In particular, annealing at temperatures between 310°C and 385°C caused low evaporation rates in terms of weight loss, and the crystalline sizes after annealing at between 300°C and 400°C were also reduced, which indicated that the TiO₂ structure was mixed with the PDDA compound and formed a metal-organic structure. In the case where the annealing temperature was higher than 450°C, the crystalline size was large and changed into an amorphous form, because the PDDA compound was completely evaporated at approximately 415°C. Therefore, in this temperature range, the thin films contained only the TiO₂ compound. However, in this annealing temperature range, the crystallinity of TiO₂ was again reduced because of the calcination effect

XPS measurements were performed to investigate the effects of the different annealing temperatures on crystalline change and to confirm the changing crystallization of the amorphous TiO₂ nanoparticles at temperatures of more than 400°C (**Fig. 2-6**). The oxygen peaks at 530 eV and 531.5 eV, which corresponded to O²⁻ and OH⁻, derived from the oxygen component of the TiO₂ nanoparticle and the hydroxyl group of titanium ammonium lactate, respectively.[18] After annealing, the intensity at the OH⁻ peak was

reduced and that at the O^{2-} peak was increased because of the oxidation effects of the titanium ammonium lactate component containing the OH^- compound in this chemical functional group in the films. The OH^- component has been found to be acceptable for inverted organic solar cells in previous reports.[19] The titanium ammonium lactate was changed into titanium dioxide according to the XPS peak, which showed the high quality TiO_2 thin film crystallization at annealing temperatures higher than $450^\circ C$. These results and the associated discussion were supported by the results of previous research,[20] which resulted in the oxidation of titanium nitride at annealing temperatures higher than $400^\circ C$.

The surface morphologies of the TiO_2 films deposited on glass before and after annealing at the different temperatures are shown in **Fig. 2-7**. The film surfaces consisted of titanium oxide nanoparticles. As the annealing temperature increased, more of the PDDA compound evaporated, which indicated that the more porous film structure was derived from the nanoparticles on the surfaces of the films. The thin film roughness also increased with increasing annealing temperature, because the crystalline sizes of the rutile and anatase phases were dependent on the annealing temperature. The high surface roughness can increase the efficiency of the resulting solar cells,[21] and therefore was appropriate for use in solar cells. The surface morphology of the TiO_2 layer deposited on FTO glass after annealing at $450^\circ C$ is shown in **Fig. 2-8**. The surface roughness and the sizes of the TiO_2 nanoparticles on FTO glass were larger and the films were more porous than those fabricated on the glass substrates. (**Fig. 2-9**)

2.3.2 Optical properties of TiO_2 fabricated by spray LBL

Fig. 2-10 shows the transmittance of a TiO_2 layer on a glass substrate. The transmittance of the TiO_2 layer before annealing showed the highest value, because the polymer

compound was blended with the titanium dioxide layer and reduced the refractive index. However, with increasing annealing temperature, the transmittance was reduced, because the polymer compound in the film evaporated and the refractive index thus increased. The refractive index increased from 1.68 (before annealing) to 1.90 (after 350°C anneal). The refractive index, the haze value and the energy band gap are shown in **Table 2-3**. The haze value was saturated at temperatures higher than 350°C.

A Tauc plot is shown in **Fig. 2-11** that can be used to indicate the energy band gap from the following relation:

$$\alpha h\nu = A(h\nu - E_g)^2 \quad [2-2]$$

where α is the absorption coefficient determined from the transmittance value, $h\nu$ is the optical energy, A is a constant and E_g is the optical band gap. The energy band gap also depended on the annealing temperature, and it was reduced from 3.30 eV in the as-deposited case to 3.20 eV at annealing temperatures of around 350°C. This result corresponds with the XRD results: the energy band gap has a relationship with the crystalline quality of the TiO₂ layer, where the crystalline quality can be determined based on the full width at half-maximum (FWHM) of the XRD data (**Fig. 2-4**). The reduction in the energy band gap was caused by the evaporation and thermal decomposition of the polymer component in the TiO₂ layer. The reduction of the crystalline quality of the rutile type and contrasting increase in crystalline quality of the anatase phase can be estimated from the XRD analysis, which was explained earlier. For annealing temperatures higher than 350°C, the optical energy band gap was stable at around 3.20 eV, corresponding to the energy band gap of the anatase and rutile phases of titanium dioxide.[21] Also, the haze value of TiO₂ on FTO increased after annealing (Table 3-2) because the PDDA

compound evaporated after annealing and was replaced by air gaps that produced a more porous structure in the thin films.

2.4 Conclusion

We have successfully fabricated TiO₂ electron transport layers, based on PDDA and TALH from a water-based solution, via the spray-LBL method for solar cell applications. The titanium dioxide structure deposited on glass by the spray-LBL method was composed of both anatase (004) and rutile (210) phases. The largest crystalline sizes of the anatase (004) and rutile (210) phases were achieved after annealing at 450°C and without annealing, respectively. Before annealing, the films had high surface roughness that was derived from the titanium nanoparticles. After an increase in the annealing temperature, the film refractive index was increased by increasing the high crystallinity of TiO₂, and the haze value was also increased because of the formation of a porous structure in the film. The optical energy band gap was reduced from 3.30 eV to 3.20 eV.

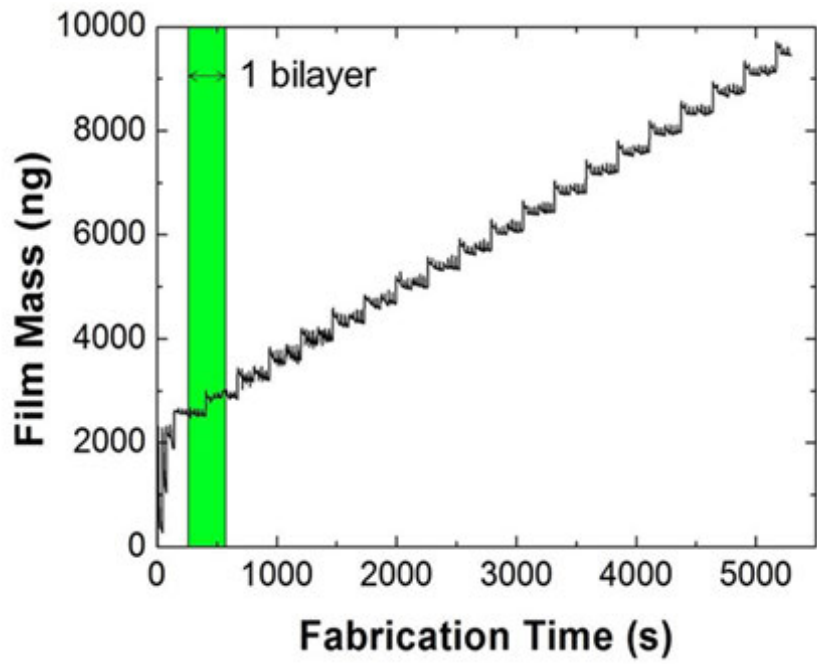


Fig. 2-1 Mass difference of 20 TALH/PDDA bilayers using quartz crystal microbalance (QCM) measurements.

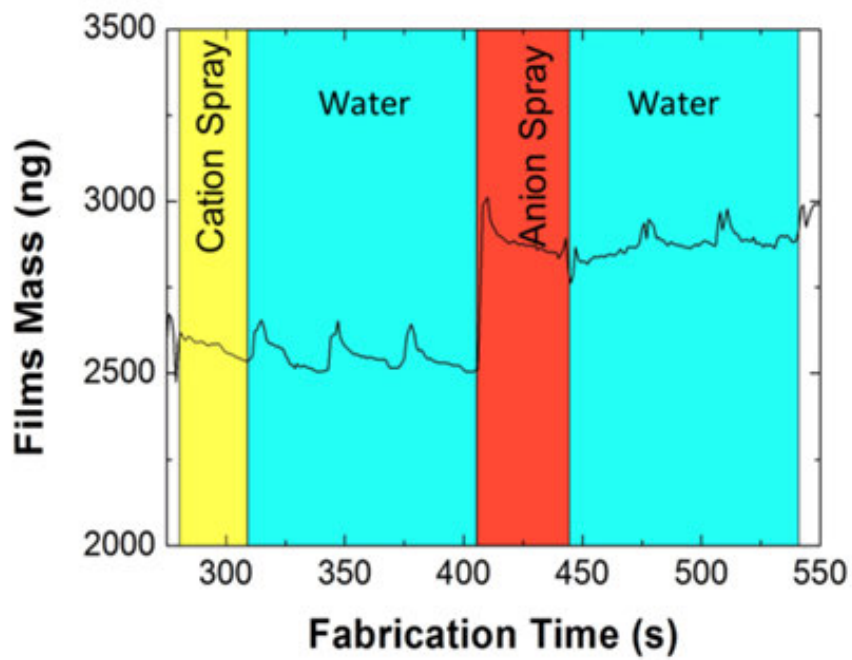


Fig. 2-2 Mass difference of one TALH/PDDA bilayer using QCM measurements

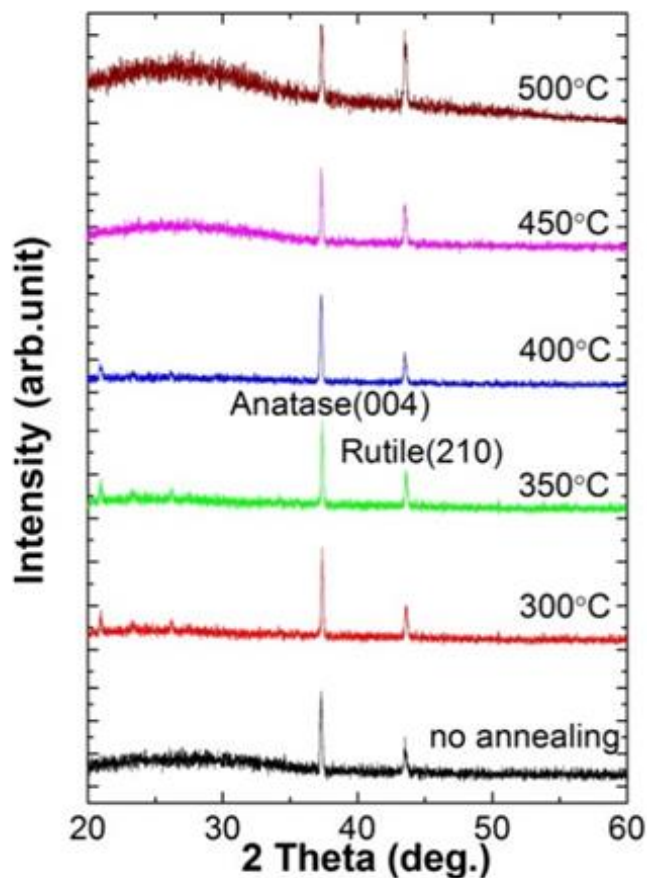


Fig. 2-3 XRD results for titanium dioxide layers fabricated using the spray-LBL method after annealing at different temperatures.

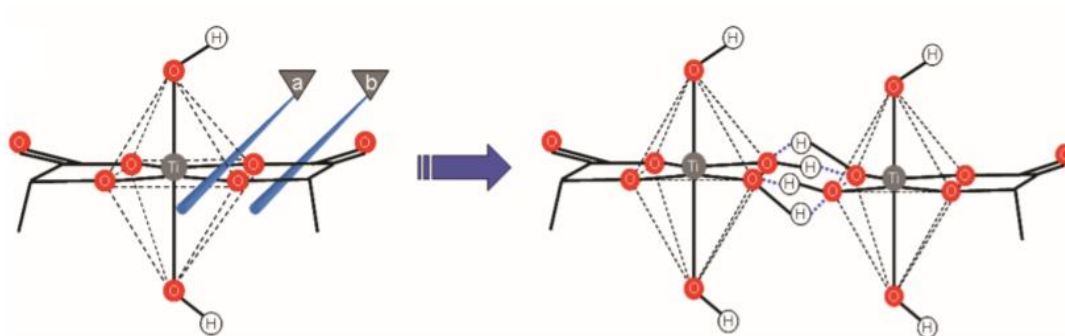
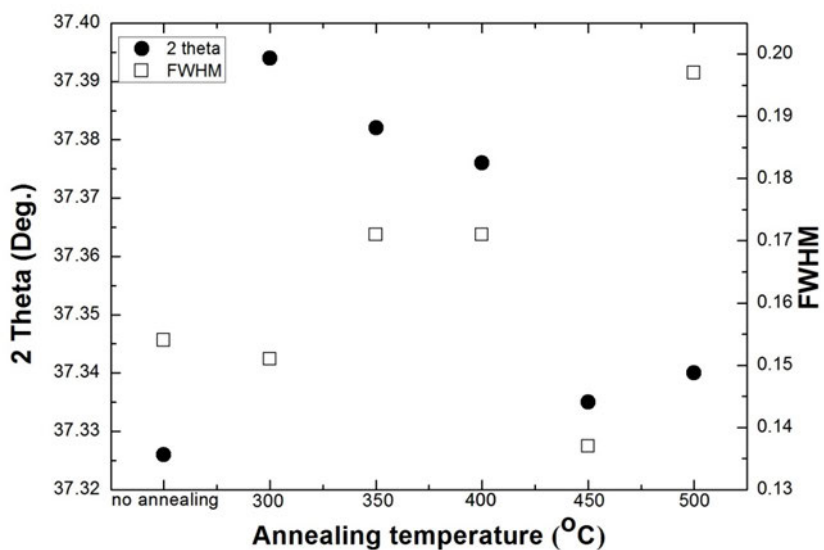
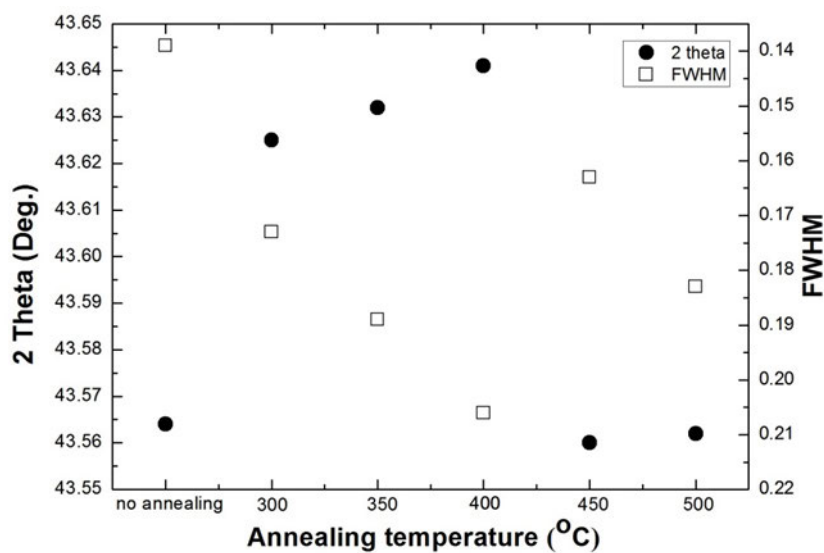


Fig. 2-4 The crystalline formation arrangement mechanism of TALH precursor to mix rutile and anatase thin film. Reprinted with permission from [16] Copyright 2015, American Chemical Society.



(a)



(b)

Fig. 2-5 2Theta and FWHM of (a) TiO₂ anatase phase(004) and (b) TiO₂ rutile phase(210) when fabricated with Spray LBL on glass and annealing at difference temperature

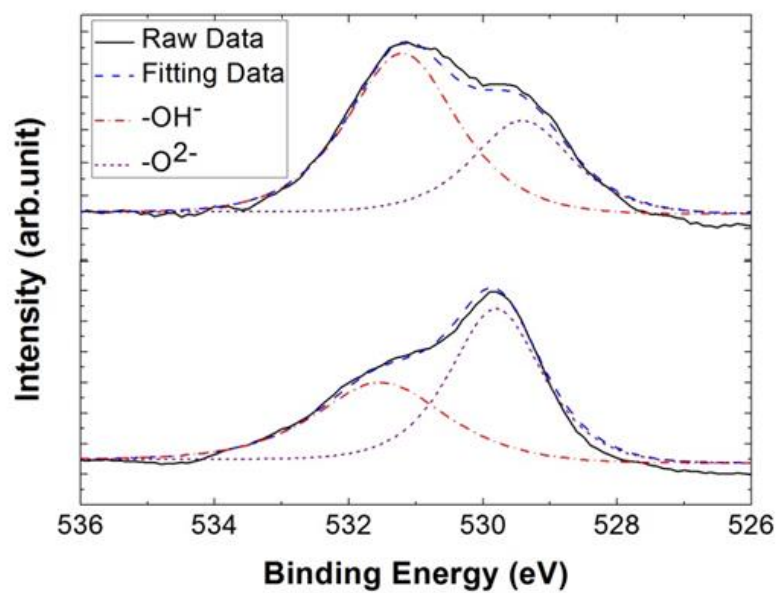


Fig. 2-6 XPS spectra of oxygen in a titanium dioxide thin film fabricated by spray-LBL method before (top) and after annealing at 450°C (bottom).

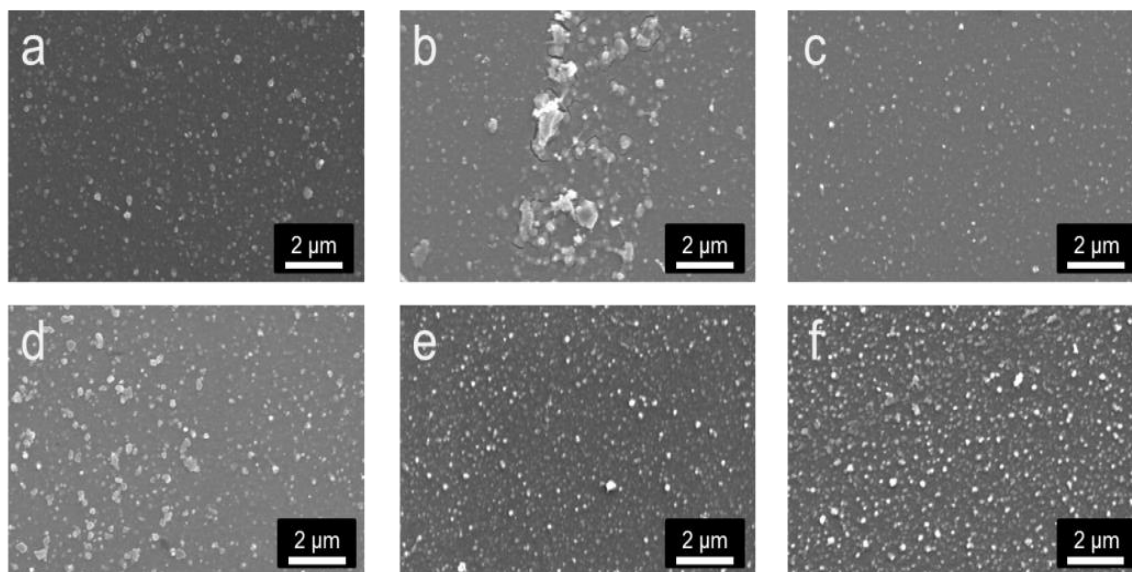


Fig. 2-7 SEM images of TiO₂ layers deposited by spray-LBL on glass before annealing (a) and after annealing at various temperatures: (b) 300°C, (c) 350°C, (d) 400°C, (e) 450°C, and (f) 500°C.

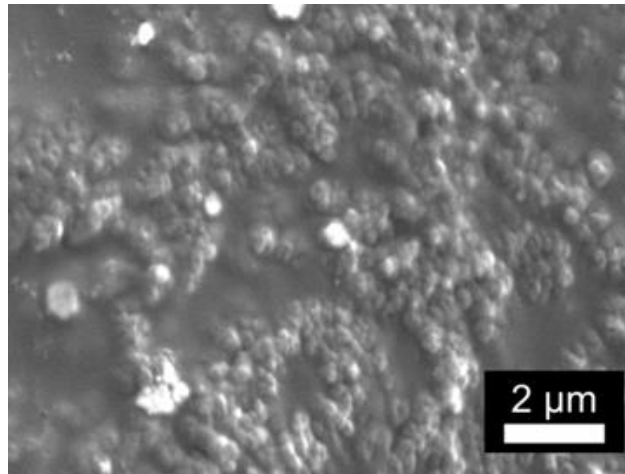


Fig. 2-8 SEM image of TiO₂ layer fabricated by spray-LBL on FTO substrate after annealing at 450°C.

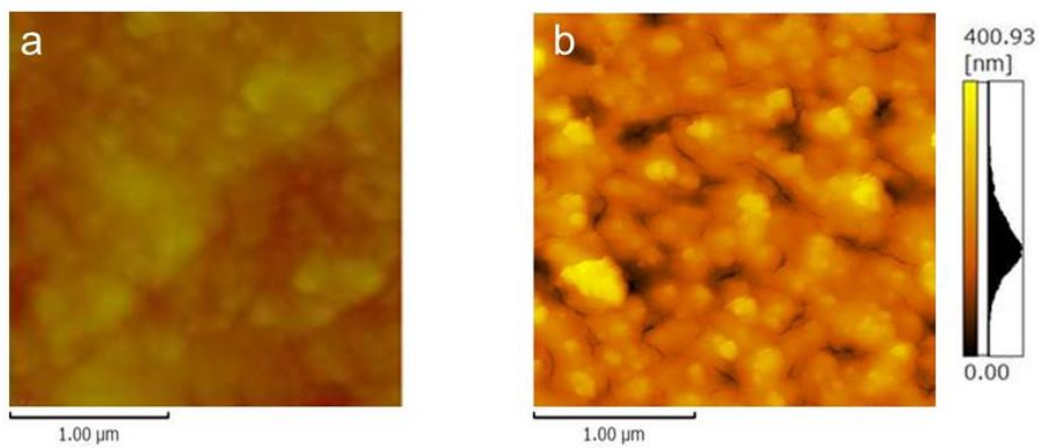


Fig. 2-9 AFM image of (a) FTO layer, Rms of surface=32 nm (b) TiO₂ layer on FTO when fabricated with Spray LBL and annealing at 450 °C, Rms of surface=50 nm

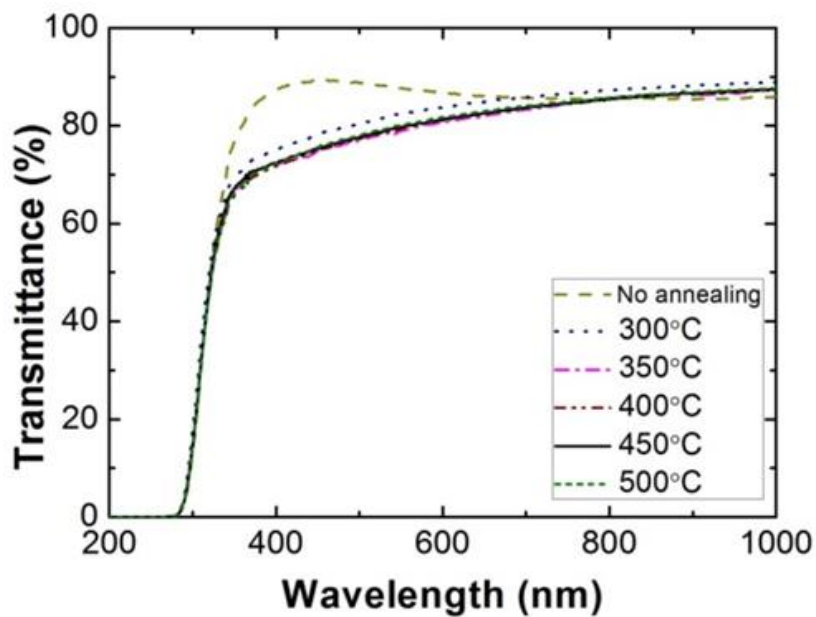


Fig. 2-10 Transmittance of TiO₂ layers fabricated by spray-LBL on glass substrates before and after annealing at various temperatures.

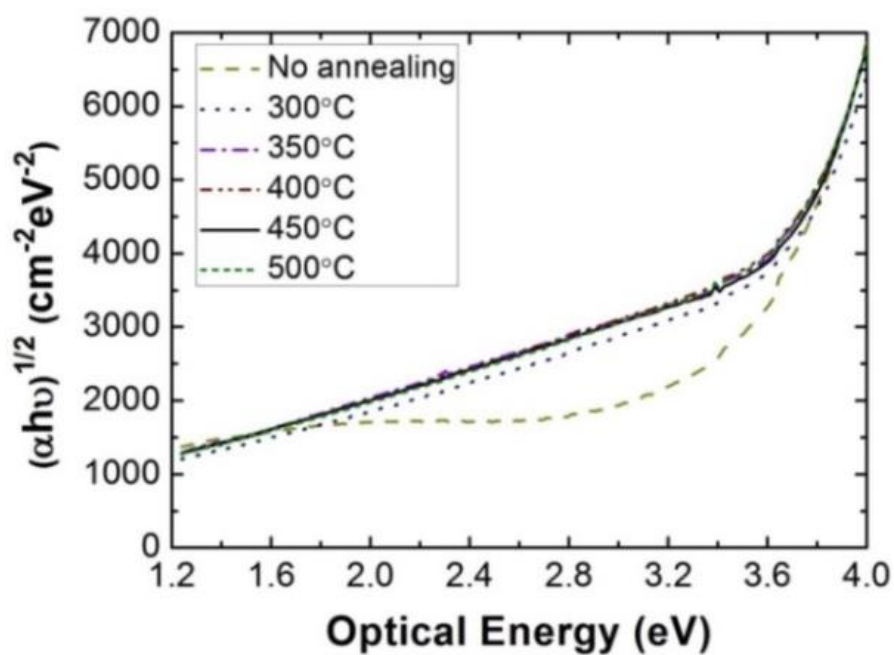


Fig. 2-11 Tauc plot of TiO₂ layers fabricated by spray-LBL method on glass substrates before and after annealing at various temperatures.

Table 2-1 The crystalline size of anatase (004) and rutile (210) after annealing at different temperatures.

Temperature (°C)	Anatase (004) (nm)	Rutile (210) (nm)
As-deposited	28.43	32.14
300	29.00	25.83
350	25.61	23.64
400	25.61	21.69
450	31.96	27.40
500	22.23	24.41

Table 2-2 Haze value and transmittance of FTO, TiO₂/FTO and TiO₂/FTO after annealing at 450 °C

	Transmittance (%)	Haze (%)
FTO	79.81	13.61
TiO ₂ /FTO	81.1	19.31
TiO ₂ /FTO after annealing	79.3	22.1

Table 2-3. The refractive index, haze and energy band gap of TiO₂ fabricated by Spray-LBL and annealing with difference temperature.

Annealing temperature (°C)	Refractive index	Energy band gap (eV)	Haze (%)	Thickness (nm)
No annealing	1.68	3.30	12.3	112
300	1.86	3.28	13.9	109
350	1.90	3.20	15.2	105
400	1.90	3.21	17.5	104
450	1.89	3.21	18.2	103
500	1.89	3.20	18.2	103

Reference

- [2-1] Huang, Z., Maness, P. C., Blake, D. M., Wolfrum, E. J., Smolinski, S. L., & Jacoby, W. A. (2000). *Journal of Photochemistry and photobiology A: Chemistry*, 130(2), 163-170.
- [2-2] Chen, X., Liu, L., Peter, Y. Y., & Mao, S. S. (2011) *Science*, 331(6018), 746-750.
- [2-3] Nishimoto, S., Ota, M., Kameshima, Y., & Miyake, M. (2015). *Colloids and Surfaces A: Physicochemical and Engineering Aspects*, 464, 33-40.
- [2-4] Vasan, R., Makableh, Y. F., & Manasreh, M. O. (2016). *MRS Advances*, 1(14), 957-963.
- [2-5] Umebayashi, T., Yamaki, T., Itoh, H., & Asai, K. (2002). *Applied Physics Letters*, 81(3), 454-456.
- [2-6] Liufu, S., Xiao, H., & Li, Y. (2005). *Journal of colloid and interface science*, 281(1), 155-163.
- [2-7] Krishna, D. S. R., Sun, Y., & Chen, Z. (2011). *Thin Solid Films*, 519(15), 4860-4864.
- [2-8] Busca, G., Saussey, H., Saur, O., Lavalley, J. C., & Lorenzelli, V. (1985). *Applied catalysis*, 14, 245-260.
- [2-9] Mo, S. D., & Ching, W. Y. (1995). *Physical Review B*, 51(19), 13023.
- [2-10] Marchand, R., Brohan, L., & Tournoux, M. (1980). *Materials Research Bulletin*, 15(8), 1129-1133.

- [2-11] Park, N. G., Van de Lagemaat, J., & Frank, A. J. (2000). *The Journal of Physical Chemistry B*, 104(38), 8989-8994.
- [2-12] Kim, H. S., Lee, J. W., Yantara, N., Boix, P. P., Kulkarni, S. A., Mhaisalkar, S., Grätzel, M. & Park, N. G. (2013). *Nano letters*, 13(6), 2412-2417.
- [2-13] Palomares, E., Clifford, J. N., Haque, S. A., Lutz, T., & Durrant, J. R. (2003). *Journal of the American Chemical Society*, 125(2), 475-482.
- [2-14] Choi, H., Nahm, C., Kim, J., Moon, J., Nam, S., Jung, D. R., & Park, B. (2012). *Current Applied Physics*, 12(3), 737-741.
- [2-15] Takenaka, S., Maehara, Y., Imai, H., Yoshikawa, M., & Shiratori, S. (2003). *Thin Solid Films*, 438, 346-351.
- [2-16] Kinsinger, N. M., Wong, A., Li, D., Villalobos, F., & Kisailus, D. (2010). *Crystal Growth & Design*, 10(12), 5254-5261.
- [2-17] Huang, P. C., & Reichert, K. H. (1989). *Die Angewandte Makromolekulare Chemie*, 165(1), 1-7.
- [2-18] Möckel, H., Giersig, M., & Willig, F. (1999). *Journal of Materials Chemistry*, 9(12), 3051-3056.
- [2-19] Guerrero, A., Chambon, S., Hirsch, L., & Garcia-Belmonte, G. (2014). *Advanced Functional Materials*, 24(39), 6234-6240.
- [2-20] Zhang, Y., Yuan, S., & Liu, W. (2014). *Electrochimica Acta*, 143, 18-22.
- [2-21] Baek, W. H., Seo, I., Yoon, T. S., Lee, H. H., Yun, C. M., & Kim, Y. S. (2009). *Solar Energy Materials and Solar Cells*, 93(9), 1587-1591.

[2-22] Reddy, K. M., Manorama, S. V., & Reddy, A. R. (2003). *Materials Chemistry and Physics*, 78(1), 239-245.

Chapter 3

Process Improvement for Organic Thin

Film Solar Cell

3.1 Introduction for organic solar cell

Organic solar cells offer numerous specific advantages as renewable energy sources since the development of semiconducting polymers which has made these cells highly suitable for flexible applications. In term of their properties, organic solar cells are lightweight, have large surface areas and can be colorful.[1-5] While the widespread use of inorganic solar cells remains limited because of the cost of the required fabrication processes, which require elevated temperatures between 400°C and 1400°C, high vacuum processing and several lithographic steps, polymer-based solar cells can be processed more simply from solution.[6-8] This has enabled these devices to resolve the processing challenges and emerge as a low-cost alternative to inorganic solar cells over the past few decades.

Over the past three decays, many research groups have developed many types of organic thin film solar cell and have demonstrated very good PCE result with planar heterojunction organic thin film solar cell[9,10], bulk heterojunction solar cell [11,12], co-evaporated organic small molecular devices[13-15]. Results indicate the performances of organic solar cell achieved PCE around 6-8% and bulk heterojunction /fullerene solar cell can achieve PCE over 11%.[16-17]

In this work, I successfully demonstrated semitransparent polymer-based bulk heterojunction solar cells using these TiO₂ layers to increase the maximum efficiency of the solar cells. Each TiO₂ layer was processed from water-based solutions with a simple

fabrication process, and this process is likely to be applicable to other types of solar cells, e.g., dye-sensitized solar cells (DSSCs)[18,19] or perovskite solar cells.[20] To enhance the maximum efficiency of the solar cells by modifying the TiO₂ layer, an automatic spray layer-by-layer (spray-LBL) self-assembly method that we established in our previous study was used.[21]

3.1.1 Solar Radiation

The solar radiation is related with Planck radiation spectrum from the surface of the sun with source temperature of 5800K. However, the solar radiation on the world surface is distorted a mainly because of the absorption by atmosphere. **Fig. 3-1** shows the solar radiation spectrum for various condition. The air mass X(AMX) is defined by equation [3-1] as;

$$X = \frac{1}{\cos(\theta)} \quad [3-1]$$

Where θ is the angle between the zenith and the position of the sun under terrestrial condition. Air mass 0 is the solar radiation above the earth atmosphere, the standard of AM0 is 135.3 mW/cm². Air mass 1 is when the sun overhead. The AM1.5 is when the sun is at 48.19° from the zenith, the standard of AM1.5 is 100.5 mW/cm².

3.1.2 Basic Parameters of Photovoltaic

The major physical mechanism of solar cell is absorption of photon, which changes to electrical carrier: electron and hole, by generation and recombination process. To understand this mechanism the p-n junction is one of the theories to explain this mechanism. **Fig. 2-2** shows the carrier distribution in p-n junction. From this figure, the

total current density (J) is sum of hole current at x_n position and electron current at $-x_p$ position given by equation;

$$J = A[J_p(x_n) + J_n(-x_p)] \quad [3-2]$$

$$= J_0 \left(e^{\left(\frac{qV}{\gamma k_b T}\right)} - 1 \right) - J_{ph} \quad [3-3]$$

Where J_0 is dark saturation current density, J_{ph} is photo current density, V is applied voltage, q is value of electron charge, γ is ideality factor, K_b is Boltzmann's constant and T is temperature. **Fig.3-3** shows the current-voltage characteristic of solar cell with and without illumination. The open circuit voltage (V_{oc}) of p-n junction is;

$$V_{oc} = \frac{\gamma k_b T}{q} \ln \left(\frac{J_{ph}}{J_0} + 1 \right) \quad [3-4]$$

Short circuit current $J = -J_{sc}$

$$J_{sc} = J_{ph} \quad [3-5]$$

The fill factor(FF) of the current density-voltage characteristic of solar cell is defined by ratio;

$$FF = \frac{V_m J_m}{J_{sc} V_{oc}} \quad [3-6]$$

The PCE of solar cell is defined by[20];

$$PCE = \frac{V_m J_m}{J_{sc} V_{oc}} = \frac{V_m J_m}{P_{opt}} FF \quad [3-7]$$

Where P_{opt} is the incident optical power on the solar cell surface.

To consider deeply about loss in solar cell, the series resistance (R_s) and shunt resistance (R_{sh}) are included in the circuit model. **Fig.3-4** shows the equivalent circuit of one diode model. The solution for one diode is given by equation [22];

$$J = J_{ph} - J_0 \left(e^{\frac{q(V+JR_s)}{\gamma kT}} - 1 \right) - (V + JR_s)/R_{sh} \quad [3-8]$$

3.2 Experiment

3.2.1 Organic Semitransparent Solar Cell

Firstly, the Fluorine-doped tin oxide (FTO) glass (SPD Laboratory, Inc., Hamamatsu, Japan) were cleaned in Acetone and KOH solution (1:120:60 wt% KOH/H₂O/IPA) for 5 min and 10 min, respectively, and then rinsed thoroughly with ultra-pure water before use. In this experiment, we fabricated TiO₂ for organic solar cell by 2 methods. The first method is liquid phase deposition technique (LPD): it was prepared by immersing a fluorine-doped tin oxide (FTO; 7 Ω/cm², 80%, SPD Laboratory) glass slide in an TiF₄ solution (40 mM, pH 2.0) at 60 °C inside a controlled temperature cabinet for 1 hour. After precursor film preparation by liquid phase deposition, the samples were annealed at various temperatures 450 °C for 15 min. The second method is Spray-LBL, the explanation of spray LBL already explain in Chapter 2. The active layers of solar cell were fabricated by Poly(3-hexylthiophene) (P3HT) (Wako Pure Chemical Industries, Ltd., Osaka, Japan) and [6,6]-phenyl C61-butyric acid methylester (PCBM) (Wako Pure Chemical Industries, Ltd., Osaka, Japan) blend solution that prepared at a concentration of 50 mg/mL in monochlorobenzene. The weight ratio between P3HT and PCBM was 1:1. The solution were deposited on TiO₂ layer by spin-coating at 1200 rpm and then annealed at 150°C for 15 min on a hot plate. Simultaneously, D-sorbitol (Wako Pure Chemical Industries, Ltd., Osaka, Japan) mixture in poly(3, 4-

ethylenedioxythiophene):poly(styrenesulfonate) (PEDOT:PSS) (PH500, Clevious, Heraeus, Leverkusen, Germany) solution at a concentration 1 wt% were deposited on the Ag nano-network PET film(Toda Kogyo Corp., Hiroshima, Japan) by spin-coating at 3000 rpm. The finished solar cells were fabricated by pressing the Ag film component and the active layer component together at approximately 0.01 MPa as a simple wet lamination process, and then the devices were annealed at 140°C for 10 min. The active area in this experiment is 0.28 cm².

3.2.2 Flexible Organic Thin Film Solar Cells

Firstly, the Indium-doped tin oxide (ITO) PEN (SPD Laboratory, Inc., Hamamatsu, Japan) were cleaned in Acetone and KOH solution (1:120:60 wt% KOH/H₂O/IPA) for 5 min and 10 min, respectively, and then rinsed thoroughly with ultra-pure water before use. The TiO₂ ETLs were fabricated on the ITO PEN using automatic Spray-LBL. The active layers of solar cell were fabricated by P3HT and PCBM blend solution that prepared at a concentration 50 mg/mL in monochlorobenzene. The weight ratio between P3HT and PCBM was 1:1. The solution were deposited on TiO₂ layer by spin-coating at 1200 rpm and then annealed at 150°C for 15 min on a hot plate. Simultaneously, D-sorbitol mixing in PEDOT:PSS solution at a concentration of 1 wt% were deposited on the Ag PET substrate, the Ag PET substrate fabricated by thermal evaporation Ag on PET substrate, by spin-coated at 3000 rpm. The finished solar cells were fabricated by pressing the Ag film component and the active layer component together at approximately 0.01 MPa as a simple wet lamination process, and then the devices were annealed at 140°C for 10 min.

3.2.3 Characterization

Film thickness and the refractive index of the thin films coated on the substrates were determined by ellipsometry (MARY-102, Five Lab, Japan) and film thickness measurements (Dektak; 3030, ULVAC, Japan). Transmittance in the spectral range of 200 to 1000 nm were measured by a spectrophotometer (UVmini-1240, Shimadzu, Japan). Haze values of the films were measured by a haze meter (NDH-5000, Nippon Denshoku Industries, Tokyo, Japan) with a white light-emitting diode (5 V, 3 W) as an optical source. The current density-voltage (J-V) characteristics of the solar cells were measured using an AM 1.5 solar simulator (100 mW cm^{-2}) and an automatic polarization system (Hokuto Denko HSV-100) with a 500-W Xe lamp (UXL-500SX, Ushio) as a light source. The active areas of these devices are fixed at 0.2827 cm^2 . Series resistance (R_s) and Shunt resistance (R_{sh}) were approximate using one diode model via MATLAB program, the diagram to fitting the J-V characteristic is shown in **Fig. 3-5**.

3.3 Result and Discussion

3.3.1 Band Diagram

Fig. 3-6 shows the band diagram of semitransparent organic thin film solar cell fabricated by spin-coating and lamination process. This band diagram is using the HOMO and LUMO level from previous literature. **Table 3-1** show the HOMO and LUMO level value with literature reports for this value. We choose TiO_2 for ETLs and fabricated by spray layer-by-layer and annealed at $450 \text{ }^\circ\text{C}$ for improve phase, rutile phase, and crystalline quality of TiO_2 layer.[23-24] The P3HT and PCBM were used for active layer, it can be fabricated by mixing P3HT and PCBM in proportion 1:1.[25] On the other side, PEDOT:PSS using for HTLs were coated on Ag-nano network and annealed at $100 \text{ }^\circ\text{C}$

for 15 mins. The PEDOT:PSS were mixed with D-sorbitol for improved performance and using it for blinder for lamination process.[4] Before deposited PEDOT:PSS, the Ag-nano-network PET film were modified the wet contact of it by plasma treatment for 15 mins.[26] Fig. 3-7 show characteristics of the solar cells when fabricated with LPD and spray LBL technique. This result show that the TiO₂ fabricated by spray LBL is suitable for organic solar cell due to the PCE of this result is almost same when compared with fabricated TiO₂ layer with LPD method.

3.3.2 Effect of annealing temperature of TiO₂ layer

The variations in the properties of solar cells with changing annealing temperature are shown in **Table 3-2**. The characteristics of the solar cells depended on the annealing temperature, because the structures and grain sizes of the TiO₂ nanoparticles varied. The maximum efficiency was 1.51% after annealing at 450°C. As shown in the XRD results, when the grain size was large, the grain boundary was reduced according to the peak of the anatase (004) phase after annealing at 450°C, and the rutile (210) phase was formed, which reduced the conductivity and increased the recombination at the interface between TiO₂ and the active layer. The series resistance (R_s) was reduced at annealing temperatures below 450°C, because the TiO₂ phase was changed to the amorphous anatase phase. At annealing temperatures above 450°C, R_s increased, because the TiO₂ rutile phase had higher resistivity than the anatase phase.[27] The shunt resistance (R_{sh}) was higher at annealing temperatures below 450°C, because the crystal quality of the TiO₂ anatase phase was higher. However, at annealing temperatures above 450°C, R_{sh} was reduced, because the anatase phase changed to the rutile phase and the grain size (from XRD and SEM imaging) was reduced because of the increased grain boundaries that make the mobility in the titanium dioxide layer decrease and the efficiency of the

solar cell drop. These results are in good agreement with the results of the experimental report by Roy et al[28]. They fabricated TiO₂ nanorods for DSSCs, and found that the annealing temperature affected both the grain size and the crystalline structure of the TiO₂ nanorods: at annealing temperatures above 500°C, the crystalline phase changed from the anatase to the rutile phase. In addition, they explained that the changes in the grain boundaries and the mobility in the TiO₂ layer also have a major effect in changing the efficiency of solar cell devices.

3.3.3 Effect of thickness TiO₂

Table 3-3 show the optical characteristics of TiO₂ layer depending on the thickness of TiO₂ layer, the optical characteristics were measured by using ellipsometry. The thickness of TiO₂ nanoparticles layers were controlled by changing the number of bilayer of TALH and PDDA. We observed the thickness of TiO₂ layer in case of before annealed are vary from 100-150 nm and the refractive index are varied from 1.64-1.68. However, after annealed at 450 °C the film thickness of TiO₂ decreased and refractive index value increased due to the evaporated of polymer contaminated in mix metal-organic thin film.

Fig. 3-8 and **Table 3-4** showed the J-V characteristic of bulk heterojunction solar cells. In case of 22 bilayers (112 nm), the PCE, V_{oc}, J_{sc} and FF were 2.04%, 0.54 V, 6.73 mA/cm². and 0.56, respectively. The benefit of TiO₂ layer can decrease recombination between generation area and electrode contact, and the leakage current can be also decreased by TiO₂ layer. However, TiO₂ layer has high resistivity when TiO₂ film is thick, and the series resistance (R_s) also increased, which has more negative effect on the efficiency of solar cells. In this case, the series resistance increased from 8.8 Ω (at 20 bilayers) to 27.3 Ω(at 26 bilayers). On the other hand, the recombination effect increased when TiO₂ layer was thin, and the shunt resistance was increased when the number of

bilayer was increased from 20 bilayers (103nm) to 22 bilayers (112nm). In this experiment, 112 nm of the film thickness was the most appropriate for bulk heterojunction solar cells in terms of the efficiency. Ou et al. fabricated TiO₂ layer by CVD.[29] The thickness at the maximum efficiency was thinner than that of our solar cells, because our solar cells consisted of the TiO₂ layer with the lower density and the more porous than CVD technique, derived from the solution process and to form metal-organic compound and the evaporation of the organic compound to transform into the only titanium dioxide layer.

3.3.4 The Optical Transparent of Semi-transparent OSC

The transmittance of solar cells at longer than 700 nm of light wavelength was higher than 60% as shown in **Fig. 3-9**, which showed better results than the previous report,[4] because of increasing the haze value caused by high surface roughness on TiO₂ layer, the haze value shown in **Table 3-5**. With increasing the haze value, the transmittance at near-infrared regions relatively increased due to the diffuse transmittance.[30] **Fig. 3-10** shows the current density–voltage of the semitransparent solar cells by optical incidences in direction from front and back side of the solar cells. The efficiency from the front illumination was higher than that from the backside illumination, because the structure of PEDOT:PSS layer had lower bandgap than PCBM and P3HT, which absorbed the high energy photon and reduced the generation effect at active layer. The transmittance during the front illumination was also lower than that during the backside illumination due to the difference of photo adsorption. The cells during the backside illumination had lower conversion efficiencies than that during the front illumination, which was caused by 60% of the transmittance on the press-Ag NW counter electrode covered with PEDOT/PSS (PE_{press-Ag NW}); in other words, the PE_{press-Ag NW} counter electrode prevented 40%

of the light transmission that should pass into the cells, as proved by the lower photocurrent densities (J_{sc}) of cells from the backside illumination. Although electron was generated by the both sides illumination, the cells during the backside illumination showed lower cell performances.

3.3.5 Flexible Devices

Moreover, we successfully fabricated the bulk heterojunction solar cells without annealing process on ITO PEN substrate. The **Table 3-6** show the properties of solar cell when fabricated the electron transport layer with spray-LBL method without annealed process and **Fig. 3-11** show the Current density –Voltage characteristic of bulk heterojunction solar cells when fabricate the electron transport layer by spray-LBL without annealing. Form this result, we can succeed to fabricated flexible bulk heterojunction solar cells when fabricated TiO_2 layer with 22-26 bilayers and observed the maximum PCE with 0.7 % when fabricated TiO_2 at 24 bilayers.

3.3.6 Improved the PCE of solar cell module.

Based on the related studies using PCBM and P3HT for active layer in bulk heterojunction solar cells, the maximum efficiency of this type was improved by changing the electrode contact to vapor-deposited silver thin film on PET substrate. **Fig. 3-12** shows the Current density–Voltage characteristics and parameters of bulk heterojunction solar cells with the electron transport layer fabricated by Spray-LBL after annealing with silver nano- network and silver thin films on PET substrate for electrode contact. In this case, the conditions of these solar cells with 22 bilayers after annealing $450^\circ C$ were selected (the best condition at **Table 3-4**). The maximum efficiency of this type of solar cells was 2.90%. The efficiency of the cells with silver thin film was higher than that of the cells with the silver nano-network, because the sheet resistivity of the silver thin film (less than

0.5 Ω/cm^2) was lower than silver nano-network (around 10 Ω/cm^2), which decreased the series resistivity of solar cells.

3.4 Conclusions

We successfully fabricated TiO_2 by using spray-LBL using for ETLs in semi-transparent bulk heterojunction solar cells and optimized the annealing temperature and film thickness of it. The current density-voltage characteristics of semi-transparent organic bulk heterojunction solar cell depends on the film thickness of TiO_2 layer and observed the maximum PCE at 2.04% when annealed the TiO_2 thin film at 450 °C and thickness of TiO_2 layer was around 112 nm. Moreover, we also observed the transmittance over 60% at wavelength over 600 nm. We also observed PCE value around 3% when change the structure to general type of organic bulk heterojunction solar cell. This study may contribute to development of semitransparent polymer solar cells through non-toxic process with low-cost, eco-friendly and short fabrication time for larger area devices in the future.

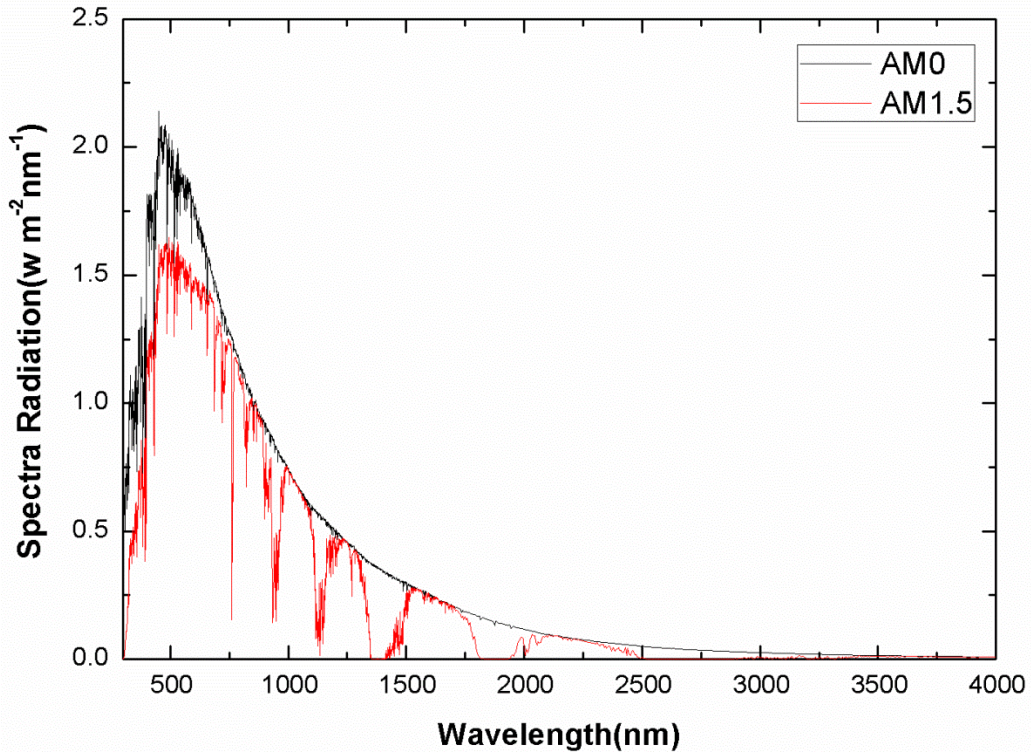


Fig. 3-1 The solar radiation spectrum and wavelength with condition AM0 and AM1.5

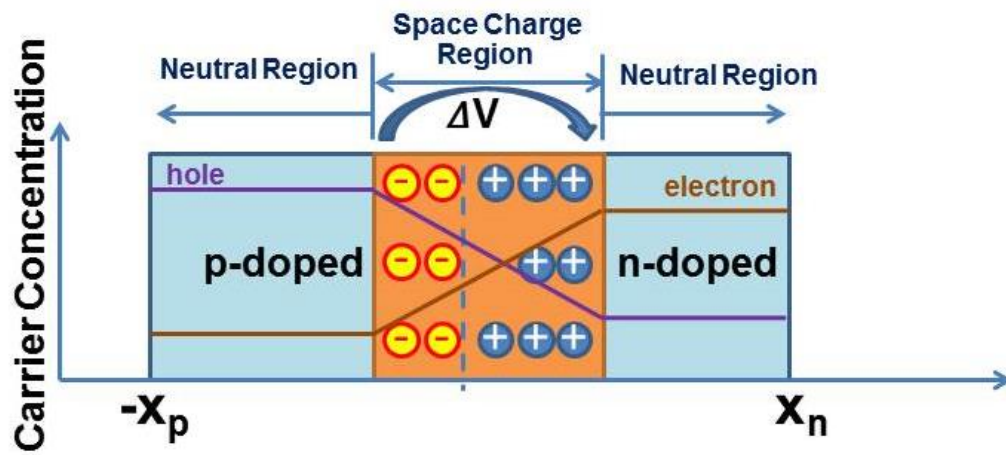


Fig.3-2 A carrier concentration of p-n junction in thermal equilibrium with zero-bias voltage applied.

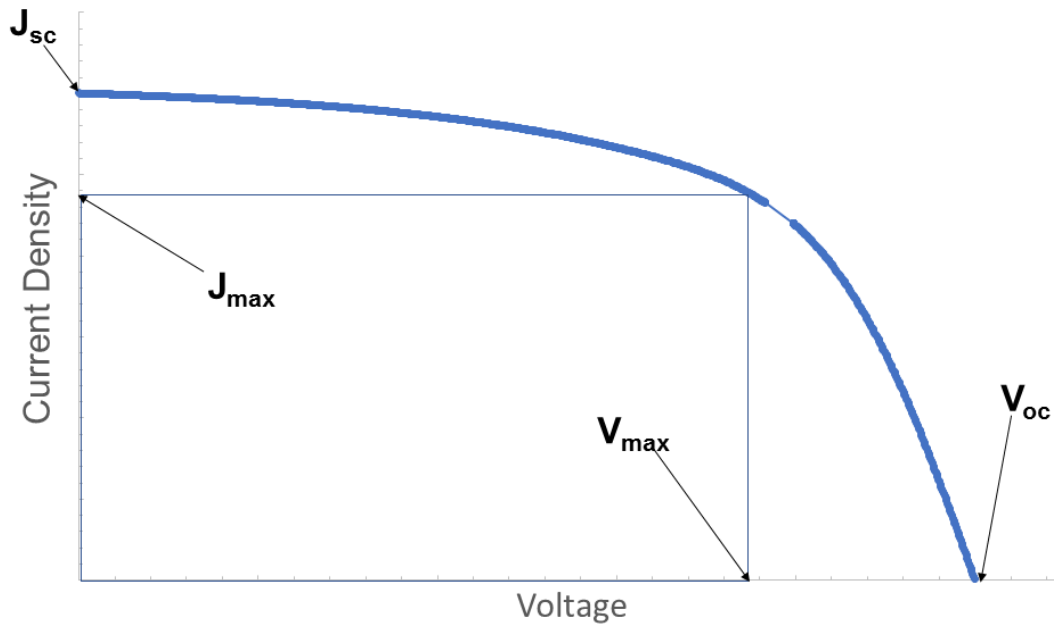


Fig.3-3 Current density -Voltage characteristics of solar cell under illumination.

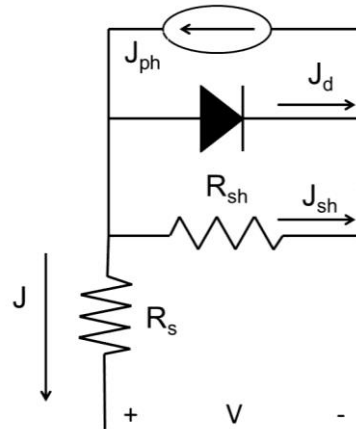


Fig. 3-4 Equivalent circuit of one diode model

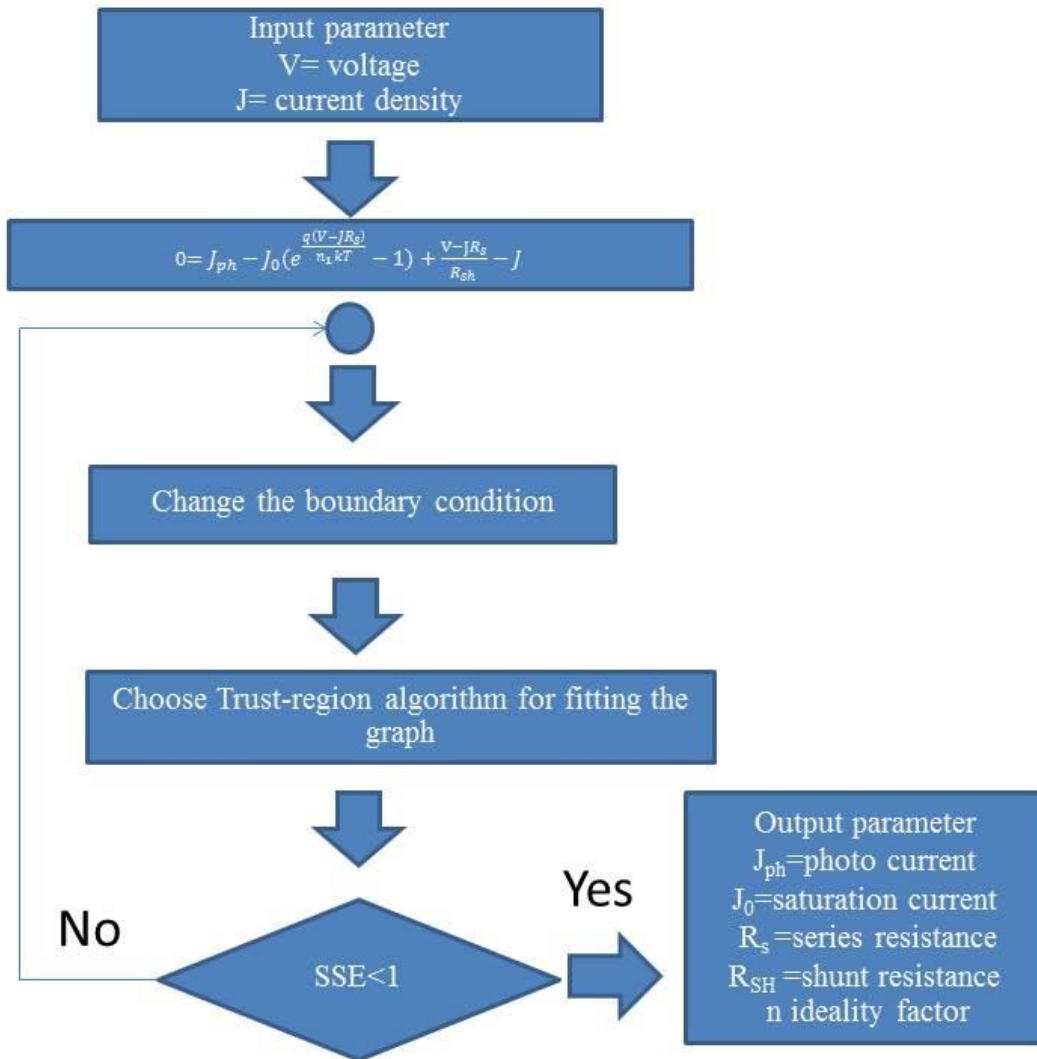
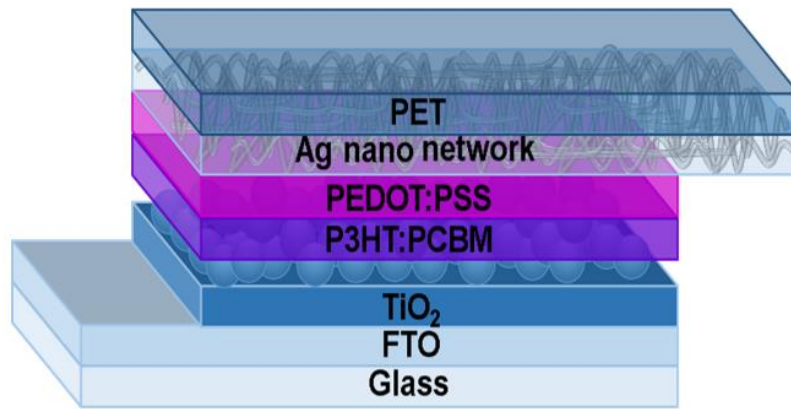
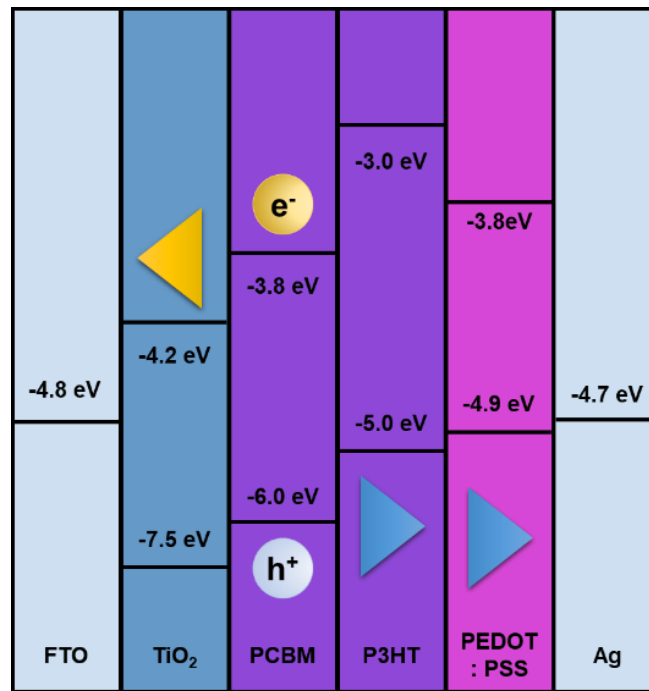


Fig. 3-5 Flow chart for fitting parameter: R_s , R_{sh} , n , J_0 and J_{ph} by using one diode model with Trust-region algorithm.



(a)



(b)

Fig. 3-6 Structure of bulk heterojunction solar cell, and (b) band diagram of bulk heterojunction solar cell in this experiment.

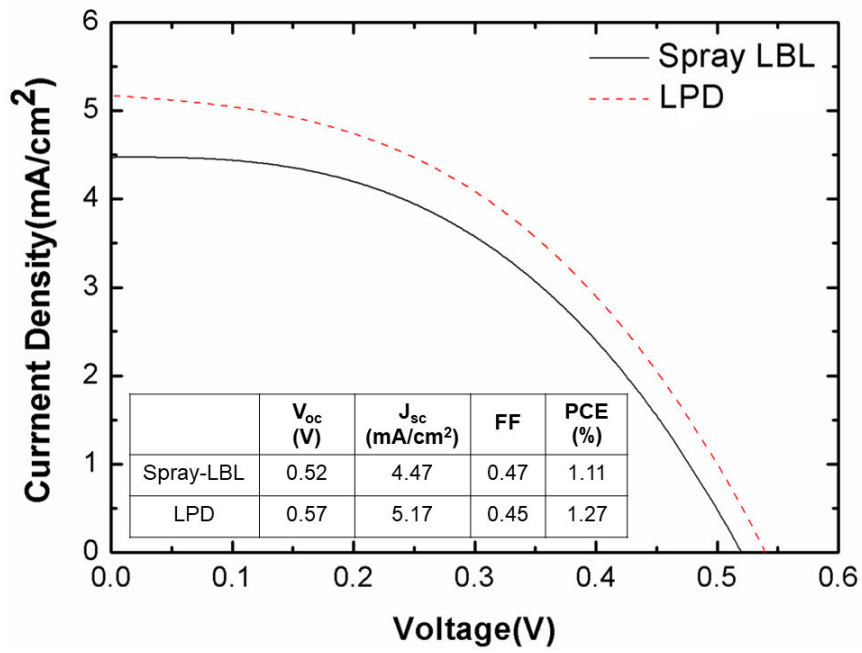


Fig 3-7 Performance of solar cell when fabricated TiO₂ layer with LPD and Spray LBL method

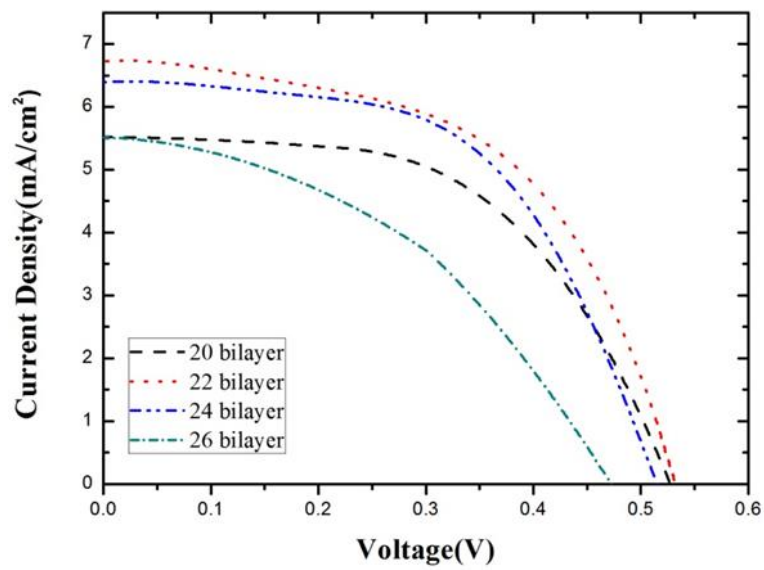


Fig 3-8 Performance of solar cell when changing the thickness of TiO₂ layer when annealing at 450 °C

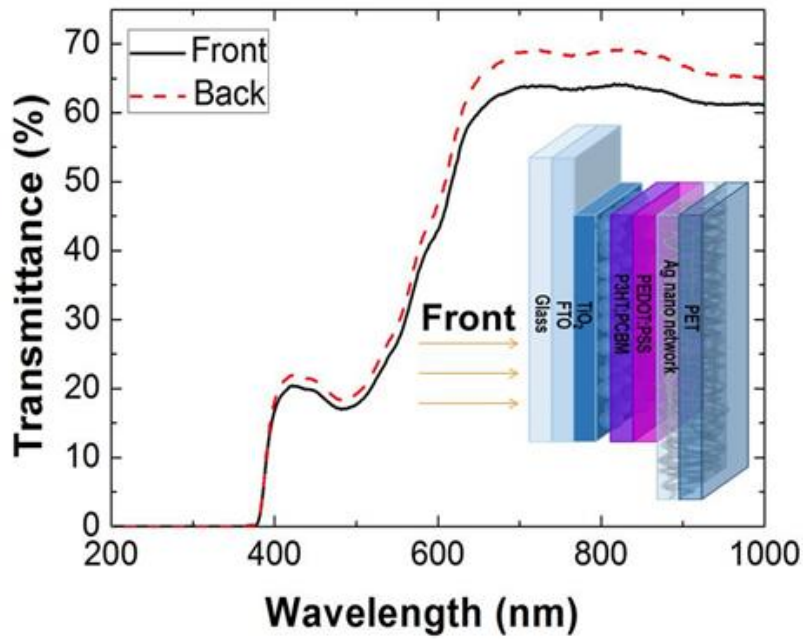


Fig. 3-9 Transmittance of the semitransparent solar cells with the electron transport layer fabricated by Spray-LBL after annealing at 450°C.

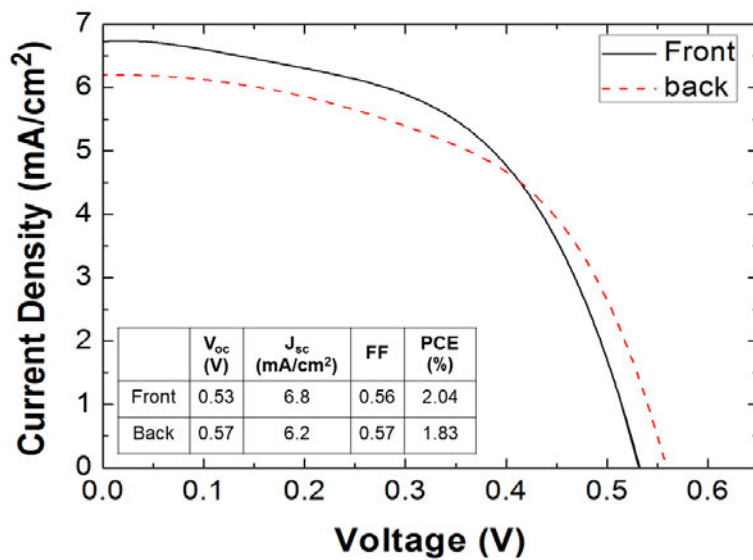


Fig. 3-10 Current density-voltage characteristic of semitransparent solar cell with the electron transport layer fabricated by Spray-LBL after annealing at 450°C

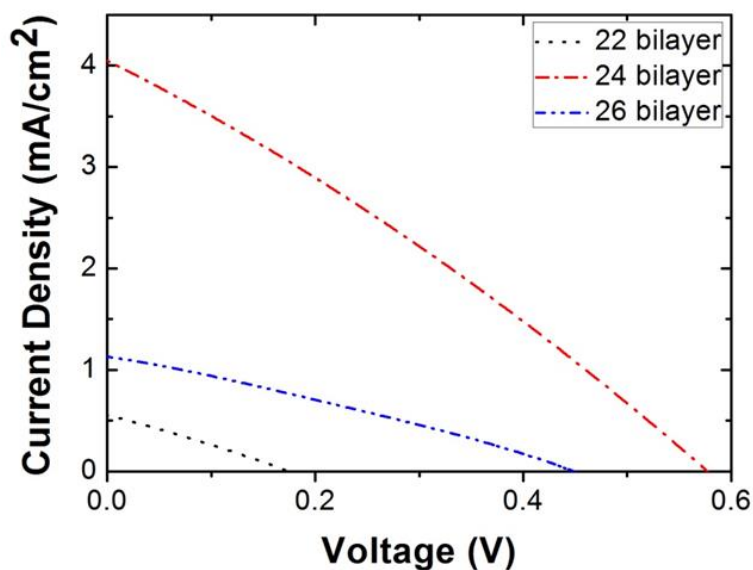


Fig. 3-11 Current density –Voltage characteristic of bulk heterojunction solar cells when fabricate the electron transport layer by spray-LBL without annealing and change the thickness of TiO₂ layer by changing number of bilayers.

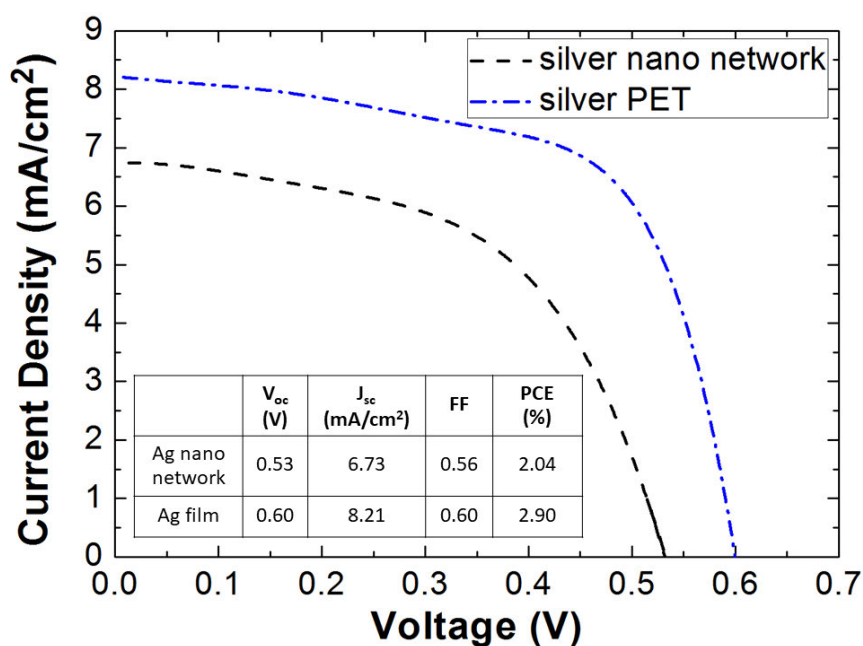


Fig. 3-12 Current density–Voltage characteristics of bulk heterojunction solar cells with the electron transport layer fabricated by Spray-LBL after annealing at 450°C using silver nano- network and silver thin films on PET substrate.

Table 3-1. The value of LUMO and HOMO level of each layer of organic thin film solar cell

Layer	Work Function	HOMO	LUMO	Reference
FTO	-4.8	-	-	[31]
TiO ₂	-	-7.5	-4.2	[32]
PCBM	-	-6.0	-3.8	[33]
P3TH	-	-5.0	-3.0	[33]
PEDOT:PSS	-	-4.9	-3.8	[34]
Ag	-4.7	-	-	[35]

Table 3-2. Electrical properties of solar cells with the electron transport layer fabricated Spray-LBL method before and after annealing at different temperatures.

Annealing temperature (°C)	J _{sc} (mA/cm ²)	V _{oc} (V)	FF	PCE (%)	R _s (Ω)	R _{sh} (kΩ)
300	2.02	0.55	0.297	0.33	59	800
350	4.18	0.51	0.325	0.69	46	1000
400	5.50	0.52	0.479	1.37	19	2000
450	5.25	0.53	0.542	1.51	11	2200
500	5.05	0.54	0.388	1.06	22	270

Table 3-3 The optical properties of electron transport layers fabricated by Spray-LBL method after annealing at 450°C with changing the thickness of TiO₂ layer

Number of bilayer	Thickness (nm)		Refractive index	
	before annealing	after annealing	before annealing	after annealing
20	111	103	1.68	1.89
22	124	112	1.66	1.85
24	136	121	1.62	1.82
26	142	127	1.64	1.82

Table 3-4 Electrical properties of solar cells with electron transport layers fabricated by spray-LBL method after annealing at 450°C for various TiO₂ layer thicknesses.

Number of bilayer	J _{sc} (mA/cm ²)	V _{oc} (V)	FF	PCE (%)	R _s (Ω)	R _{sh} (Ω)
20	5.52	0.53	0.54	1.58	8.8	361
22	6.73	0.54	0.56	2.04	9.8	1213
24	6.40	0.52	0.58	1.82	13.5	939
26	5.51	0.47	0.43	1.11	27.3	758

Table 3-5 Haze value and transmittance of FTO, TiO₂/FTO and TiO₂/FTO after annealing at 450 °C

	Transmittance (%)	Haze (%)
FTO	79.81	13.61
TiO ₂ /FTO	81.1	19.31
TiO ₂ /FTO after annealing	79.3	22.1

Table 3-6 The properties of solar cell when fabricated the electron transport layer with spray-LBL method without annealing and change the number of bilayer

Number of bilayer	Jsc (mA/cm ²)	Voc (V)	FF	PCE (%)	TiO ₂ Thickness (nm)
20	-	-	-	-	100
22	0.55	0.18	0.275	0.027	110
24	4.02	0.58	0.302	0.704	120
26	1.13	0.46	0.295	0.153	130

Reference

- [3-1] Lubber, E. J., & Buriak, J. M. (2013). *ACS nano*, 7(6), 4708-4714.
- [3-2] Zhou, Y., Zhang, F., Tvingstedt, K., Barrau, S., Li, F., Tian, W., & Inganäs, O. (2008)., *Applied Physics Letters*, 92(23), 233308.
- [3-3] Krantz, J., Stubhan, T., Richter, M., Spallek, S., Litzov, I., Matt, G. J., Spiecker, E. & Brabec, C. J. (2013), *Advanced Functional Materials*, 23(13), 1711-1717.
- [3-4] Shimada, C., & Shiratori, S. (2013), *ACS Applied Materials & Interfaces*, 5(21), 11087-11092.
- [3-5] AbdulAlmohsin, S., & Cui, J. B. (2012), *The Journal of Physical Chemistry C*, 116(17), 9433-9438.
- [3-6] Lim, Y. F., Lee, S., Herman, D. J., Lloyd, M. T., Anthony, J. E., & Malliaras, G. G. (2008). *Applied Physics Letters*, 93(19), 193301.
- [3-7] Peh, R. J., Lu, Y., Zhao, F., Lee, C. L. K., & Kwan, W. L. (2011), *Solar Energy Materials and Solar Cells*, 95(12), 3579-3584.
- [3-8] Kang, J. W., Kang, Y. J., Jung, S., You, D. S., Song, M., Kim, C. S., Kim, D.G., Kim, J.K. & Kim, S. H. (2012). *Organic Electronics*, 13(12), 2940-2944.
- [3-9] Xue, J., Uchida, S., Rand, B. P., & Forrest, S. R. (2004). *Applied Physics Letters*, 84, 3013.
- [3-10] Peumans, P., Bulović, V., & Forrest, S. R. (2000), *Applied Physics Letters*, 76(19), 2650-2652.

- [3-11] Scharber, M. C., Mühlbacher, D., Koppe, M., Denk, P., Waldauf, C., Heeger, A. J., & Brabec, C. J. (2006), *Advanced materials*, 18(6), 789-794.
- [3-12] Park, S. H., Roy, A., Beaupre, S., Cho, S., Coates, N., Moon, J. S., Moses, D., Leclerc, M., Lee, K. & Heeger, A. J. (2009), *Nature photonics*, 3(5), 297-302.
- [3-13] Gebeyehu, D., Maennig, B., Drechsel, J., Leo, K., & Pfeiffer, M. (2003). *Solar Energy Materials and Solar Cells*, 79(1), 81-92.
- [3-14] Chen, G., Sasabe, H., Wang, Z., Wang, X. F., Hong, Z., Yang, Y., & Kido, J. (2012). *Advanced Materials*, 24(20), 2768-2773.
- [3-15] Opitz, A., Ecker, B., Wagner, J., Hinderhofer, A., Schreiber, F., Manara, J., Pflaum, J. & Brütting, W. (2009), *Organic Electronics*, 10(7), 1259-1267.
- [3-16] Dennler, G., Scharber, M. C., & Brabec, C. J. (2009). *Advanced Materials*, 21(13), 1323-1338.
- [3-17] Blom, P. W., Mihailetchi, V. D., Koster, L. J. A., & Markov, D. E. (2007), *Advanced Materials*, 19(12), 1551-1566.
- [3-18] Tang, Y. B., Lee, C. S., Xu, J., Liu, Z. T., Chen, Z. H., He, Z., Cao, Y. L. Yuan, G., Song, H., Chen, L., Luo, L., Cheng, H.M., Zhang, W.J., Bello, I. & Luo, L. (2010). *Acs Nano*, 4(6), 3482-3488.
- [3-19] Hara, K., Dan-oh, Y., Kasada, C., Ohga, Y., Shinpo, A., Suga, S., Sayama, K. & Arakawa, H. (2004), *Langmuir*, 20(10), 4205-4210.
- [3-20] Conings, B., Baeten, L., Jacobs, T., Dera, R., D'Haen, J., Manca, J., & Boyen, H. G. (2014). *APL Materials*, 2(8), 081505.

- [3-21] Fukao, N., Kyung, K. H., Fujimoto, K., & Shiratori, S. (2011). *Macromolecules*, 44(8), 2964-2969.
- [3-22] Chan, D. S., & Phang, J. C. (1987). ANALYTICAL METHODS FOR THE EXTRACTION OF SOLAR-CELL SINGLE-AND DOUBLE-DIODE MODEL PARAMETERS FROM IV CHARACTERISTICS.
- [3-23] Thamaphat, K., Limsuwan, P., & Ngotawornchai, B. (2008). *Kasetsart J.(Nat. Sci.)*, 42(5), 357-361.
- [3-24] Tang, H., Prasad, K., Sanjines, R., Schmid, P. E., & Levy, F. (1994). *Journal of applied physics*, 75(4), 2042-2047.
- [3-25] Huang, J., Li, G., & Yang, Y. (2005). *Applied Physics Letters*, 87(11), 112105.
- [3-26] Lai, J., Sunderland, B., Xue, J., Yan, S., Zhao, W., Folkard, M., Michael, B.D. & Wang, Y. (2006), *Applied Surface Science*, 252(10), 3375-3379.
- [3-27] Busca, G., Saussey, H., Saur, O., Lavalley, J. C., & Lorenzelli, V. (1985). *Applied catalysis*, 14, 245-260.
- [3-28] Roy, P., Kim, D., Lee, K., Spiecker, E., & Schmuki, P. (2010). *Nanoscale*, 2(1), 45-59.
- [3-29] Ou, K.L., Tadytin, D., Steirer, K.X., Placencia, P., Nguyen, M., Lee, P. and Armstrong, N.R., *J. Mater. Chem. A*, 2013, 1, 6794–6803
- [3-30] Chang, K. M., Ho, P. C., Ariyarit, A., Yang, K. H., Hsu, J. M., Wu, C. J., & Chang, C. C., *Thin Solid Films*, 2013, 548, 460-464.

- [3-31] Wang, J. Y., Hsu, F. C., Huang, J. Y., Wang, L., & Chen, Y. F., ACS applied materials & interfaces, 2015, 7(50), 27676-27684.
- [3-32] Chung, I., Lee, B., He, J., Chang, R. P., & Kanatzidis, M. G, Nature, 2012, 485(7399), 486.
- [3-33] Manna, E., Xiao, T., Shinar, J., & Shinar, R., Electronics, 2015, 4(3), 688-722.
- [3-34] Chen, C. C., Bae, S. H., Chang, W. H., Hong, Z., Li, G., Chen, Q., Zhou, H. & Yang, Y., Materials Horizons, 2015, 2(2), 203-211.
- [3-35] Yang, T., Wang, M., Duan, C., Hu, X., Huang, L., Peng, J., Huang, F. & Gong, X., Energy & Environmental Science, 2012, 5(8), 8208-8214.

Chapter 4

Optimization Technique with Low Temperature Process for Perovskite Solar Cell

4.1 Introduction

Lead halide perovskite solar cells (PVSCs) have been much studied by using various materials and have possibility to be fabricated onto flexible substrate with easy process.[1-3] Those perovskite materials exhibit excellent photonic properties such as high absorption coefficient, long carrier life time, and low recombination rate with a tunable bandgap.[4-5] PVSCs already achieved the maximum efficiency over 22% in short period of time.[6] The efficiency of perovskite has been improved and developed with variety of fabrication techniques, device structure and optimization of parameters.[7-8]

Developing photovoltaics for wearable devices requires low temperature process because flexible plastic substrates have low thermal durability.[9] In addition, it requires special materials for the process to fabricate wearable PVSC. To improve this problem, we choose tin oxide layer for ETLs. This material already improves PVSCs by report of Ke et. al.[10] The property of SnO₂ is suitable for PVSCs because of this material have higher electron mobility than that of TiO₂.

However, to finding the “optimum condition” through such a variety of systems in fabricating PVSCs might make the process complicated. The features that make achieving high-performance PVSCs difficult are; multi-layered structure and composite material used for fabrication[11]; difficulty of controlling the uniformity, grain size and crystalline

quality of perovskite layer that have, both individually and interactively, high effect to the output efficiency.[12] Due to this wide range of manufacturing problems, the optimization process of PVSCs requires vast numbers of experimental trials that could slow down the research of PVSCs.

In many industries, the design of experiment (DoE) is chosen for decreasing the number of experiments that has benefited for reducing the cost and time for optimizing the process condition.[13,14] In previous reports, Chen et al. used a combination of DoE and the response surface models for the optimized manufacturing conditions of dairy tofu.[15] Bashiri et al. also used DoE and the response surface models for optimizing the parameters and studied optical properties of Cu and Ni-doped TiO₂ in photocatalysts.[16]

In this chapter, we report the low-temperature fabrication of PVSCs process with using Latin hypercube sampling (LHS)[17,18] for DoE, where we randomly chose only 12 conditions for two factors with 12 levels each. DoE by LHS drastically decreases the number of experiment with keeping the uniformity through the experimental space. After making the experiment, we investigated the reasonability of result efficiency via material characterizations such as morphology and crystalline property. Then we utilized Kriging model to model the output efficiency and to find the optimal condition.[19,20] The optimization process was verified using the computational optimization through the genetic algorithm.[21-23] Our method is one of the technique for simulating the system model based on experimental data, which has benefit to predict the optimum point independent of any theoretical model like coarsening effects of crystals or ionic motion inherent to perovskite materials.[24,25]

4.2 Method

To design the experiment, we utilized LHS method. [17,28] The LHS method is one of the techniques for random value sampling that has large diversity. After DoE process, an Ordinary Kriging interpolation method[19,20] was used to predict their output function from the data generated through DoE. The outputs of this experiment are fill factor (FF), short circuit current density (J_{sc}), open circuit voltage (V_{oc}) and power conversion efficiency (PCE).

Next, the genetic algorithm with Nondominated sorting genetic algorithm-II (NSGA-II)[26,27] was used to investigate the best condition by finding the maximum values of FF, J_{sc} and V_{oc} . In this process, the number of population was 50 and number of generation was 500. The algorithm of our optimization process is shown in **Fig. 4-1**

4.2.1 Kriging Model Method

Kriging model[19,20] is an expression of unknown function y as;

$$\hat{y}(x) = \mu(x) + \epsilon(x) \quad [4-1]$$

where $\mu(x)$ is a global model and $\epsilon(x)$ is a local model. Sample points (x) are interpolated with Gaussian random function. The correlation between $Z(x_i)$ and $Z(x_j)$ is related to the distance between the two corresponding points x_i and x_j . The distance function between the point and is expressed as;

$$d(x_i, x_j) = \sum_{k=1}^m \theta^k |x_i^k - x_j^k|^2 \quad [4-2]$$

where $\theta^k (0 \leq \theta^k \leq \infty)$ is the k^{th} element of the correlation vector parameter θ . The correlation between the points x_i and x_j is defined as;

$$\text{Corr}[Z(x_i), Z(x_j)] = \exp(-d(x_i, x_j)) \quad [4-3]$$

Then the Kriging prediction can be expressed as;

$$\hat{y}(x) = \hat{\mu}(x) + \mathbf{r}^T \mathbf{R}^{-1}(\mathbf{F} - \hat{\boldsymbol{\mu}}) \quad [4-4]$$

where $\mathbf{F} = [f(x_1), f(x_2), f(x_3), \dots, f(x_N)]$ is the value of the evaluated function value at $\mathbf{X}_n = \{x_1, x_2, x_3, \dots, x_n\}$, \mathbf{R} denotes the $n \times n$ matrix whose (i,j) entry is $\text{Corr}[Z(x_i), Z(x_j)]$, \mathbf{r} is the vector whose i^{th} element is;

$$r_i(x) = \text{Corr}[Z(x), Z(x^i)] \quad [4-5]$$

The unknown parameter, θ for the Kriging model can be estimated by finding the maximum likelihood estimation:

$$\text{Ln}(\mu, \sigma^2, \theta) = -\frac{n}{2} \ln(\sigma^2) - \frac{1}{2} \ln(|\mathbf{R}|) \quad [4-6]$$

MLE is an m -dimensional unconstrained non-linear optimization problem. In this paper, a genetic algorithm (NSGA-II) is used to solve this problem. For a given θ , σ^2 can be defined as;

$$\sigma^2 = \frac{(\mathbf{F} - \hat{\boldsymbol{\mu}}(x))' \mathbf{R}^{-1} (\mathbf{F} - \hat{\boldsymbol{\mu}})}{n} \quad [4-7]$$

Then, $\mu(x)$ is assumed to be a constant value in the original Kriging as;

$$\mu(x) = \frac{\mathbf{1}' \mathbf{R}^{-1} \mathbf{F}}{\mathbf{1}' \mathbf{R}^{-1} \mathbf{1}} \quad [4-8]$$

4.2.2 NSGA-II

Genetic Algorithm (GA)[21-23] is a stochastic search method using the genetic operators, e.g., the selection, crossover and mutation. **Fig. 4-2** shows the algorithms of simple GA. In this work, the Non-dominated Sorting Genetic Algorithm-II (NSGA-II)[26,27] was selected to search the minimum mass and stress of structure.

NSGA-II is widely employed to solve the multi-objective optimization problem. NSGA-II is characterized by non-dominated points and crowding distance sorting. The individuals of the next generation are selected by elitism. The new generation is sequentially filled by each front until the population size exceeds the current population size, shown in **Fig. 4-3**. In this work, the blended crossover-0.5 (BLX-0.5) and the simple mutation were also applied.

4.3 Experiment

4.3.1 Synthesis of Methyl Ammonium Iodide (MAI)[28]

In this experiment, we synthesized MAI powder by mixing 5.8 mL of HI (57 wt% in water, Sigma-Aldrich), 5 mL of Methylamine (40 wt% in methanol, Tokyo Chemical Industry Co. Ltd) and 20 mL of ethanol in a round bottom flask and stirred at 0 °C (ice bath) for 2 hours. After that, MAI was crystallized by rotary evaporation of the solvent at 50 °C for one hour. MAI powder was washed three times with diethyl ether (99%, Wako) in ultrasonic bath, and dried in vacuum oven at 50 °C for 8 hours.

4.3.2 Devices Fabrication

In this experiment, we fabricated the perovskite solar cell in air-glovebox at humidity under 15% without N₂ or Ar flow. F-doped tin oxide (FTO) glass (TEC7, Pilkington) was patterned with 4M of HCl and Zinc powder. After etching, substrates were cleaned by sonication with isopropyl alcohol (IPA) and deionized water (DIW) for 5 and 10 min, respectively. Then the substrates were heated at 60°C for 30 mins to remove the remnant solvent. The SnO₂ electron transport layer was deposited via spin coating 0.1M solution of SnCl₂ (98%, Sigma-Aldrich) in ethanol at 3000 rpm for 30 s. The samples were annealed at 180°C for 1 hour in laboratory oven to surely convert SnCl₂ into SnO₂. To

prepare the perovskite layer with two-step method, 1M of PbI_2 dissolved in mixed solvent that contains dimethylformamide (DMF, 99%, Wako) and dimethyl sulfoxide (DMSO 99%, Wako). The volume ratio of solvent was 9:1. The samples and precursor solution were preheated at 70°C before deposition. The precursor solution was coated on the substrate by spin-coating typically at 500 rpm for 3 s and high spin speed, high spin speed change by each condition, for 30 s. The PbI_2 films were annealed at 70°C for 15 min to remove the remnant solvent in the film. After the surface temperature of PbI_2 thin films were decreased to room temperature, the samples were dipped in MAI solution (10 mg mL^{-1} in IPA) typically for 10 min followed by rinsing with IPA and annealing at 90°C for 20 min. To fabricate the hole transport layer, the samples were spin coated at 2000 rpm with HTLs solution. The HTLs solution was prepared by mixing 68 mM spiro-OMeTAD (Sigma-Aldrich), 26 mM Li-TFSI (Sigma-Aldrich), and 55 mM 4-tert-butylpyridine (TBP, Sigma-Aldrich) in acetonitrile and chlorobenzene (V/V=1:10). Finally, 100 nm of gold electrodes were deposited by magnetron sputtering process. The active device area was 0.09 cm^2 . The band diagram and devices structure are shown in **Fig. 4-4**. This band diagram are using the HOMO and LUMO level from previous literature.[29]

4.3.3 Characterization

Surface topographies of perovskite layer were observed by field emission scanning electron microscope (FE-SEM, S-4700, Hitachi, Japan) with an accelerating voltage of 5 kV. The thickness of each layer was measured by stylus profilometry (Dektak 3030, ULVAC, Japan). Light transmittance over the range of 200 to 1000 nm was measured using spectrophotometry (UVmini-1240, Shimadzu, Japan). Crystallization of the perovskite layer was analyzed by X-ray diffraction (XRD, D8 DISCOVER, Bruker, USA) using $\text{Cu K}\alpha$ radiation (40 kV, 40 mA), with a scan rate and a step size of $2^\circ/\text{min}$ and

0.01 °/min, respectively. The surface elemental composition of the samples was identified by XPS (JEOL JPS-9000MX). The current density-voltage (J-V) characteristics of the solar cells were measured using an AM 1.5 solar simulator (100 mWcm⁻²) and an automatic polarization system (Hokuto Denko HSV-100) that used a 500 W Xe lamp (UXL-500SX, Ushio) as a light source.

4.4 Result and Discussion

4.4.1 Design of experiment

To design the experiment, we focused on two parameters as dominant parameters. The first parameter is the thickness of perovskite layer, which can be controlled by spin-speed for depositing PbI₂ layer. The second parameter is dipping time of PbI₂ thin film in MAI solution. Other possible parameters in the perovskite layer are as follows; duration time of spin coating, annealing temperature, and environmental humidity. The set of conditions was selected following the LHS as **Table 4-1**. The optimization problem can be written as follows;

$$\text{Maximize: } f_1 = FF$$

$$\text{Maximize: } f_2 = J_{sc}$$

$$\text{Maximize: } f_3 = V_{oc}$$

$$\text{Subject to: } 2000 \leq \text{Spin speed} \leq 5000$$

$$300 \text{ s} \leq \text{Dipping time} \leq 780 \text{ s}$$

4.4.2 Control film thickness of perovskite layer

One of the important parameters to control the efficiency of solar cell is the film thickness of perovskite layers. **Fig. 4-5** shows the relation between film thickness of perovskite

layer fabricated on SnO₂ layer and spin speed. We used conditions determined by LHS model (**Table 4-1**) for this measurement. One can easily see the spin speed is uniformly distributed through the whole range, which is one of the benefits of DoE based on LHS. The film thickness was decreased from 630 nm at 2314 rpm to 125 nm at 4794 rpm. From this graph, we can obtain the relationship between thickness and spin-speed by;

$$L = 3.05 * 10^9 / x^2 \quad [4-9]$$

Where L is perovskite film thickness and x is spin speed.

4.4.3 Photovoltaic characteristics

Table 4-2 shows the output parameters of PVSCs fabricated using the conditions in **Table 4-1**. From **Table 4-2**, we plotted the relationship between J_{sc} and V_{oc} in **Fig. 2**. From the original current density-voltage graph, we calculated fill factor (FF). J_{sc} and V_{oc}. The conventional efficiency of solar cell can be calculated by the equation as follows;

$$PCE = J_{sc} \times V_{oc} \times FF \quad [4-10]$$

This means that in this experiment, we optimized the efficiency by optimizing the output composed of three sub-outputs: J_{sc}, V_{oc}, and FF.

From data from **Table 4-2**, the range of J_{sc} was from 0.1 to 15.7 mAcm⁻², V_{oc} from 0.19 to 1.03 V and FF from 0.28 to 0.49. According to low range of FF variance when compared with those of J_{sc} and V_{oc}, the FF was ignored for optimization here. **Fig. 4-6** shows the relationship between output parameter J_{sc} and V_{oc}. We observed a general population of J_{sc} depends on V_{oc}, having only some data have a trading off relationship: the data in the red cycle is trading off data which have high V_{oc} with low J_{sc} value.

Fig. 4-7 shows the relationship between input parameters and efficiency from original experimental data. We observed the large difference in efficiency when we change the spin-speed and dipping time, so these input parameters are effective for finding the optimum point of the experiment. To explain the high range of efficiency difference, we have characterized the surface morphology and crystalline quality of perovskite layer, which is explained in the next part.

4.4.4 Surface Morphology and Crystalline Property

The surface morphology of perovskite layer fabricated under conditions in **Table 4-1** is shown in **Fig. 4-8**. This figure shows the difference of roughness and grain size of perovskite with PbI_2 spin-speed and MAI dipping time. We observed the high roughness of perovskite in the case of low spin speed and smooth surface in case of high-spin rate coating of PbI_2 . For improving the efficiency of solar cell, the low roughness of perovskite and large grain size are required.[30]

Fig. 4-9(a) shows the relationship between average grain size of surface perovskite thin film fabricated by spin coating and input parameter. This graph was plotted by using analysis data of grain size average from SEM images, which is shown in **Fig. 4-10**. We found the grain size of thin film is larger when fabricated at low spin speed. This large grain size occurs from high film thickness. Usually, large grain size has benefit to increase the efficiency, [31] however in this report we could not observe the high efficiency at low spin speed, which can be explained by poor homogeneity of grain size distribution.[32]

Fig. 4-9(b) shows the standard deviation of the grain size of surface perovskite film and input parameters. We observed the high S.D. value when we fabricated perovskite thin film at low spin speed. This can explain the poor uniformity of grains and high roughness

of the thin film. Some previous reports concluded the familiar tendency that the high roughness of thin film makes the efficiency of solar cell drop.[33,34]

To investigate the crystalline property of perovskite layer for each condition, we measured the XRD spectra. The XRD results are shown in **Fig. 4-11**. In previous reports, the ratio of PbI₂ and perovskite peak strength can explain the crystalline quality of perovskite thin film. Hsieh et al. defined the conversion ratio of PbI₂ into methylammonium lead iodide (MAPbI₃) with following equation[35];

$$C_{MAPbI_3} = \frac{I_{14.2}}{I_{12.7} + I_{14.2}} \quad [4-11]$$

Where I_{12.7} is the intensity of PbI₂ peak at 12.7° and I_{14.2} is the intensity MAPbI₃ peak at 14.2° The values of conversion ratio are shown in Table 4-3. For fabricating the high-efficiency solar cell we need high conversion ratio into MAPbI₃. We found the high amount of PbI₂ remained in conditions of low spin-speed rate and short dipping time. The highest conversion ratio of MAPbI₃ was found in condition 1, which should lead to highest efficiency from the experiment.

Fig. 4-9(c) shows the relationship between each experimental input parameters (spin-speed and dipping time) and C_{MAPbI_2} . We observed the low C_{MAPbI_2} in case of low spin rate, which shows incomplete crystalline conversion due to thick PbI₂ film or low contact time to MAI solution.

4.4.5 Predicting the mapping surface via Kriging Model

For using Kriging model, we used output parameters from **Table 4-2**. The results of computational optimization by the Kriging model are shown in **Fig. 4-12**. This figure shows the simulation of output surface distribution J_{sc}, V_{oc} and power conversion

efficiency (PCE). From these surface plots, we can approximate the reasonable region of input parameters for reaching the high value of output.

From **Fig. 4-12(a)**, we approximated the region for getting high J_{sc} output, J_{sc} higher than 12 mAcm^{-2} , as 3400-3600, 4600-4800 rpm for spin speed and 600-740s for dipping time. For V_{oc} , higher than 0.9 V, the region was approximated as 2200-3800 rpm and 600-720 s (**Fig. 4-12(b)**). And for power conversion efficiency, we define the local maximum area 1 as a red color cycle, area 2 as a black color cycle and area 3 as a brown color cycle (**Fig. 4-12(c)**).

4.4.6 Validation of the Optimization via Genetic Algorithm (NSGA-II)

To check our best fabrication condition, we used NSGA-II, which predicts the best condition in a different manner. **Fig. 4-13** shows the non-dominated solution of output parameters; V_{oc} and J_{sc} ; this graph is obtained by NSGA-II simulation from random best region data along J_{sc} and V_{oc} in **Fig. 4-12 (a), (b)**. From this graph, the predicted highest J_{sc} from this system is around 15.8 mAcm^{-2} and V_{oc} around 1.03V. The region for high efficiency of solar cell is obtained as J_{sc} around 14.8 mAcm^{-2} to 15.8 mAcm^{-2} and V_{oc} from 0.8 to 1.05 V.

To understand the two group of data, the data from area 1 and 2 from **Fig. 4-12(c)**, we analyzed the SEM image, XRD data and used Kriging modeling for simulating the surface of conversion of MAPbI_3 and S.D value: we already explained in the S.D value are related to homogeneous of perovskite thin film in SEM characterization part. **Fig. 4-14(a)** shows the Kriging surface of S.D value of perovskite grains, on which lower value shows higher uniformity. **Fig. 4-14(b)** show Kriging surface of conversion ratio into MAPbI_3 . We found that high uniformity and high conversion of MAPbI_3 are important to get the high

efficiency of the solar cell; the conversion of MAPbI₃ has the high effect to efficiency than uniformity of perovskite thin film.

Fig. 4-15 shows the relationship between efficiency and input parameters (spin speed and dipping time). The efficiency from this graph comes from the simulation result of FF, J_{sc}, and V_{oc}. To search the global optimum condition, we chose the best condition point (Data group 2) at spin-coating rate vary from 3600 rpm and dipping time around 690-720 s. The optimum area of data set come from data group 1 and data group 2. The reason to have 2 group of data is the trading-off effect between film homogeneous and high conversion of MAPbI₃

Through this computational optimization, we chose the best condition as spin-speed at 3600 rpm and dipping time at 710 s. We made 6 devices under this condition and evaluated the device performance. The average efficiency under this condition is 8.04% with standard derivation of 0.42, and average J_{sc}=15.51 mAcm⁻², V_{oc}=1.03 V and FF=0.51. The full data of each device is shown in Table 4-4. The maximum efficiency of this experiment was 8.75% with J_{sc}=15.97 mAcm⁻², V_{oc}=1.03 V and FF=0.52, whose graph of the current-voltage characteristic is shown in **Fig. 4-16**. It is notable that all the optimization process was done only through 18 samples in total even though we have two experimental parameters with 12 levels, which ordinary means that 2¹²=4096 of samples are required for obtaining full information of the system. This improvement comes from (1) highly effective sampling of LHS method, (2) high accuracy of Kriging method for a few data sets, and (3) high effectiveness of NSGA-II for selecting the best point from Kriging result.

4.5 Conclusion

In conclusion, we have successfully fabricated PVSCs with structure ITO/SnO₂/Perovskite/Spiro-OMeTad/Au. This structure is a good candidate for flexible devices with low-cost material. To find the maximum efficiency, we optimized the experimental conditions using the Kriging model method from experimental data given through Latin hypercube sampling. With only 12 conditions of experiments, we could approximate the best condition for fabricating PVSCs as the spin speed 3600 rpm and dipping time 710s. Under this condition, we observed a high efficiency of PVSCs at 8.75% ($J_{sc}= 15.97 \text{ mAcm}^{-2}$, $V_{oc}=1.03 \text{ V}$, $FF=0.52$). From the LSH sampling, we could observe the spin-coating speed and MAI dipping time have strong relationships with efficiency due to the conversion ratio of PbI₂ to MAPbI₃ and the surface morphology of the perovskite film. This optimization method will allow researchers to go much faster through a variety of system in PVSCs.

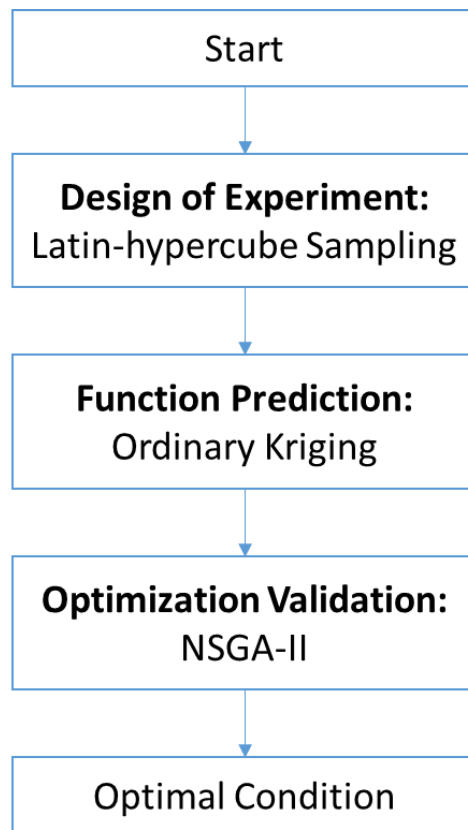


Fig. 4-1 Flowcharts showing the modelling and optimization process using in this report.

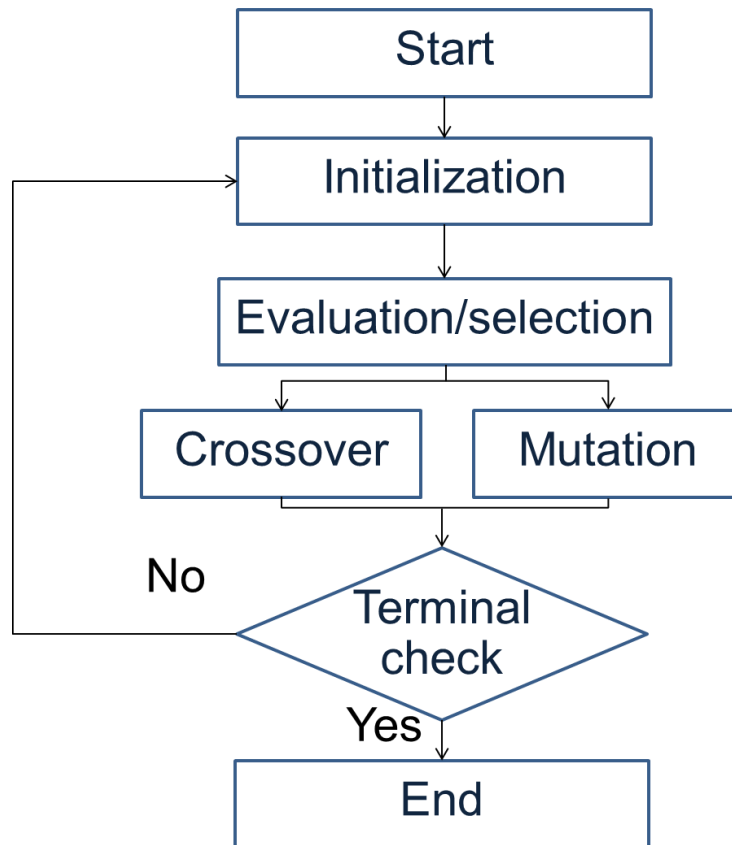


Fig. 4-2 Algorithms of simple GA.

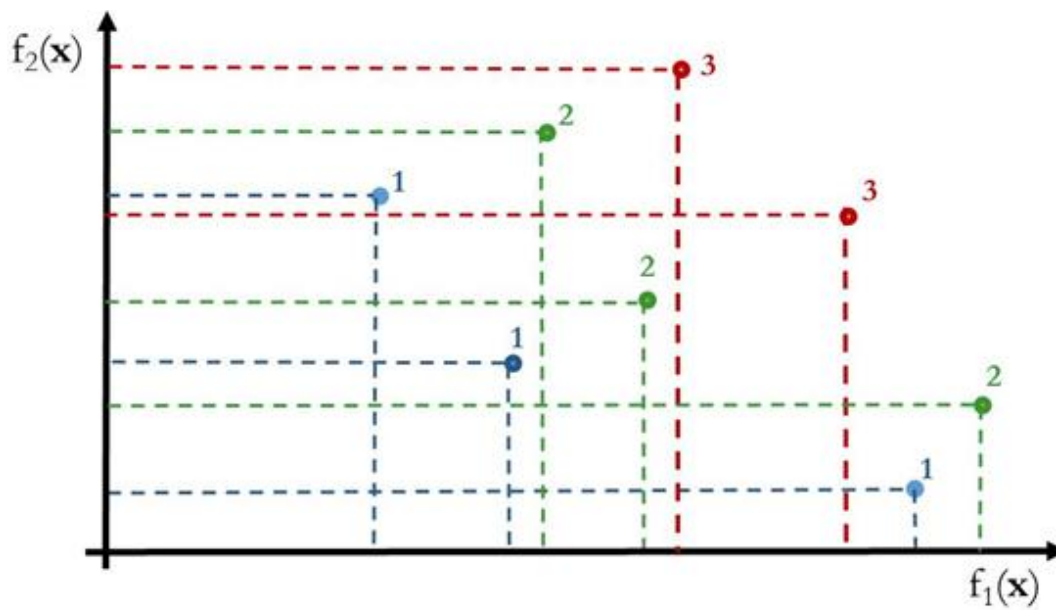


Fig. 4-3 Ranking by NSGA-II (Minimization of f_1 and f_2).

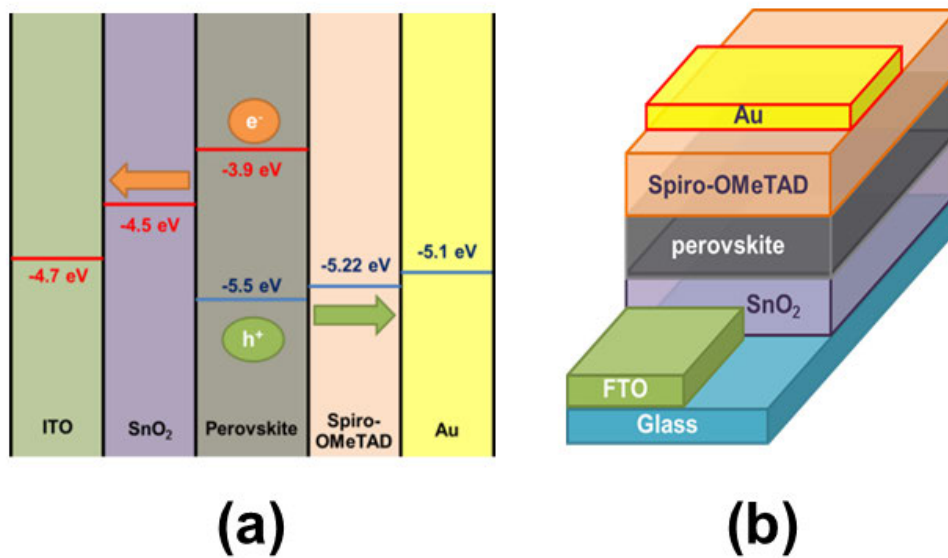


Fig. 4-4 a) Energy band diagram and b) Devices structure of our cell.

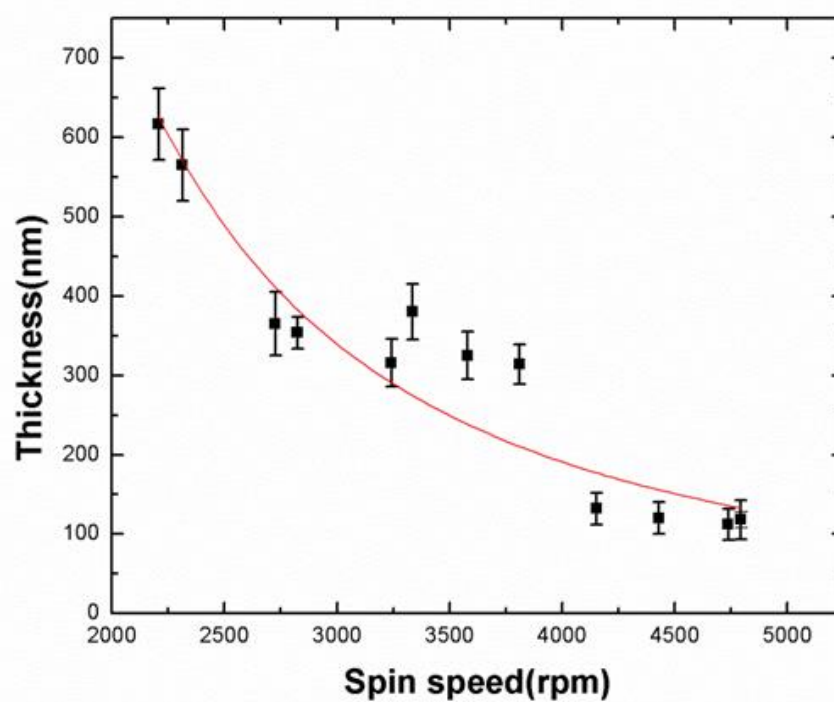


Fig. 4-5 Relation between spin-coating speed and thickness of perovskite layer

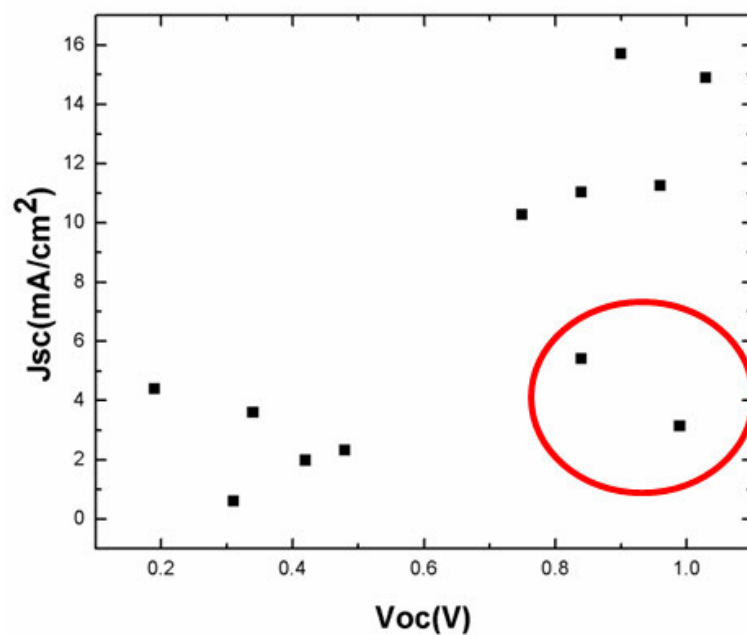


Fig. 4-6 Relationship between J_{sc} and V_{oc} from the original experimental data.

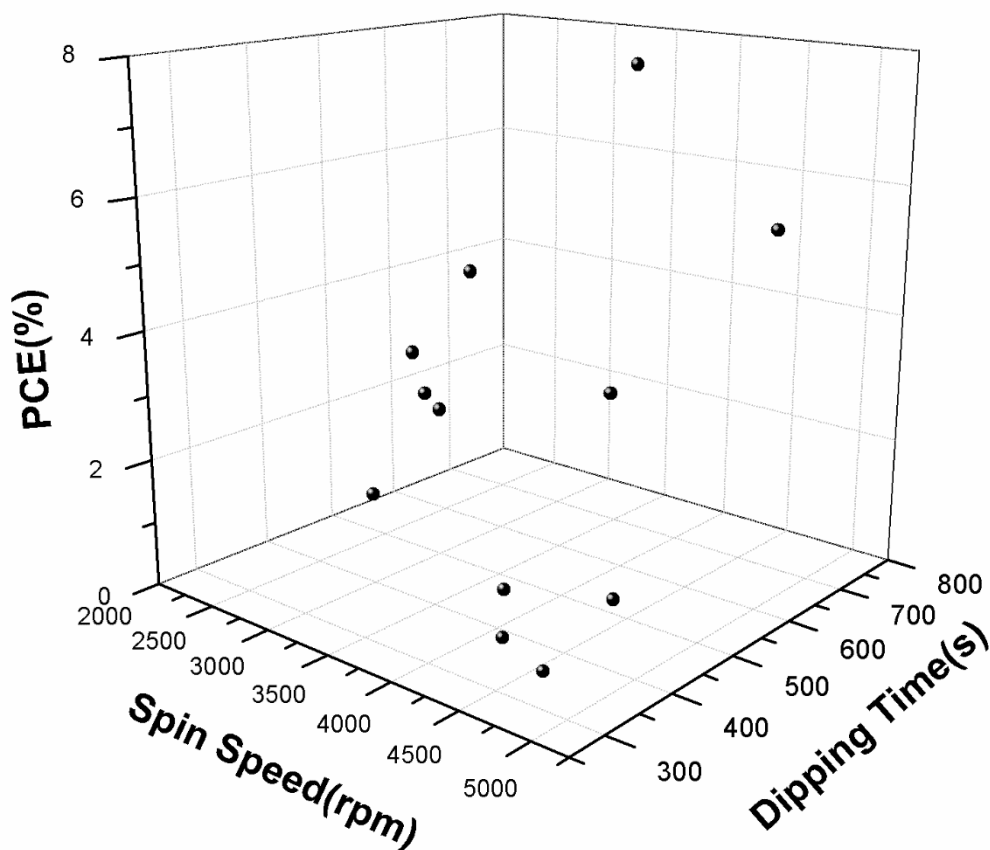


Fig. 4-7 Relationship between experiment parameters and efficiency of devices from original experimental data.

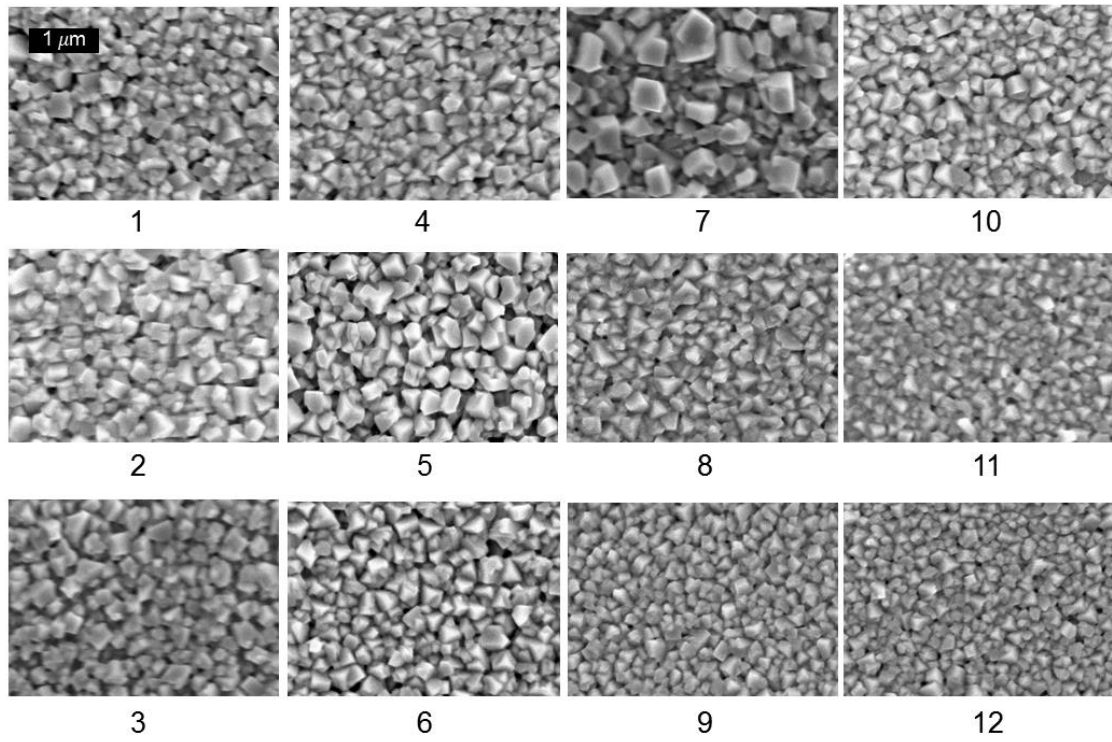
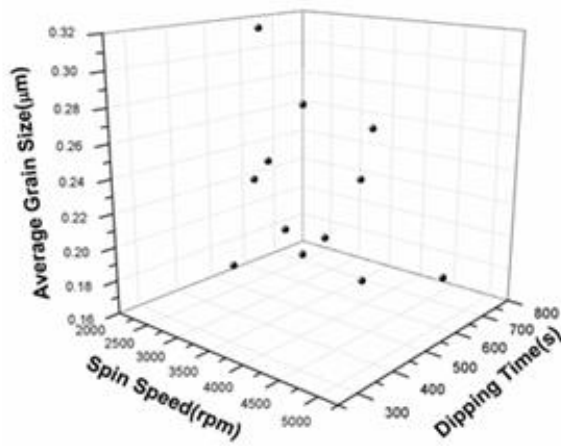
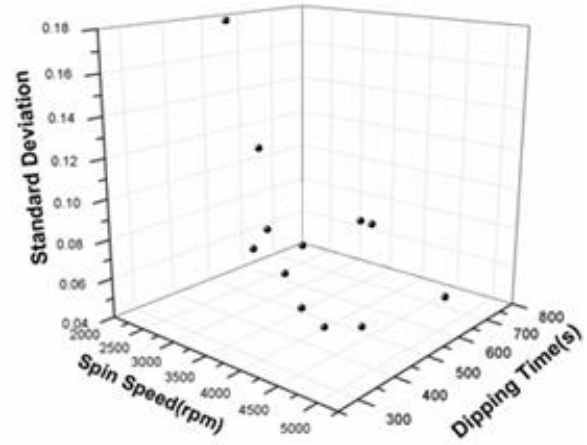


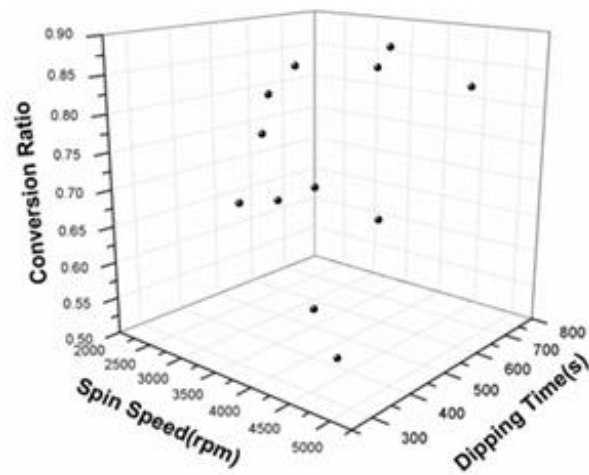
Fig. 4-8 SEM images of perovskite layer under conditions in **Table 4-1**



(a)



(b)



(c)

Fig. 4-9 Relationship between input parameters and a) the average grain size, b) Standard deviation and c) crystalline conversion ratio into MAPbI_3 .

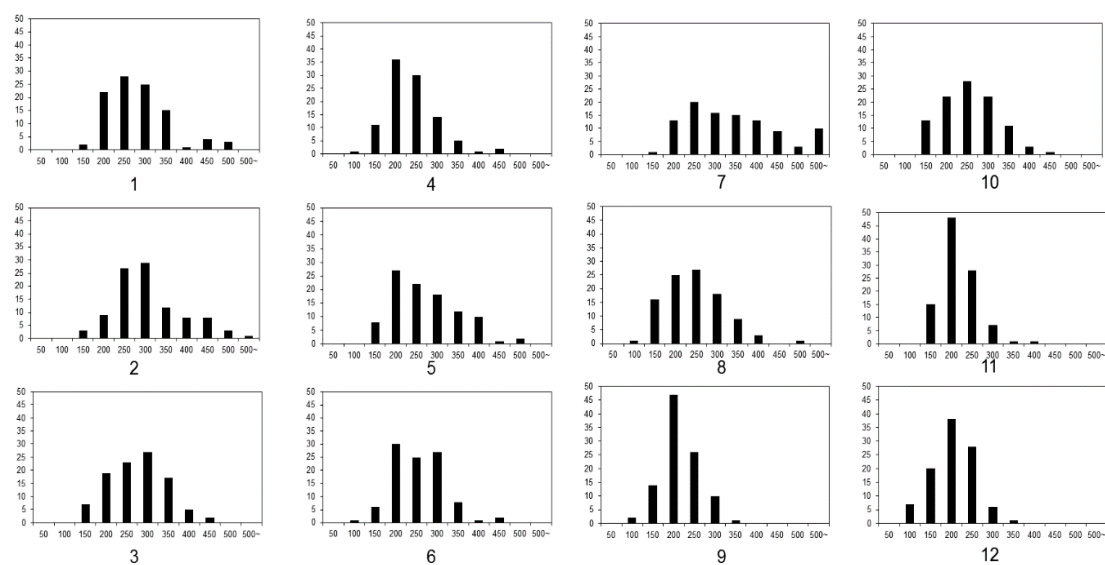


Fig. 4-10 Grain size distribution of perovskite thin film surface

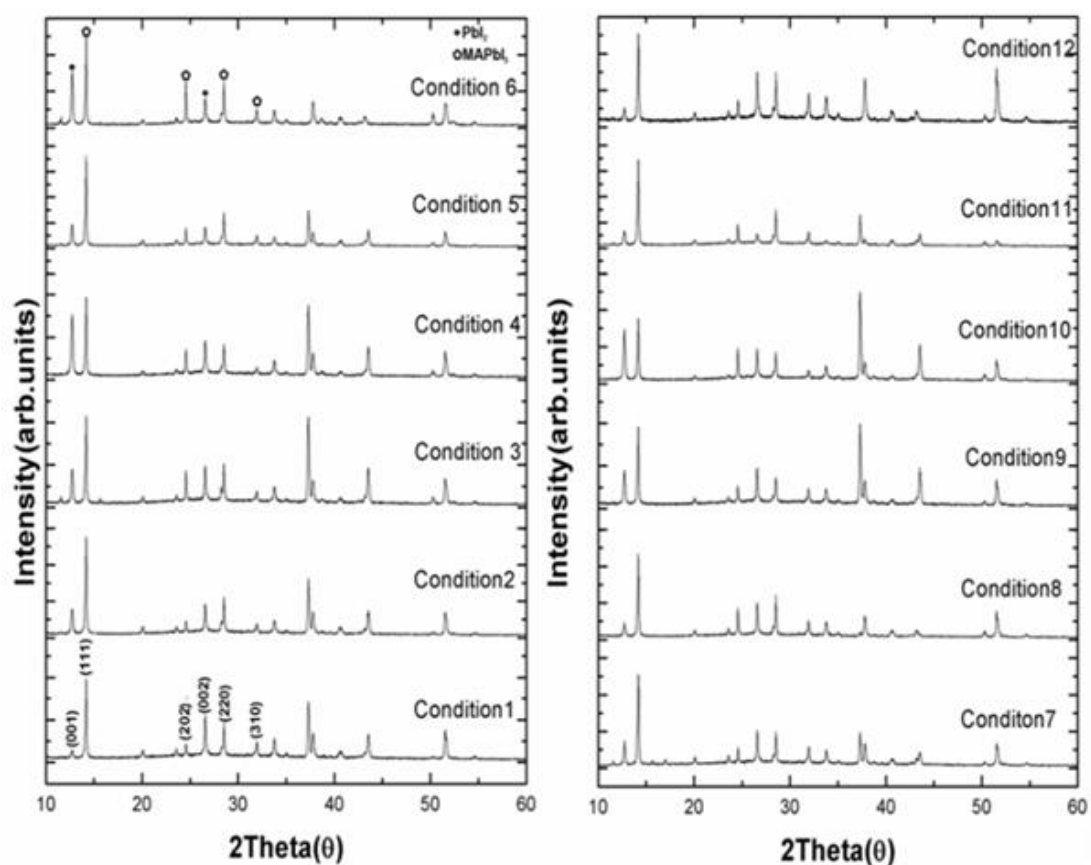


Fig. 4-11 The XRD spectra of perovskite layer on FTO/SnO₂ fabricated under conditions in **Table 4-1**.

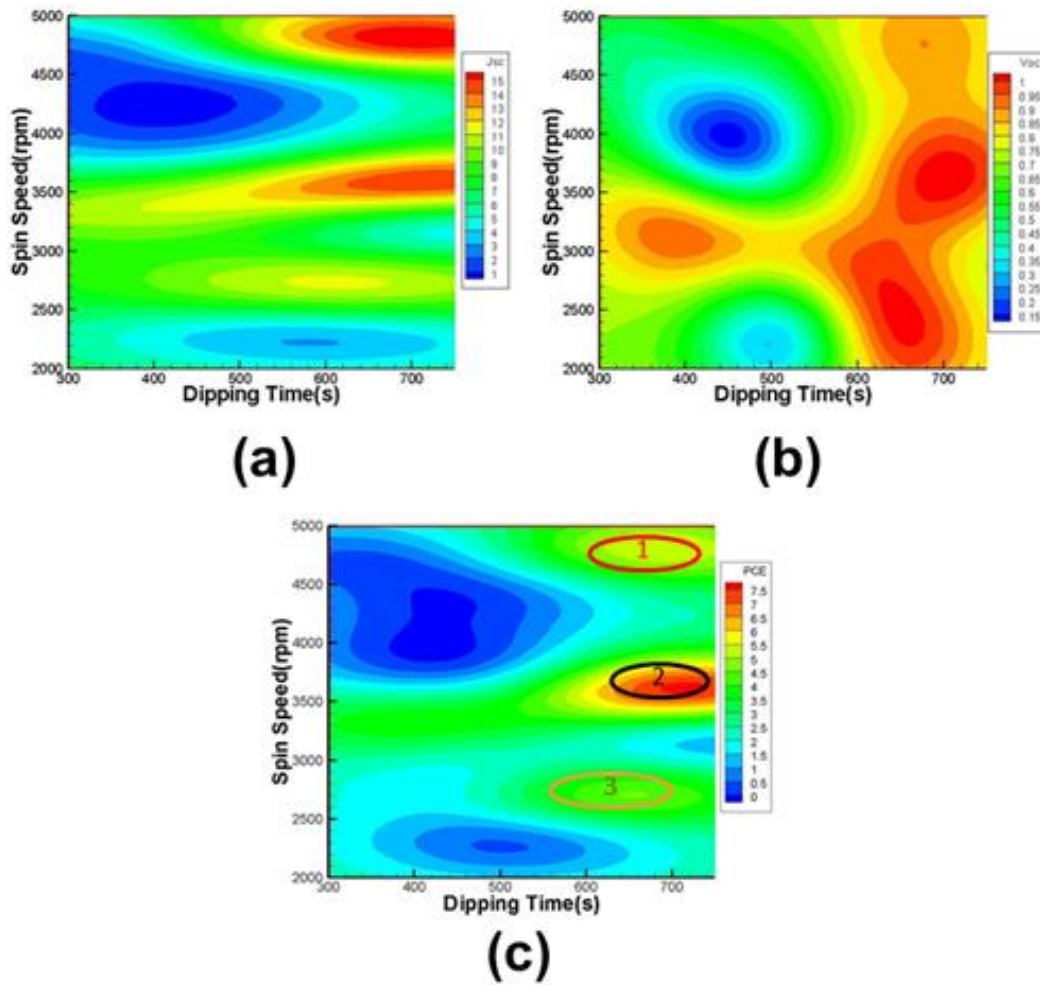


Fig. 4-12 Surface plot of the relationship between experimental parameters (Spin speed, time) and outputs a) short circuit current density (J_{sc}), b) open circuit voltage (V_{oc}) and c) power conversion efficiency.

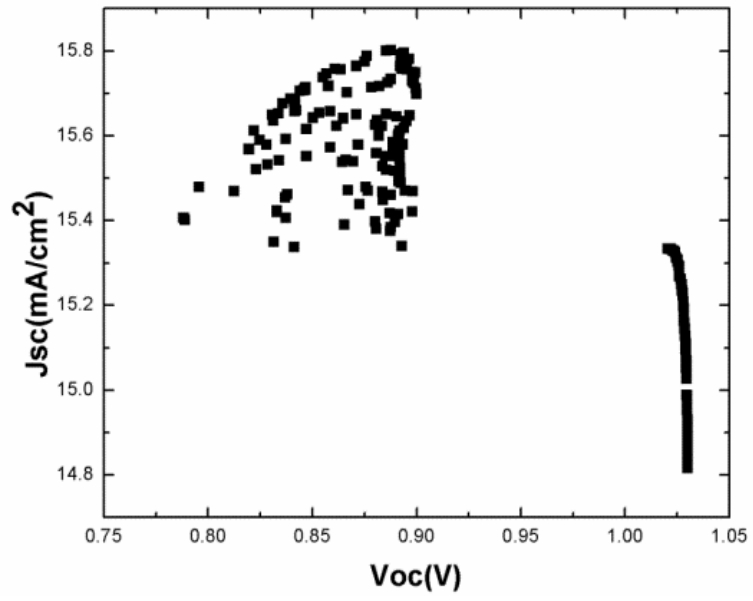
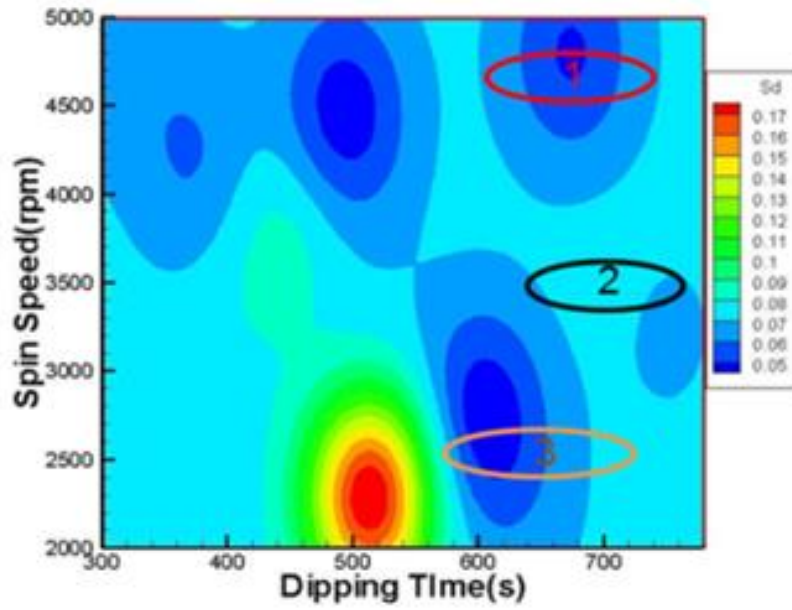
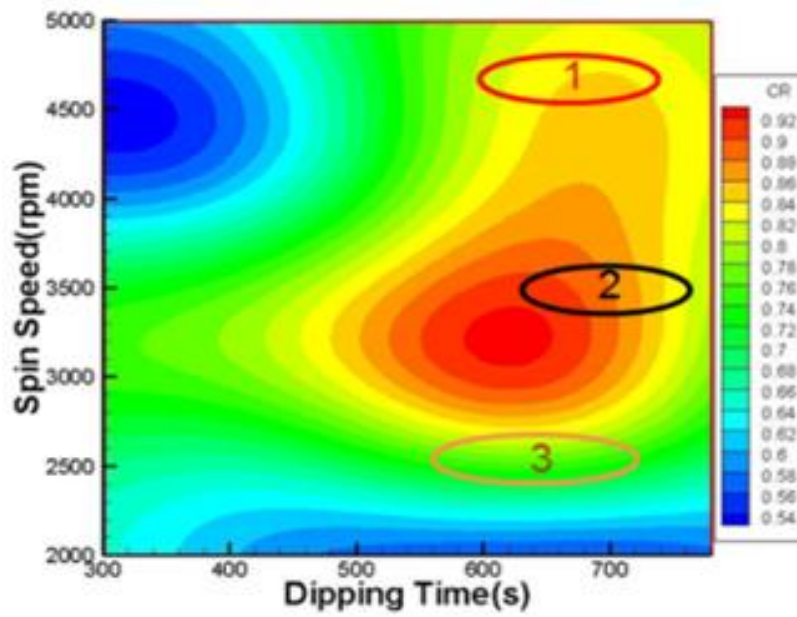


Fig. 4-13 Non-dominated solution of output parameters; V_{oc} , J_{sc}



(a)



(b)

Fig. 4-14 Surface plot of the relationship between experimental parameters (Spin speed, time) and a) S.D of grain and b) conversion of MAPbI₃.

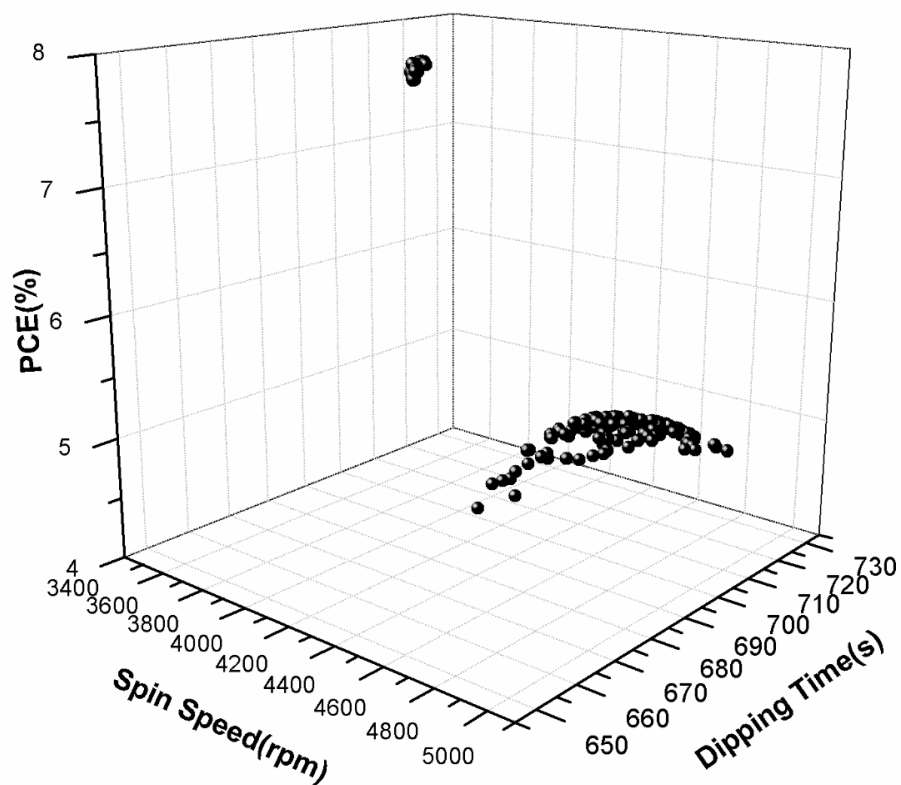


Fig. 4-15 Relationship of efficiency and input parameters (spin speed and dipping time) derived from NSGA-II.

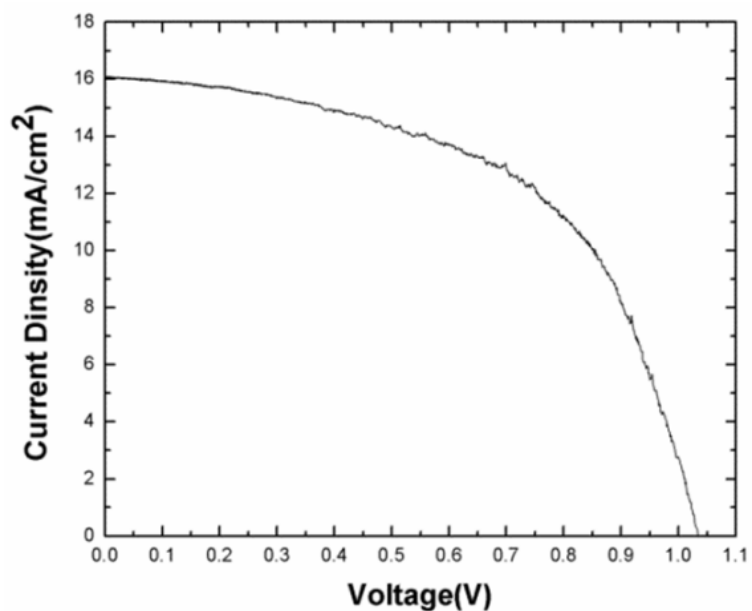


Fig. 4-16 Current-voltage characteristics of the highest performance devices fabricated with optimal condition.

Table 4-1 Input parameters for fabricating perovskite layer assigned by LHS method.

Condition	spin speed (rpm)	Dipping time (s)
1	3580	712
2	3810	447
3	2314	514
4	4152	378
5	3336	402
6	2208	644
7	2824	510
8	3242	748
9	4430	492
10	4738	320
11	2726	602
12	4794	674

Table 4-2 Output parameters of perovskite solar cells fabricated by using the conditions in **Table 4-1**.

Condition	Output			
	J_{sc} (mA/cm ²)	V_{oc} (V)	FF	PCE (%)
1	14.92	1.03	0.49	7.57
2	4.41	0.19	0.28	0.23
3	3.60	0.34	0.42	0.51
4	0.65	0.31	0.42	0.08
5	11.02	0.84	0.41	3.81
6	3.14	0.99	0.46	1.44
7	10.28	0.75	0.33	2.54
8	5.43	0.84	0.42	1.90
9	1.98	0.42	0.35	0.29
10	2.32	0.48	0.32	0.36
11	11.25	0.96	0.39	4.22
12	15.71	0.90	0.38	5.47

Table 4-3 The conversion ratio of PbI_2 to MAPbI_3 , grain size average and S.D value of perovskite grain when fabricated with difference condition

Condition	C_{MAPbI_3}	Ave. (μm)	STDEV.
1	0.87	0.25	0.07
2	0.71	0.28	0.08
3	0.65	0.17	0.18
4	0.58	0.21	0.06
5	0.78	0.24	0.08
6	0.62	0.23	0.06
7	0.81	0.32	0.12
8	0.83	0.22	0.07
9	0.68	0.19	0.04
10	0.55	0.23	0.06
11	0.84	0.19	0.04
12	0.83	0.18	0.05

Table 4-4 Current density-voltage parameters of perovskite solar cell when fabricated with optimal condition

Sample number	V _{oc} (V)	FF	J _{sc} (mA/cm ²)	Eff (%)
1	1.03	0.52	16.56	8.87
2	1.02	0.49	15.99	7.99
3	1.02	0.51	15.05	7.83
4	1.02	0.49	15.58	7.79
5	1.03	0.52	15.35	8.22
6	1.02	0.50	15.14	7.72

Reference

- [4-1] Docampo, P., Ball, J. M., Darwich, M., Eperon, G. E., & Snaith, H. J. (2013). Nature communications, 4.
- [4-2] Ball, J. M., Lee, M. M., Hey, A., & Snaith, H. J. (2013). Energy & Environmental Science, 6(6), 1739-1743.
- [4-3] Kumar, M. H., Yantara, N., Dharani, S., Graetzel, M., Mhaisalkar, S., Boix, P. P., & Mathews, N. (2013). Chemical Communications, 49(94), 11089-11091.
- [4-4] Kim, H. S., Lee, J. W., Yantara, N., Boix, P. P., Kulkarni, S. A., Mhaisalkar, S., Grätzel, M. & Park, N. G. (2013). Nano letters, 13(6), 2412-2417.
- [4-5] Ponseca Jr, C. S., Savenije, T. J., Abdellah, M., Zheng, K., Yartsev, A., Pascher, T., Harlang, T., Chabera, T., Pullerits, T., Stepanov, A. & Wolf, J. P. (2014). Journal of the American Chemical Society, 136(14), 5189-5192.
- [4-6] Saliba, M., Matsui, T., Seo, J. Y., Domanski, K., Correa-Baena, J. P., Nazeeruddin, M. K., Zakeeruddin, S.M., Tress, W., Abate, A., Hagfeldt, A. & Grätzel, M. (2016). Energy & Environmental Science, 9(6), 1989-1997.
- [4-7] Chen, Q., Zhou, H., Hong, Z., Luo, S., Duan, H. S., Wang, H. H., Liu, Y., Li, G. & Yang, Y. (2013). Journal of the American Chemical Society, 136(2), 622-625.
- [4-8] Wang, Q., Shao, Y., Dong, Q., Xiao, Z., Yuan, Y., & Huang, J. (2014). Energy & Environmental Science, 7(7), 2359-2365.
- [4-9] You, J., Hong, Z., Yang, Y. M., Chen, Q., Cai, M., Song, T. B., Chen, C.C., Lu, S., Liu, Y., Zhou, H. & Yang, Y. (2014). ACS Nano, 2014, 8 (2), pp 1674–1680

- [4-10] Ke, W., Fang, G., Liu, Q., Xiong, L., Qin, P., Tao, H., Wang, J., Lei, H., Li, B., Wan, J., Yang, G. & Yan, Y. (2015). *Journal of the American Chemical Society*, 137(21), 6730-6733.
- [4-11] Eperon, G. E., Burlakov, V. M., Goriely, A., & Snaith, H. J. (2013). *ACS nano*, 8(1), 591-598.
- [4-12] Kim, H. S., & Park, N. G. (2014). *The journal of physical chemistry letters*, 5(17), 2927-2934.
- [4-13] Ngo, T. A., Kim, J., & Kim, S. S. (2013). *Journal of Industrial and Engineering Chemistry*, 19(1), 137-143.
- [4-14] Beser, M. I., Beltrán, J., & Yusà, V. (2014). *Journal of Chromatography A*, 1323, 1-10.
- [4-15] Chen, M. J., Chen, K. N., & Lin, C. W. (2005), *Journal of Food Engineering*, 68(4), 471-480.
- [4-16] Bashiri, R., Mohamed, N. M., Kait, C. F., Sufian, S., & Hanaei, H. (2016). *Procedia Engineering*, 148, 151-157.
- [4-17] Minasny, B., & McBratney, A. B. (2006). *Computers & Geosciences*, 32(9), 1378-1388.
- [4-18] Pholdee, N., & Bureerat, S. (2015). *International Journal of Systems Science*, 46(10), 1780-1789.
- [4-19] Teixeira, A. L., & Falcao, A. O. (2014). *Journal of chemical information and modeling*, 54(7), 1833-1849.

- [4-20] Gao, Y., & Wang, X. (2008). The International Journal of Advanced Manufacturing Technology, 37(9), 953-960.
- [4-21] Ariyarit, A., & Kanazaki, M. (2015). Journal of Mechanical Science and Technology, 29(4), 1443-1448.
- [4-22] Horn, J., Nafpliotis, N., & Goldberg, D. E. (1994, June). IEEE World Congress on Computational Intelligence, Proceedings of the First IEEE Conference on (pp. 82-87). IEEE.
- [4-23] Jones, G., Willett, P., Glen, R. C., Leach, A. R., & Taylor, R. (1997). Journal of molecular biology, 267(3), 727-748.
- [4-24] Zhang, Y., Liu, M., Eperon, G. E., Leijtens, T. C., McMeekin, D., Saliba, M., Zhang, W. Bastiani, M., Petrozza, A., Herz, L.M., Johnston, M.B., Lin, H. & Johnston, M. B. (2015). Materials Horizons, 2(3), 315-322.
- [4-25] Mosconi, E., & De Angelis, F. (2016). ACS Energy Letters, 1(1), 182-188.
- [4-26] Li, H., & Zhang, Q. (2009). IEEE Transactions on Evolutionary Computation, 13(2), 284-302.
- [4-27] Deb, K., Pratap, A., Agarwal, S., & Meyarivan, T. A. M. T. (2002). IEEE transactions on evolutionary computation, 6(2), 182-197.
- [4-28] Kim, H. S., Lee, C. R., Im, J. H., Lee, K. B., Moehl, T., Marchioro, A., Moon, S.J., Humphry-Baker, R., Yum, Y.H., Moser, J.E., Grätzel, M. & Park. N.G. (2012). Scientific reports, 2, 591.
- [4-29] Song, J., Zheng, E., Bian, J., Wang, X. F., Tian, W., Sanehira, Y., & Miyasaka, T. Journal of Materials Chemistry A, 2015, 3(20), 10837-10844.

- [4-30] Zuo, C., & Ding, L. (2014). *Nanoscale*, 6(17), 9935-9938.
- [4-31] Nie, W., Tsai, H., Asadpour, R., Blancon, J. C., Neukirch, A. J., Gupta, G., Crochet, J.J., Chhowalla, M., Tretial, S., Alam, M.A. & Wang, H. L. (2015). *Science*, 347(6221), 522-525.
- [4-32] Ren, X., Yang, Z., Yang, D., Zhang, X., Cui, D., Liu, Y., Wei, Q., Fan, H. & Liu, S. F. (2016). *Nanoscale*, 8(6), 3816-3822.
- [4-33] Chen, C. C., Hong, Z., Li, G., Chen, Q., Zhou, H., & Yang, Y. (2015). *Journal of Photonics for Energy*, 5(1), 057405-057405.
- [4-34] Di Giacomo, F., Razza, S., Matteocci, F., D'Epifanio, A., Licoccia, S., Brown, T. M., & Di Carlo, A. (2014). *Journal of Power Sources*, 251, 152-156.
- [4-35] Hsieh, T. Y., Wei, T. C., Wu, K. L., Ikegami, M., & Miyasaka, T. (2015). *Chemical Communications*, 51(68), 13294-13297.

Chapter 5

Process Improvement for cm^2 Perovskite Solar Cell with Studies Effect of TiO_2

5.1 Introduction

Various material combinations have been used in the study of lead halide perovskite solar cells (PVSCs), which could potentially be fabricated as flexible devices and also fabricated with large areas as a commercial product [1-3]. The perovskite layer has many benefits, such as a high absorption coefficient, long carrier lifetime, and low recombination rate with a tunable bandgap [4-5]. In 2016, PVSCs achieved a maximum efficiency of over 22% in a paper co-written by researchers at KRICT and UNIST [6]. The efficiency of the PVSCs has been improved by testing different fabrication techniques, device structures, and optimizing the experimental parameters [7-9].

Most of the reports on improving the fabrication methods of PVSCs are focused on small device active areas (i.e. an active area smaller than 0.2 cm^2). There have only been a few investigations into cells fabricated with areas of several centimeters squared via methods such as doctor-blading, inkjet printing, spray deposition, and spin coating [10-12]. Le et al. fabricated large-scale PVSCs using a vacuum flash–assisted solution process [13]. By using such processes, the crystalline quality of perovskites has improved and power conversion efficiencies (PCEs) above 20% have been achieved. Gouda et al. developed a vapor treatment method for the surface of perovskite films and thus achieved a PCE of around 15% [14]; their findings demonstrated that improving the crystalline quality and homogeneity of perovskite films is beneficial for scaling up PVSC products. However,

the studies were all conducted with fabrication processes requiring a glove box with an inert atmosphere.

To date, there have only been a few reports on the fabrication of large-area PVSCs at atmospheric pressure [15] despite many research groups successfully developing PVSC fabrication processes at atmospheric pressure for small device areas ($<0.25 \text{ cm}^2$). Tai et al. fabricated PVSCs in ambient air using a $\text{Pb}(\text{SCN})_2$ solution [16]. Sveinbjörnsson et al. developed an ambient air process for mixed-ion perovskite films [17]. Most fabrication techniques for PVSCs developed at atmospheric pressure focus on solving the following problems that generally occur during fabrication, namely 1) the high degree of incomplete reactions leading to a high amount of PbI_2 remaining in the films; 2) the high number of pin-holes in the perovskite film surface; and 3) the low reproducibility of the film quality. It is not too difficult to solve these problems for small-area cells, but this problem has a large effect on decreasing the PCE when fabricating cells with areas $>1 \text{ cm}^2$.

Here, we designed a fabrication process for a perovskite layer that is referred to as the "dynamic spin-washing method", which involves a conventional mesoporous TiO_2 -based device to produce cells with areas $>1 \text{ cm}^2$ at atmospheric pressure (for a humidity level below 40%). The key component of this two-step method is the "dynamic spin-washing" process conducted after dipping the film into a MAI solution. This experiment demonstrates that our washing process has the potential to improve the uniformity and quality of perovskite crystalline thin films. Moreover, we also designed the experiments to optimize the deposition conditions for the electron transporting TiO_2 layer. After optimizing our process, we achieved a PCE of 13.5% for small-area devices and 11.8 % for large-area devices.

5.1.1 Fabrication method for perovskite layer

One of the crucial factor to improve the performance of PVSCs is morphology of perovskite thin film. Therefore, the fabrication process of PVSCs layer should be developed for higher surface coverage, crystalline quality and uniformity of perovskite layer. Until now, it has mainly 2 types of method for fabricated perovskite layer are one-step method and two-step method.[18-20]

5.1.1.1 One-step method

One-step method is first developed by Lee et al. in 2012. The original process for one-step method is shown in **Fig. 5-1**. [3] In that report, they were making stoichiometry precursors by containing 3:1 molar ration of MAI and lead chloride (PbCl_2) in DMF solvent. By using this technique, Lee et al can improved this technique for wearable devices with PCE around 10%. [18] After that, many research group try to be developed it with changing process parameters such as; changing the starting precursor, mixing with difference solvent and changing the proportion of precursors. However, simple one-step methods have big problem to control the reproducibility especially when fabricated in higher humidity condition.

To improve this problem, Xiao et al. report the surface improvement of perovskite thin film my adding an antisolvent on the top of wet precursor film during spin coating process. They found the difference type of antisolvent such as; chlorobenzene, benzene, toluene can improve the fast nucleation, which can be improved the micro size of perovskite crystal and improve the PCE close to 14%. [21] After that, Jeon et al. can improve the maximum PCE of that time by modify this technique by changing the precursors in mixture solvent contain; γ -butyrolactone (GBL) and DMSO with using toluene for antisolvent. After optimized the proportion of mixture solution, they can be achieved PCE

around 16.2%. After that this method is one of the best choice to fabricated perovskite layer with many type of modification method such as; changing solvent, changing starting precursor or changing the type of antisolvent.[22]

5.1.2.1 Two-step method

Two-step method is the first method to fabrication perovskite solar cell by miyazaka et al in 2009.[2] This method is starting to fabricate by first; deposition PbI_2 thin film by coating PbI_2 in DMF solvent with difference method such as; spin coating, spray or thermal evaporation. [23-25] Then convert the PbI_2 thin film to perovskite by dipping PbI_2 precursor thin film in MAI solution, during this process the color of precursor film were convert from yellow to black-brown color. The conversion process of PbI_2 to perovskite is shown in **Fig. 5-2**. [26] By fabricated PVSCs by this method, Burschka et al. can achieved PCE over 15% on mesoporous TiO_2 layer.[27] However, this method has problem to control the amount of perovskite conversion.

To improve this problem, Docampo et al. modify this method by mixing MAI and MACl together. The result is PCE can improve to 15.7% by improved the high conversion rate of perovskite crystal.[28] After that, many research group try to increase the conversion of perovskite crystal such as spin-coating with higher concentrated of MAI solution [29], pre-wetting of solvent [30] and using solvent vapor annealing [31]. The modification of two-step process not only improved the conversion of MAPbI_3 ratio. However, they can be improved the grain size and homogeneous of thin film that have benefit for improved the scale up PVSCs. Yang et al. explain the mechanism for conversion PbI_2 crystal to MAPbI_3 crystal: named in-situ conversion. The morphology of PbI_2 crystal is converted to MAPbI_3 by incorporation of MAI ions. However, the PbI_2 crystal dissolves and the perovskite recrystallizes in a thermodynamically favored shape[32]. After that, this

concept was developed for improve the conversion rate of MAPbI₃ crystal of two-step method.

5.2 Experiment

5.2.1 Substrate preparation

FTO glass substrates (2 cm × 2.5 cm) were etched with HCl and zinc power. After that, the pattern-etched FTO substrates were cleaned by ultrasonication in deionized water, acetone, and ethanol (20 min in each solvent) and dried by blowing air onto them.

5.2.2 Devices Fabrication

The overall process for this experiment is shown in **Fig. 5-1**. In this experiment, we fabricated a dense layer of TiO₂ by spin coating a solution composed of 0.1 M titanium diisopropoxide bis(acetylacetonate) (Sigma-Aldrich) dissolved in n-butanol (99%, Wako) at 3000 rpm. Then, the samples were annealed at 150 °C for 5 min. These processes were repeated three times to deposit a dense TiO₂ precursor film. After that, the films were annealed at 500 °C for 60 min. After cooling, the mesoporous TiO₂ layer was deposited by spin coating 0.4 g of TiO₂ nanoparticles diluted in ethanol (1.4 g) at 3000 rpm for 30 s; the samples were then post-annealed at 500 °C for 60 min. To prepare the perovskite layer with the two-step method, 1 M of PbI₂ was dissolved in a mixed solvent that contained dimethylformamide (DMF, 99%, Wako) and dimethyl sulfoxide (DMSO 99%, Wako). The volume ratio of the solvents was 9:1. The samples and precursor solutions were preheated at 70 °C before deposition. The precursor solution was coated onto the substrate by spin coating (typically at 500 rpm for 3 s and subsequently at 5000 rpm for 30 s). The PbI₂ films were annealed at 70 °C for 15 min to remove the remnant

solvent in the film. After the surface temperature of the PbI_2 thin films decreased to room temperature, the samples were typically dipped into the MAI solution (10 mg mL^{-1} in IPA) for 90 s. Then the perovskite thin films were transferred to the spin coater to remove the remaining solution on the surface by spinning at 4000 rpm with IPA for 30 s. After that, the films were annealing at 90°C for 30 min. To fabricate the hole transport layers, the samples were spin coated at 4000 rpm with a solution of the hole transport material. This solution was prepared by mixing 68 mM of spiro-OMeTAD (Sigma-Aldrich), 26 mM Li-TFSI (Sigma-Aldrich), and 55 mM 4-tert-butylpyridine (TBP, Sigma-Aldrich) in acetonitrile and chlorobenzene ($V/V = 1:10$). Finally, 100-nm-thick gold electrodes were deposited by magnetron sputtering. The active device area was 0.09 cm^2 for the small surface area and 1 cm^2 for large surface area devices. **Fig.5-2** show the image of 1 cm^2 scale area PVSCs when fabricate with modified two-step method.

5.2.3 Characterization

The surface topographies of the perovskite layers were studied using a field emission scanning electron microscope (FE-SEM, S-4700, Hitachi, Japan) with an accelerating voltage of 5 kV. The thickness of each layer was measured by stylus profilometry (Dektak 3030, ULVAC, Japan). Light transmittance between wavelengths of 200 to 1000 nm was measured using spectrophotometry (UVmini-1240, Shimadzu, Japan). The crystallization of the perovskite layer was analyzed via X-ray diffraction (XRD, D8 DISCOVER, Bruker, USA) using $\text{Cu K}\alpha$ radiation (40 kV at 40 mA) with a scan rate and a step size of 2 deg/min and 0.01 deg/min. The surface elemental composition of the samples was identified by XPS (JEOL JPS-9000MX). The current density–voltage (J–V) characteristics of the solar cells were measured using an AM 1.5 solar simulator (100 mW cm^{-2}) and an automatic polarization system (Hokuto Denko HSV-100) that used a 500 W Xe lamp (UXL-500SX, Ushio) as a light source.

5.3 Result and Discussion

5.3.1 Surface modification by dynamic spin coating

In this experiment, we fabricated a perovskite solar cell by modifying a two-step spin method for a mesoporous TiO₂ based structure, namely for a FTO/dense TiO₂/mesoporous TiO₂/perovskite/spiro-OMeTAD/Au stack. This structure has already been improved to achieve a very high PCE (over 20%) in many reports [33,34]. However, only a few studies succeeded to fabricate this structure in ambient air and for a large surface area; this is because of the difficulties in controlling film uniformity to achieve fewer pin-holes and a high reproducibility of the film quality [35]. To modify the two-step spin method, we changed the washing process for the perovskite film by dropping IPA onto the samples during the spin coating of the film.

Fig.5-5 shows the perovskite surface characteristics via SEM and AFM images. From this figure, we can observe that the surface morphology changes depend on the spin speed of the IPA during the washing of the perovskite thin film. The lower the surface roughness of the perovskite films is, the more the efficiency of the solar cell can be improved. The surface of the perovskite thin films appears smoother for higher washing spin speeds. Moreover, we observed that the surface roughness of the perovskite films dropped from 74 nm when washing at 2000 rpm to 35 nm when washing perovskite thin film at 4000 rpm. The surface roughness of the perovskite films was measured by AFM. Not only did the smoothness of the perovskite film surface increase, the number of pin-holes also decreased when the washing spin speed was increased.

The crystalline quality of the perovskite films is an important parameter to optimize the PCE of PVSCs. One way to investigate the quality of a perovskite layer is via XRD. **Fig.**

5-6 shows the XRD pattern of a perovskite thin film washed with IPA at different spin speed. In a previous report on assessing the crystalline quality of a perovskite thin film, Hsieh et al. defined the conversion ratio of PbI_2 into methylammonium lead iodide (MAPbI_3) with following equation [36];

$$C_{\text{MAPbI}_3} = \frac{I_{14.2}}{I_{12.7} + I_{14.2}} \quad [5-1]$$

where $I_{12.7}$ is the intensity of the PbI_2 peak at 12.7° and $I_{14.2}$ is the intensity of the MAPbI_3 peak at 14.2° . The values of the conversion ratio when changing the washing spin speed are shown in the **Table 5-1**. We found that a large amount of PbI_2 remained at low washing spin-speeds. A higher conversion ratio of MAPbI_3 was observed when we increased the spin-washing speed.

5.3.2 Investigated the surface morphology change

We designed an experiment to investigate the phenomena that cause the formation of high roughness films and different conversion ratios for different spin speeds. First, a PbI_2 thin film was deposited via spin coating on top of the TiO_2 layer and dried to evaporate the solvent in the PbI_2 thin film; after that, the film was dipped into the MAI solution. Then, the sample was mounted onto the holder of the spin coater and we waited until some areas of the film were dried (as shown in a photograph in **Fig. 5-7**); subsequently, we conducted the dynamic spin-washing step. **Fig. 5-7** shows a picture of the sample before and after using the dynamic spin-washing method, highlighting the surface morphology of the dry and the wet area. The dry area of the sample reveals a non-uniform perovskite film with a rough surface area. Further, **Fig. 5-7** demonstrates that the surface of the perovskite film was directly affected by the IPA evaporation: this is because we observed a smooth and

uniform surface in the wet area of the film before the dynamic-spin drying process. Not only was the film's surface affected by the presence or absence of the solvent, but the crystalline quality of the PbI_2 appeared also to be much higher in the dry area than in the wet area; the XRD result of dry surface area and wet surface area are shown in the **Fig. 5-8** and **Table 5-2**.

To explain the reason for the differences in the structures and the quality of PbI_2 when washing and drying the film with difference spin-speeds, we needed to model the results of Koo et al [37]. In that report, they investigated the effects of water and IPA content in air in a single wafer cleaning system. Their simulation showed that the content of water and IPA in the air and the spin-speed rate are related to the evaporation rate of the IPA and water; further, a higher evaporation rate of both water and IPA was confirmed when the spin-speed was increased. Additionally, the evaporation rate of water is lower than that of IPA owing to the higher boiling point of water. In humid conditions, it is necessary to consider the influence of water condensation. This phenomenon is harmful to the surface of perovskite films because the perovskite surface readily reacts with water, converting the surface back to PbI_2 [38]. **Fig. 5-9** shows the schematic of the film formation process for different film surfaces. For the dry part of film at atmospheric pressure, the amount of condensed water (from water vapor in the ambient air) is higher than the amount of water evaporated from the perovskite surface; thus, the presence of ambient vapor that condenses on the surface converts an additional portion of the perovskite film into PbI_2 . Moreover, the evaporation rate of IPA is non-uniform owing to the amount of IPA on the surface not being the same across the entire area of the film; for example, areas at the edge of the film have a lower IPA content than central areas. For this reason, the surface of a normal dry process results in a non-uniform film with a high surface roughness. Moreover, it can be seen from a cross sectional image (shown in **Fig.**

5-10) that the wet and dry areas have different thicknesses; different surface morphologies of the perovskite film were formed during the waiting step while the films dried. The MAI solution did not dry uniformly and some areas retained a small amount of solvent. In the completely dried area the film thickness gradually decreased as the size of the crystallites from the re-converted perovskites to PbI_2 grew. Schlipf et al. reported that the size of a perovskite crystal is larger than that of PbI_2 [39]. At a low washing spin-speed, the water evaporation rate is still higher than the water condensation rate, and thus the surface of the film also has a high surface roughness. However, the conversion of perovskite crystals into PbI_2 is lower than for the normal dry fabrication case because of the reduced amount of water on the surface owing to a higher rate of water evaporation. At high washing spin-speeds, the water evaporation rate is lower than the rate of water condensation. Thus, most of the perovskite surface has a low surface roughness with a low amount of residual PbI_2 , because the surface of the film is not converted into PbI_2 owing to the low amount of water in the vicinity of the film surface.

Table 5-3 shows the J–V parameters for the small area PVSCs fabricated with different IPA spin-washing speeds. These results show a correlation between the spin speeds and the surface morphology and crystalline quality of the perovskite films. The PCE of the PVSCs gradually increased as we increased the spin-washing speed. We observed a significant increase in the fill factor (FF) and short-circuit current density (J_{sc}); the FF increased from 0.47 to 0.59 and J_{sc} increased from 16.5 to 22.5 mA/cm^2 . The J–V curves also confirmed that the dynamic spin-washing method can improve the PCE of PVSC devices. In particular, in the case of the 1- cm^2 -area device, the PCE of the devices when washing at 4000 rpm were almost double than those at 2000 rpm. The J–V parameters of large area PVSCs fabricated with different washing IPA spin speeds are shown in **Table 5-4**. When we fabricated perovskites with a large surface area, the benefit of our method

could be more clearly observed because of the higher crystalline uniformity and area of the perovskite coverage required for the large-scale device [39-41]. The FF increased from 0.32 to 0.53 when we increased the washing speed from 2000 to 4000 rpm and the J_{sc} increased from 15.3 to 19.7 mA/cm².

5.3.3 Optimization by Design of experiment

To optimize the efficiency of the PVSC devices in this experiment we chose the experimental methods using the kriging model to optimize the TiO₂ layer; this method was already used in our previous studies and a diagram for the optimized parameters. [42] In this study, we optimized the TiO₂ layer, as this layer has a large impact on increasing the V_{oc} and J_{sc} by reducing the recombination at the interface between the perovskite layer and the FTO substrate [43]. In a device with a mesoporous structure there are two kinds of TiO₂ layers, the first of which is a dense TiO₂ layer and the second of which is a mesoporous TiO₂ layer. Therefore, we selected the input parameters to be the spin-speed for fabricating a dense TiO₂ layer (Spin Speed 1) and the spin-speed for fabricating a mesoporous TiO₂ layer (Spin Speed 2). To optimize the real effect of the TiO₂ layer and to reduce the cost of optimization, we designed a half-cell that has no hole transporting layer.

5.3.4 The selection of parameters range

Before starting to design the experiment, we set the parameter values of the dense TiO₂ layer by fabricating devices with only a dense TiO₂ layer and a perovskite layer (FTO/dense TiO₂/perovskite/Au). By changing the spin-speed for fabricating the dense TiO₂ layer we estimated the range of input parameters.

The J–V parameters of the PVSCs fabricated with different spin speeds for the compact TiO₂ layer are shown in **Table 5-5**. From this table, we could choose the range of spin

speeds for fabricating the films (around 2000 to 6000 rpm). The reasons we chose this range were 1) we observed a high PCE at spin speeds of around 3000 rpm, and 2) we observed a high FF at 5000 rpm. The film thickness of the dense TiO₂ films was measured using profilometry. We plotted the relationship between the film thickness of the dense TiO₂ layer and the spin speed in **Fig. 5-11**. This graph shows that the thickness of the dense TiO₂ layer was inversely proportional to the spin speed for fabricating the TiO₂ layer.

We started the design of the experiment by choosing the parameters by Latin hypercube sampling (LHS). **Table 5-6** shows the input parameters for fabricating the dense and mesoporous TiO₂ layers assigned by LHS [44]. The benefit of random data sampling by LHS is that we can decrease the number of experiments while maintaining uniformity throughout the experimental space. The optimization problem can be written as follows:

Maximize: f1 = J_{sc}

Maximize: f2 = V_{oc}

Maximize: f3 = FF

Maximize: f4 = PCE

Subject to: 2000 rpm ≤ Spin Speed 1 ≤ 6000 rpm

2000 rpm ≤ Spin Speed 2 ≤ 6000 rpm

After we randomly selected the input parameters, we ran the experiment and got the output parameters. The output parameters were the J–V parameters (J_{sc}, V_{oc}, FF, and PCE). Fig. 4 shows the relationship between the input and the output parameters (J_{sc}, V_{oc},

FF, and PCE) from the original experimental data. The output parameters found based on the input parameters gathered using the LHS method are shown in **Table 5-7**.

We observed a large difference in the efficiency when we changed the dense and mesoporous TiO₂ layer; thus, these input parameters are effective for determining the optimum parameters for the experiment.

5.3.5 Predicting the mapping surface via Kriging model

Applying the output parameters in the kriging model [45-46] yielded the computational optimization results shown in **Fig. 5-12**. This figure shows the simulation of the output surface distribution for the J_{sc}, V_{oc}, FF, and PCE. From these surface plots, we can approximate a reasonable region for the input parameters to achieve a high output value.

Fig. 5-12 (a) and (b) show the effect of the input parameters on J_{sc} and V_{oc}. We can observe that Spin Speed 2 (mesoporous TiO₂) has a large effect on J_{sc}. **Fig. 8(c)** shows the effect of the input parameters on FF. With regards to choosing the range of parameters for the experiment, the input parameter FF is related only to Spin Speed 1 (dense TiO₂) with a near linear relationship. Based on the data in **Fig. 12(d)** we can approximate the best conditions for fabricating the TiO₂ layer; the best conditions for fabricating dense TiO₂ are a spin speed of around 5600–5800 rpm and for mesoporous TiO₂ a spin speed of around 2400–2600 rpm is ideal. Therefore, we chose 5700 rpm for the dense TiO₂ layer and 2500 rpm for the mesoporous TiO₂ layer.

We made 6 small and 3 large-area devices under these conditions and evaluated the device performances. The average efficiency was 5.81% with a standard deviation of 0.25% and an average J_{sc} of 12.01 mA cm⁻², V_{oc} of 0.80 V, and FF of 0.57. Current density-voltage parameters of each cells are shown in **Table 5-8**. The maximum efficiency in this

experiment under optimized conditions for fabricating TiO₂ with a full cell are given in **Table 5-9** along with the results of the best cells and the average values. The average for a small-area device was 13.47% and the average J_{sc} , V_{oc} , and FF values were 21.21 mA cm⁻², 0.99 V, and 0.64, respectively. The average for the large-area devices was 11.47%, and the average J_{sc} , V_{oc} , and FF values were 19.53 mA cm⁻², 0.99 V, and 0.59, respectively. Current density-voltage parameters of each cells are shown in **Table 5-10**. **Fig. 5-13** shows the J–V characteristics of the highest performance cell of (a) the small-area devices and of (b) the large-area devices when fabricated under optimized conditions.

5.4 Conclusion

In conclusion, we fabricated PVSCs at atmospheric pressure with a ITO/dense TiO₂/mesoporous TiO₂/perovskite/Spiro-OMeTAd/Au structure with a large surface area by using a modified dynamic spin-washing method. We found that a high spin-washing speed had a significant effect on increasing the PCE by preventing vapor reactions. Vapor reactions strongly effect re-conversion of perovskites into PbI₂ and cause the surfaces of perovskite films to be rough. From this experiment, we conclude that not only is the growth of the crystalline phase of the perovskite film important, but the washing step of the perovskite film is also important when it comes to scaling up the area of PVSCs. Lastly, we succeeded in achieving a PCE of 13.5% for a device area of 0.09 cm² and 11.8% for a device area of 1 cm² by using the optimized process. This modified two-step method will allow researchers to develop PVSCs for practical devices or commercial products in the near future.

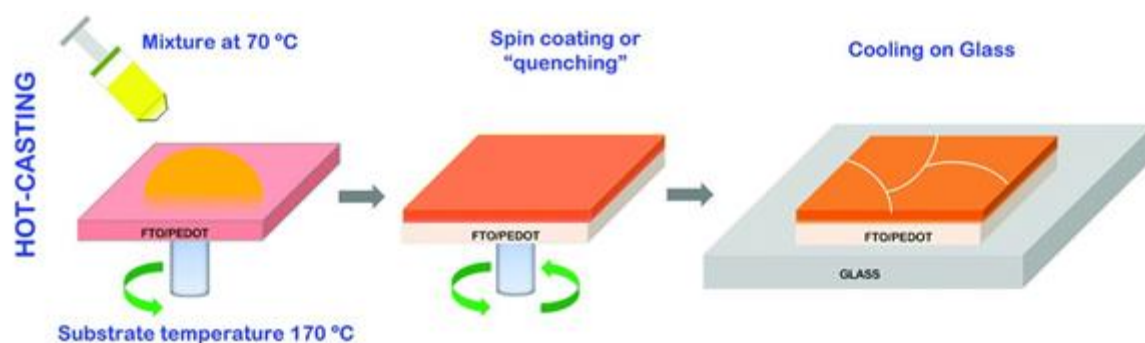


Fig. 5-1 Schematic of one step method deposition. Reprint with permission form.[3]

Copyright 2015, The American Association for the Advancement of Science.

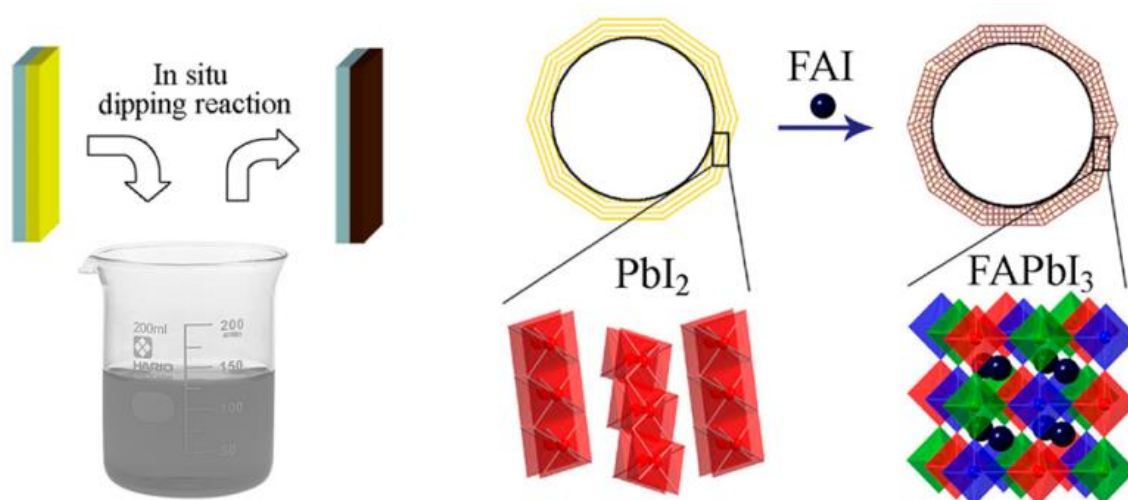


Fig. 5-2 (a) Schematic illustration of in situ formation of FAPbI₃ by in situ dipping reaction of PbI₂ and FAI on the TiO₂ surface. Reprinted with permission form.[26]

Copyright 2015, American Chemical Society.

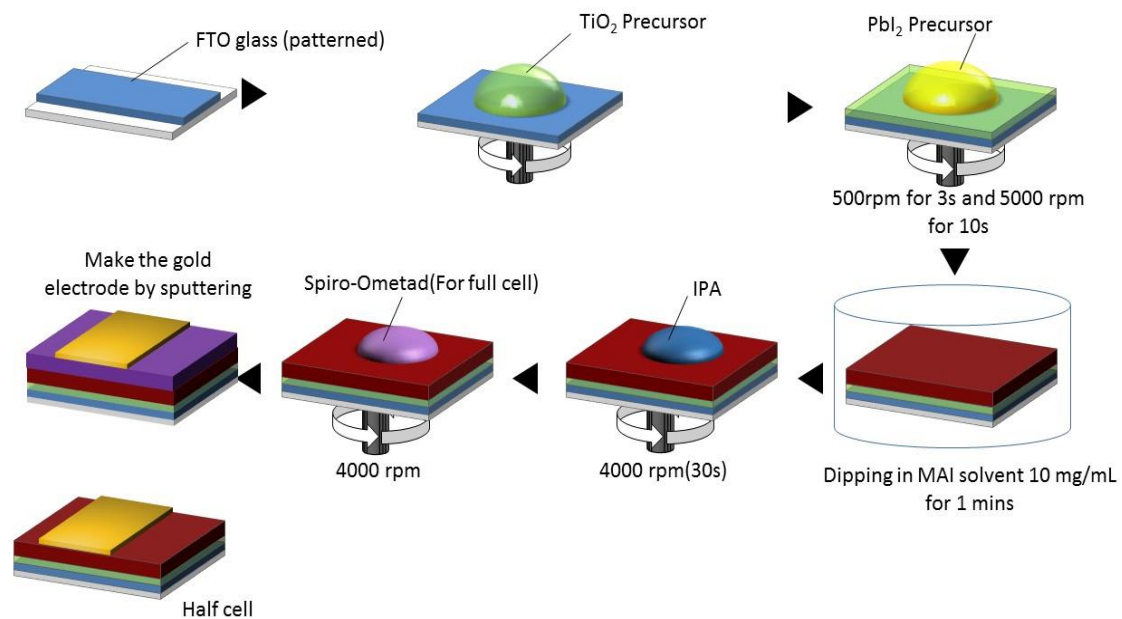


Fig. 5-3 Schematic of fabrication of perovskite solar cell based on the modified two-step spin method.

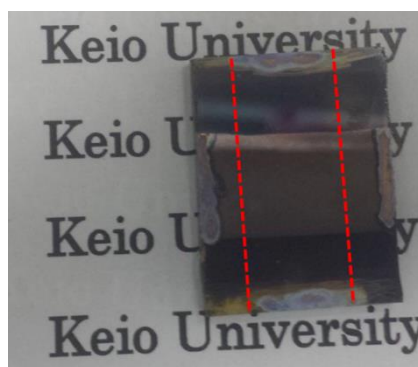


Fig. 5-4 The image of 1 cm² scale area PVSCs when fabricate with modified two-step method.

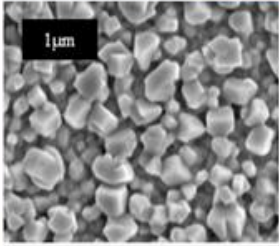
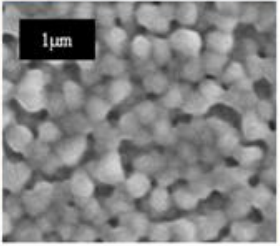
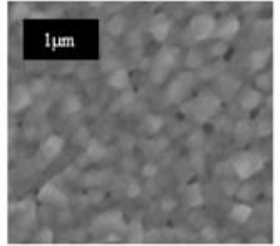
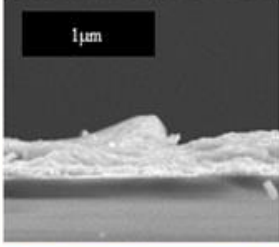
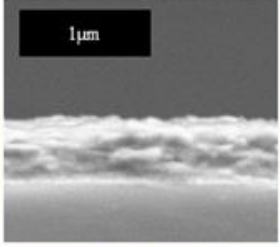
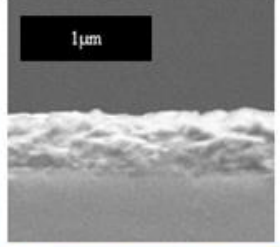
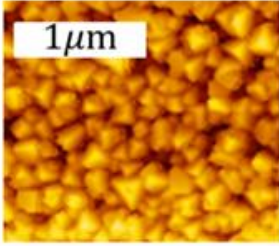
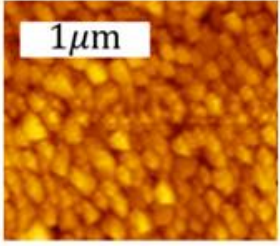
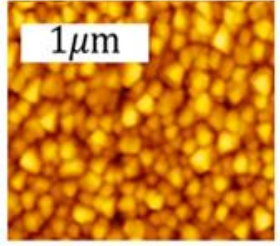
Spin-Speed	2000 rpm	3000 rpm	4000 rpm
SEM Top View			
SEM Cross section			
AFM			
Roughness	74 nm	35 nm	35 nm

Fig. 5-5 Surface morphology analysis of perovskite layer when washing surface with different spin speed.

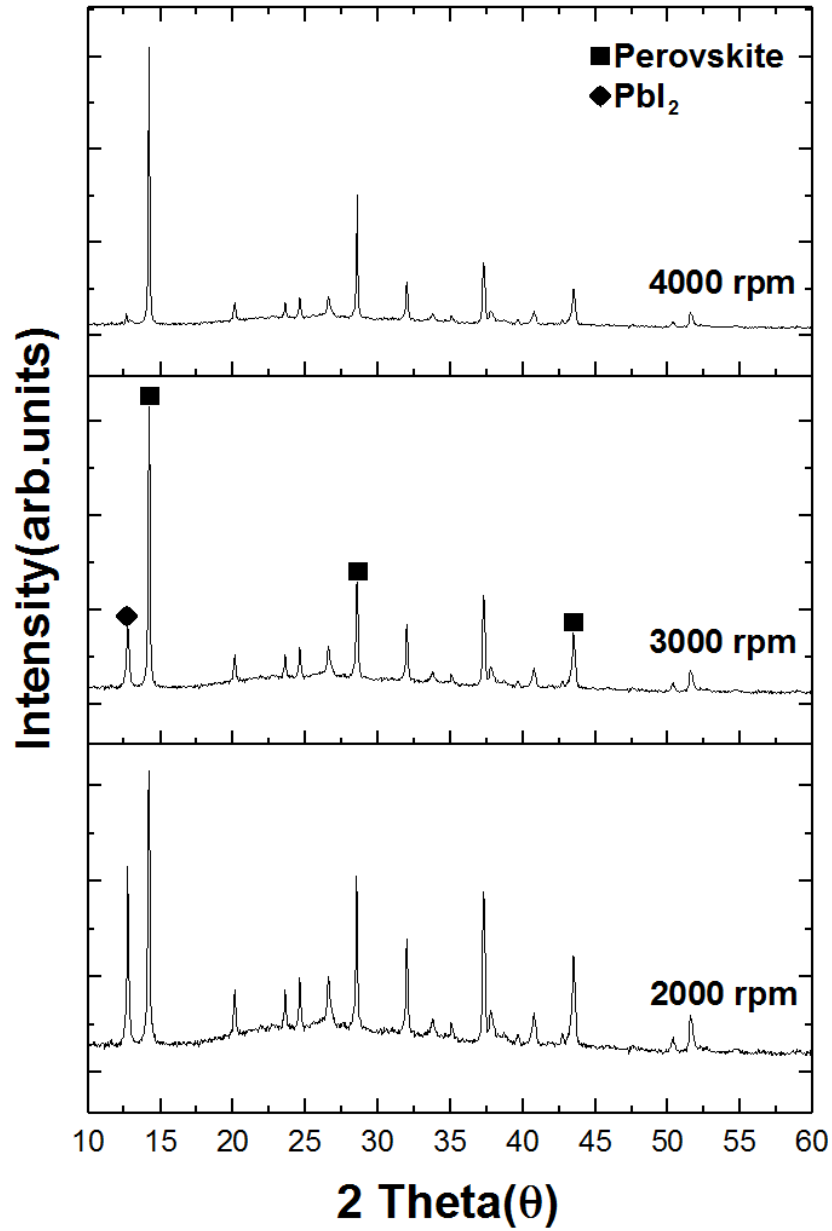


Fig. 5-6 XRD pattern of perovskite film when washing perovskite with difference spin speed.

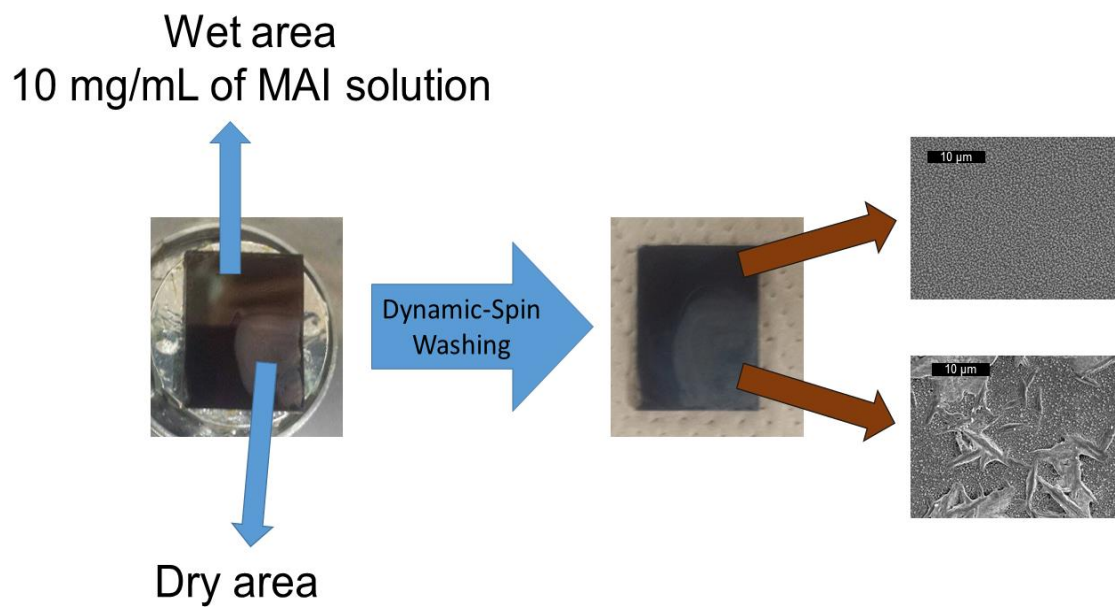


Fig. 5-7 The sample picture before and after using dynamic-spin washing method with SEM surface of dry area and wet area.

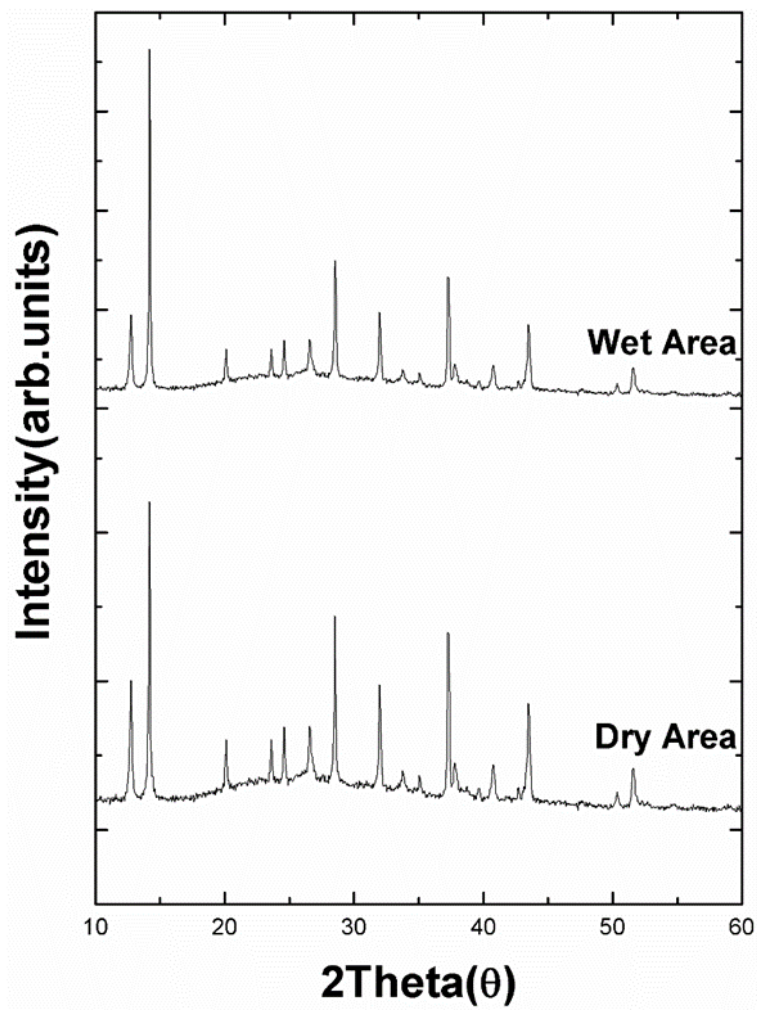


Fig. 5-8 XRD pattern of perovskite films area with the residual solution and the dry area.

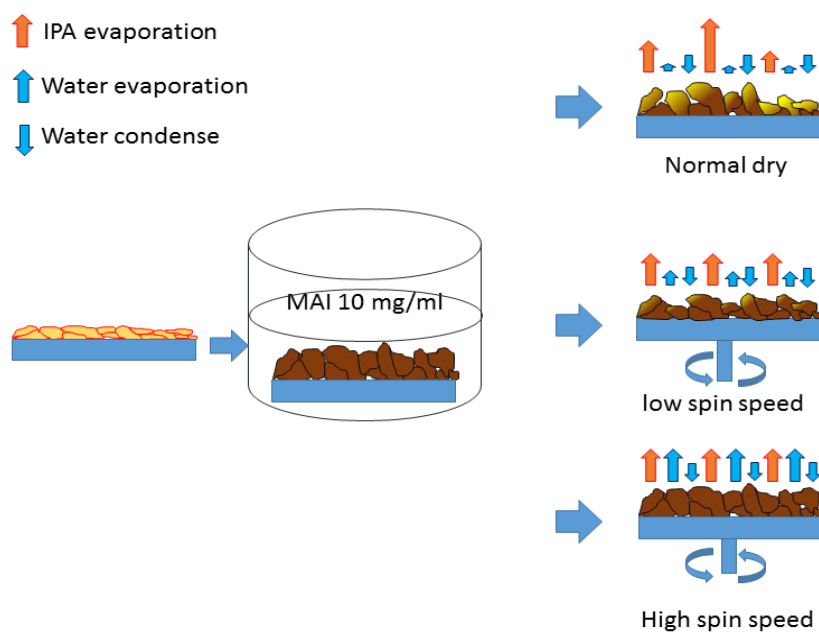


Fig. 5-9 Schematic of explanation of difference surface structure when washing surface of perovskite with difference spin speed.

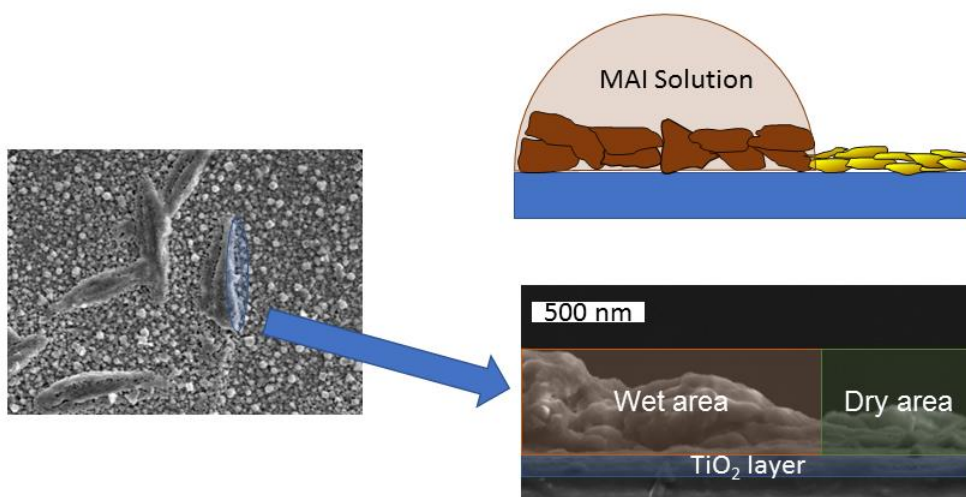


Fig. 5-10 Cross-section and schematic of remain solution area and dry area of boundary of difference perovskite surface morphology.

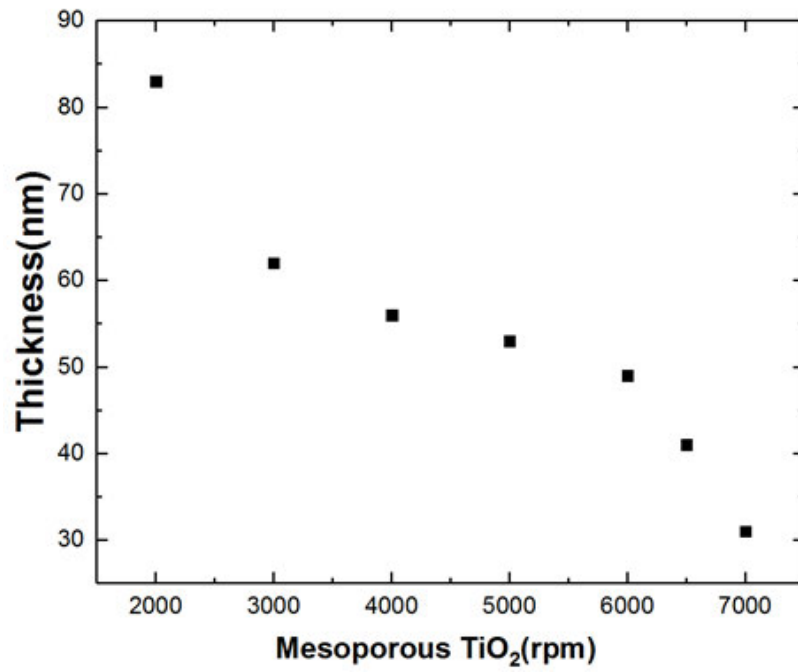


Fig. 5-11 Relationship between film thickness of mesoporous-TiO₂ layer and spin-speed to fabricated mesoporous-TiO₂.

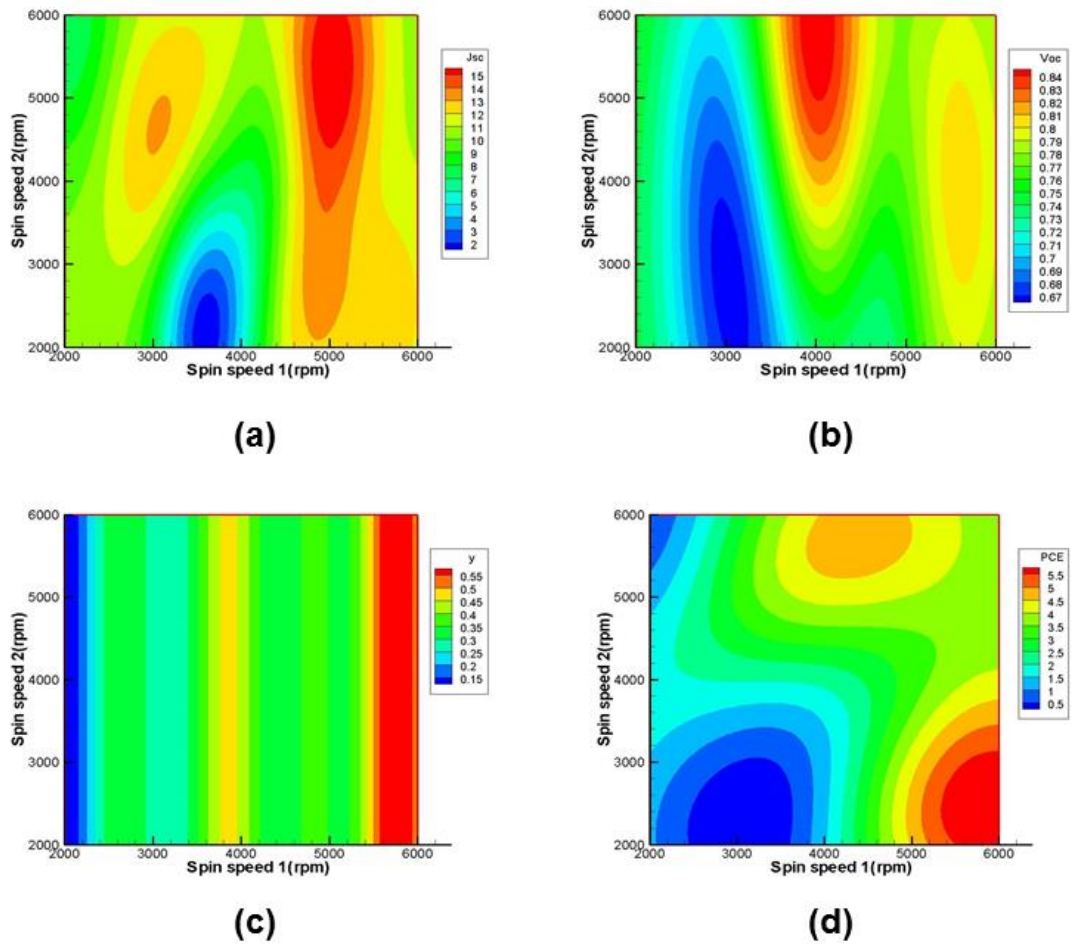


Fig. 5-12 Surface plot of the relationship between experimental parameters (spin speed of dense-TiO₂ and mesoporous-TiO₂) and outputs a) short-circuit current density (J_{sc}), b) open circuit voltage (V_{oc}), fill factor (FF) and d) power conversion efficiency (PCE).

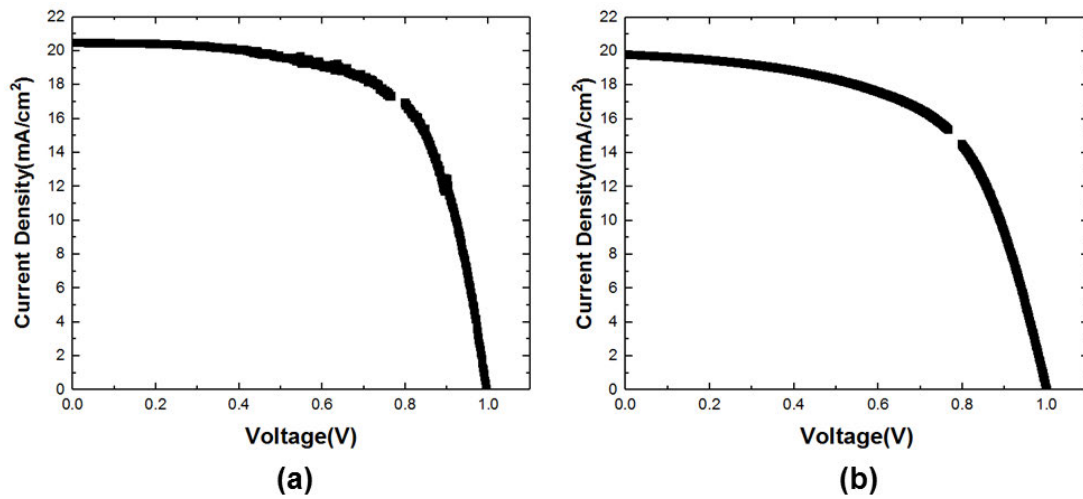


Fig. 5-13 Current-voltage characteristics of the highest performance of (a) small area devices and (b) large area devices when fabricated with the optimal condition. 0.09cm² for the small surface area and 1 cm² for large surface area devices.

Table 5-1 Conversion ratio of PbI_2 to MAPbI_3 when washing them with IPA at difference spin speeds.

Washing spin speed (rpm)	C_{MAPbI_3}
2000	0.63
3000	0.76
4000	0.92

Table 5-2 The conversion ratio of PbI_2 to MAPbI_3 between dry area and wet area.

Condition	C_{MAPbI_3}
Dry area	0.68
Wet area	0.79

Table 5-3 Current density-voltage parameters of small area of PVSCs fabricated with difference washing IPA spin speed.

Washing Spin speed (rpm)	J_{sc} (mA/cm^2)	V_{oc} (V)	FF	PCE (%)
2000	16.5	0.91	0.47	7.2
3000	18.2	0.97	0.58	10.3
4000	22.5	0.95	0.59	12.7

Table 5-4 Current density-voltage parameters of cm^2 area of PVSCs fabricated with difference washing IPA spin speed.

Washing spin speed (rpm)	J_{sc} (mA/cm^2)	V_{oc} (V)	FF	PCE (%)
2000	15.3	0.95	0.32	4.79
3000	17.3	0.98	0.41	6.95
4000	19.7	0.98	0.53	10.3

Table 5-5 Current density-voltage parameters of perovskite solar cell (FTO/Dense- TiO_2 /perovskite/Au) when fabricated with changing fabrication spin speed of compact TiO_2 layer.

Spin speed (rpm)	J_{sc} (mA/cm^2)	V_{oc} (V)	FF	PCE (%)
2000	10.99	0.49	0.28	1.53
3000	9.99	0.7	0.37	2.64
4000	5.27	0.69	0.45	1.79
5000	3.01	0.67	0.49	0.99
6000	2.17	0.65	0.45	0.65
6500	1.34	0.23	0.32	0.1
7000	0	0	0	0

Table 5-6 Input parameters for fabricating dense-TiO₂ and mesoporous TiO₂ layer assigned by Latin-hyper cube method.

Condition	Dense-TiO ₂ (rpm)	Mesoporous-TiO ₂ (rpm)
1	4676	2962
2	2430	4696
3	5028	5358
4	3126	4116
5	2038	5912
6	5608	2754
7	5424	3482
8	3556	2272
9	4296	3830
10	3836	4996

Table 5-7 Current density-voltage parameters of perovskite solar cell (half-cell) when fabricated by using the conditions in **Table 5-6**.

Condition	J_{sc} (mA/cm ²)	V_{oc} (V)	FF	PCE (%)
1	12.83	0.75	0.35	3.31
2	10.21	0.71	0.29	2.12
3	16.07	0.78	0.34	4.31
4	12.41	0.68	0.27	2.25
5	7.005	0.75	0.12	0.61
6	12.62	0.80	0.57	5.76
7	12.51	0.81	0.45	4.48
8	1.44	0.73	0.37	0.37
9	8.355	0.79	0.33	2.21
10	10.67	0.83	0.46	4.12

Table 5-8 Current density-voltage parameters of perovskite solar cell(half-cell) when fabricated with optimal condition

Sample number	J _{sc} (mA/cm ²)	V _{oc} (V)	FF	PCE (%)
1	12.11	0.81	0.592	5.81
2	12.05	0.80	0.589	5.68
3	12.45	0.80	0.592	5.90
4	11.63	0.82	0.591	5.64
5	11.89	0.82	0.594	5.79
6	12.51	0.82	0.592	6.07
Average	12.11	0.81	0.591	5.81

Table 5-9 Current density-voltage parameters of perovskite solar cell when fabricated with 0.09cm² and 1 cm² scale area.

Condition	J _{sc} (mA/cm ²)	V _{oc} (V)	FF	PCE (%)
Best cell(0.09cm ²)	21.51	0.99	0.65	13.75
Average(0.09 cm ²)	21.21	0.99	0.64	13.47
Best cell(1 cm ²)	19.83	0.99	0.60	11.76
Average(1 cm ²)	19.53	0.99	0.58	11.56

Table 5-10 Current density-voltage parameters of perovskite solar cell when fabricated with optimal condition

Area	Sample number	J _{sc} (mA/cm ²)	V _{oc} (V)	FF	PCE (%)
0.09 cm ²	1	21.51	0.99	0.646	13.75
	2	21.36	0.99	0.646	13.66
	3	21.12	0.99	0.643	13.44
	4	21.04	0.99	0.643	13.39
	5	20.89	0.99	0.639	13.21
	6	21.36	0.99	0.633	13.38
	Average	21.21	0.99	0.641	13.47
1 cm ²	1	19.83	0.99	0.599	11.76
	2	19.26	0.99	0.597	11.38
	3	19.39	0.99	0.589	11.30
	4	19.66	0.99	0.589	11.46
	Average	19.535	0.99	0.5935	11.47

Reference

- [5-1] Chen, W., Wu, Y., Yue, Y., Liu, J., Zhang, W., Yang, X., Chen, H., Bi, E. & Han, L. (2015). *Science*, 350(6263), 944-948.
- [5-2] Kojima, A., Teshima, K., Shirai, Y., & Miyasaka, T., *Journal of the American Chemical Society* (2009), 131(17), 6050-6051.
- [5-3] Nie, W., Tsai, H., Asadpour, R., Blancon, J. C., Neukirch, A. J., Gupta, G., Crochet, J.J., Chhowalla, M., Tretiak, S., Alam, M.A., Wang, H.L. & Wang, H. L. (2015). *Science*, 347(6221), 522-525.
- [5-4] Kim, H. S., Lee, J. W., Yantara, N., Boix, P. P., Kulkarni, S. A., Mhaisalkar, S., Grätzel, M. & Park, N. G. (2013). *Nano letters*, 13(6), 2412-2417.
- [5-5] Ponseca Jr, C. S., Savenije, T. J., Abdellah, M., Zheng, K., Yartsev, A., Pascher, T., Harlang, T., Chabera, T., Pullerits, T., Stepanov, A. & Wolf, J. P. (2014). *Journal of the American Chemical Society*, 136(14), 5189-5192.
- [5-6] Saliba, M., Matsui, T., Seo, J. Y., Domanski, K., Correa-Baena, J. P., Nazeeruddin, M. K., Zakeeruddin, S.M., Tress, W., Abate, A., Hagfeldt, A. & Grätzel, M. (2016). *Energy & Environmental Science*, 9(6), 1989-1997.
- [5-7] Sudchanham, J., Batmunkh, M., Reutrakul, V., Shapter, J. G., Raston, C. L., & Pakawatpanurut, P. (2017). *ChemistrySelect*, 2(1), 369-374.
- [5-8] Eperon, G. E., Burlakov, V. M., Docampo, P., Goriely, A., & Snaith, H. J. (2014). *Advanced Functional Materials*, 24(1), 151-157.

- [5-9] Quarti, C., Mosconi, E., Ball, J. M., D'Innocenzo, V., Tao, C., Pathak, S., Snaith, H.J., Petrozz, A. & De Angelis, F. (2016). *Energy & Environmental Science*, 9(1), 155-163.
- [5-10] Kutes, Y., Ye, L., Zhou, Y., Pang, S., Huey, B. D., & Padture, N. P. (2014). *The journal of physical chemistry letters*, 5(19), 3335-3339.
- [5-11] Razza, S., Di Giacomo, F., Matteocci, F., Cina, L., Palma, A. L., Casaluci, S., Cameron, P., D'Epifanio, A., Licoccia, S. & Brown, T. M. (2015). *Journal of Power Sources*, 277, 286-291.
- [5-12] Wu, C. G., Chiang, C. H., Tseng, Z. L., Nazeeruddin, M. K., Hagfeldt, A., & Grätzel, M. (2015). *Energy & Environmental Science*, 8(9), 2725-2733.
- [5-13] Li, X., Bi, D., Yi, C., Décoppet, J. D., Luo, J., Zakeeruddin, S. M., Hagfeldt, A. & Grätzel, M. (2016). *Science*, 353(6294), 58-62.
- [5-14] Gouda, L., Gottesman, R., Tirosh, S., Haltzi, E., Hu, J., Ginsburg, A., Keller, D.A., Bouhadana, Y. & Zaban, A. (2016). *Nanoscale*, 8(12), 6386-6392.
- [5-15] Di Carlo, A., Matteocci, F., Razza, S., Mincuzzi, M., Di Giacomo, F., Casaluci, S., Gentilini, D., Brown, T.M., Reale, A., Brunetti, F., Licoccia, S. & D'Epifanio, A. (2014, August), 2014 IEEE 14th International Conference on (pp. 70-74). IEEE.
- [5-16] Tai, Q., You, P., Sang, H., Liu, Z., Hu, C., Chan, H. L., & Yan, F. (2016), *Nature communications*, 7, 11105
- [5-17] Sveinbjörnsson, K., Aitola, K., Zhang, J., Johansson, M. B., Zhang, X., Correa-Baena, J. P., Hagfeldt, A., Boschlo, G. & Johansson, E. M. (2016). *Journal of Materials Chemistry A*, 4(42), 16536-16545.

- [5-18] Lee, M. M., Teuscher, J., Miyasaka, T., Murakami, T. N., & Snaith, H. J., (2012). *Science*, 338(6107), 643-647.
- [5-19] Chen, Q., Zhou, H., Song, T. B., Luo, S., Hong, Z., Duan, H. S., Dou, L., Liu, L. & Yang, Y. (2014). *Nano letters*, 14(7), 4158-4163.
- [5-20] Im, J. H., Kim, H. S., & Park, N. G. (2014). *Apl Materials*, 2(8), 081510.
- [5-21] Xiao, M., Huang, F., Huang, W., Dkhissi, Y., Zhu, Y., Etheridge, J., Gray-Weale, A., Bach, U., Cheng, Y.B. & Spiccia, L. (2014). *Angew. Chem.*, 126, 10056.
- [5-22] Jeon, N.J., Noh, J.H., Kim, Y.C., Yang, W.S., Ryu, S. & Seok, S.I. (2014). *Nat. Mater.*, 13, 897.
- [5-23] Zhang, H., Mao, J., He, H., Zhang, D., Zhu, H. L., Xie, F., Wong, K., Grätzel, M. & Choy, W. C. (2015). *Advanced Energy Materials*, 5(23).
- [5-24] Gao, C., Liu, J., Liao, C., Ye, Q., Zhang, Y., He, X., Gao, X., Mei, J. & Lau, W. (2015). *RSC Advances*, 5(33), 26175-26180.
- [5-25] Li, F., Bao, C., Zhu, W., Lv, B., Tu, W., Yu, T., Yang, J., Zhou, X., Wang, Y., Wang, X., Zhou, Y. & Zou, Z. (2016) *Journal of Materials Chemistry A*, 4(29), 11372-11380.
- [5-26] Pang, S., Hu, H., Zhang, J., Lv, S., Yu, Y., Wei, F., Qin, T., Xu, H., Liu, Z. & Cui, G. (2014). *Chemistry of Materials*, 26(3), 1485-1491.
- [5-27] Burschka, J., Pellet, N., Moon, S.-J., Humphry-Baker, R., Gao, P., Nazeeruddin, M.K. & Grätzel, M. (2013). *Nature*, 499, 316.

- [5-28] Docampo, P., Hanusch, F.C., Stranks, S.D., Döblinger, M., Feckl, J.M., Ehrensperger, M., Minar, N.K., Johnston, M.B., Snaith, H.J. & Bein, T. (2014). *Adv. Energy Mater.*, 4, 1400355.
- [5-29] Xiao, Z., Bi, C., Shao, Y., Dong, Q., Wang, Q., Yuan, Y., Wang, C., Gao, Y. & Huang, J. (2014). *Energy Environ. Sci.*, 7, 2619.
- [5-30] Li, F., Bao, C., Zhu, W., Lv, B., Tu, W., Yu, T., Yang, J., Zhou, X., Wang, Y., Wang, X., Zhou, Y. & Zhou, Z. (2016). *Journal of Materials Chemistry A*, 4(29), 11372-11380.
- [5-31] Liu, J., Gao, C., He, X., Ye, Q., Ouyang, L., Zhuang, D., Liao, C., Mei, J. & Lau, W. (2015). *ACS applied materials & interfaces*, 7(43), 24008-24015.
- [5-32] Yang, S., Zheng, Y.C., Hou, Y., Chen, X., Chen, Y., Wang, Y., Zhao, H. & Yang H.C. (2014). *Chemistry of Materials*, 26, 6705.
- [5-33] Giordano, F., Abate, A., Baena, J. P. C., Saliba, M., Matsui, T., Im, S. H., Zakeeruddin, S.M., Nazeeruddin, M.K., Hagfeldt, A. & Graetzel, M. (2016). *Nature communications*, 2016, 7, 10379.
- [5-34] Gao, L. L., Li, C. X., Li, C. J., & Yang, G. J. (2017). *Journal of Materials Chemistry*, 5, 1548-1557
- [5-35] Hsieh, T.Y., Wei, T.C., Wu, K.L., Ikegami, M. & Miyasaka, T. (2015). *Chem. Commun.*, 2015, 51(68), 13294-13297.
- [5-36] Ahn, N., Son, D. Y., Jang, I. H., Kang, S. M., Choi, M., & Park, N. G. (2015). *Journal of the American Chemical Society*, 137(27), 8696-8699.

- [5-37] Koo, J., Kim, T., Jung, C., & Lee, J. (2007) International journal of heat and mass transfer, 50(21), 4275-4285.
- [5-38] Chen, Q., Zhou, H., Hong, Z., Luo, S., Duan, H. S., Wang, H. H., Liu, Y., Li, G. & Yang, Y. (2013) Journal of the American Chemical Society, 136(2), 622-625.
- [5-39] J. Schlipf, P. Docampo, C. J. Schaffer, V. Körstgens, L. Bießmann, F. Hanusch, N. Giesbrecht, S. Bernstorff, T. Bein, and P. Müller-Buschbaum, J. (2015) Phys. Chem. Lett., 6, 1265–12
- [5-40] Chang, C. Y., Huang, W. K., Chang, Y. C., Lee, K. T., & Chen, C. T. (2016). Journal of Materials Chemistry A, 4(2), 640-648.
- [5-41] Lang, F., Gluba, M. A., Albrecht, S., Rappich, J., Korte, L., Rech, B., & Nickel, N. H. (2015). The journal of physical chemistry letters, 6(14), 2745-2750.
- [5-42] Ariyarit, A., Takenaka, I., Yoshikawa, R., Gillot, F., & Shiratori, S. (2016). RSC Advances, 6(100), 98052-98058.
- [5-43] Kim, H. S., & Park, N. G. (2014). The journal of physical chemistry letters, 5(17), 2927-2934.
- [5-44] Stein, M. (1887) Technometrics, 29(2), 143-151.
- [5-45] Gao, Y., & Wang, X. (2008). The International Journal of Advanced Manufacturing Technology, 37(9), 953-960.
- [5-46] Simpson, T., Mistree, F., Korte, J., & Mauery, T. (1998, September) In 7th AIAA/USAF/NASA/ISSMO Symposium on Multidisciplinary Analysis and Optimization (p. 4755).

Chapter 6

Summary

6.1 General summary

This thesis demonstrates the design of an experiment for semitransparent organic thin film solar cell and lead tri-halide perovskite solar cell.

In studies of OSCs devices, the TiO₂ electron transport layers, based on PDDA and TALH from a water-based solution, are fabricated via the spray-LBL method for solar cell applications. The titanium dioxide structure deposited on glass by the spray-LBL method was composed of both anatase (004) and rutile (210) phases. The largest crystalline sizes of the anatase (004) and rutile (210) phases were achieved after annealing at 450°C and without annealing, respectively. The optical energy band gap was reduced from 3.30 eV to 3.20 eV. After preparation of the TiO₂ layer via the spray-LBL using a water-based solution with the best conditions for the surface morphology, precise thickness control and the optical properties, semitransparent bulk heterojunction solar cells were successfully fabricated. The efficiency of these organic thin film solar cells depended on the thickness of the titanium dioxide layer, and the semitransparent polymer-based solar cells had power conversion efficiencies of more than 2% after improving the TiO₂ layer thickness, which was controlled via the spray-LBL method.

In the studies of PVSCs, first is the developed tool for optimising the structure for the fabricated PVSCs. The structure ITO/SnO₂/Perovskite/Spiro-OMeTad/Au has been chosen for our purposes – this structure is a good candidate for flexible devices with low-cost material. To find the maximum efficiency, we optimised the experimental conditions using the Kriging model method from experimental data given through Latin hypercube sampling. We could approximate the best condition for fabricating PVSCs with only 12

conditions of experiment. Under the best condition, we observed the high efficiency of PVSCs at 8.75%. From the LSH sampling, we could observe the spin-coating speed and MAI dipping time have strong relationships with efficiency due to the conversion ratio of PbI_2 to MAPbI_3 and the surface morphology of the perovskite film.

The second studies for PVSCs are focus on fabrication process for an up-scaled size of PVSCs based on TiO_2 layer. We found high washing-spin speed has the large effect to increase PCE by preventing the vapor reaction. The vapor reaction strongly affects re-conversion perovskite to PbI_2 and making a rough surface of perovskite film. This experiment proposed that not only crystalline grown phase of perovskite film but also the washing step of perovskite film is important to scale up the area of PVSCs. Lastly, we succeeded in achieving 13.5% for the 0.09 cm^2 area and 11.8% for the 1 cm^2 area by using the optimised process.

6.2 Future Approach

Until now, many researchers for photovoltaic devices already succeeded in fabricating it with high PCE. However, these devices are in need of further attention as problems remain. These include the degradation effect from humidity, damage from hot temperature, using many toxic material and the recycling of out of date products. To improve them, not only the structure of photovoltaic should be developed, but also the outside product packaging also should be developed too, comprising encapsult layer, antirefraction and cooling system. For the future development of OSC, this device must focus on reducing the production cost of ETLs and HTLs material such as PCBM, P3HT and PTB7. Moreover, this device have to investigated some mechanism to improve the stability of it at high temperature with high humidity. PVSCs devices already improve for high PCE, but lack of knowledge about crystalline stability in high temperatures is crucial

for solar farms. Moreover, the amount of lead in these devices must be decreased in the near future.

Acknowledgement

I am deeply grateful to Prof. Seimei Shiratori and Asst. Prof. Frédéric Gillot from École Centrale de Lyon, that they patiently taught me, and whose comments and suggestions were innumerably valuable throughout my doctor study.

I would like to thank Asso. Prof Ishigue Takaaki, Prof. Fujihara Shinobu and Asso. Prof. Noda Kei for their constructive comments and careful reviewing on this thesis. I also thank my colleagues, Mr. Takenaka Issei, Mr. Yoshikawa Ryohei, Fukada Kenta and all members of Shiratori laboratory for their Kind cooperation and warm friendship.

This work was partially funded by Keio Leading-edge Laboratory of Science and Technology(KLL) sponsored by Japanese Ministry of Education, Science Culture and Sports. Partial support from Marubun Research Promotion Foundation of Japan is appreciated.

Finally, I would like to dedicate this thesis to my family for their love and support.

ARIYARIT, Atthaporn